ABSTRACT

DATTELBAUM, ANDREW MARTIN. Design, Characterization, and Reactivity of Copper(I)-Zirconium(IV) Halide Analogs of Metal Chalcogenides. (Under the direction of James D. Martin.)

In this work, new metal-halide materials are designed by using a novel charge matching methodology whereby structural analogs of metal chalcogenides are prepared using a halide-for-chalcogenide substitution strategy. In particular, the metal-halide materials prepared herein are analogous to known phosphate, phosphonate, and silicate-based clay-type materials. Following this charge matching strategy, dimethyl ammonium cations were shown to organize copper(I) and zirconium(IV) primary building blocks into $(CuZrCl_6)^-$ chains, which are analogous to the thiophosphate chains in $(MPS_4)^-$. Hydrogen bond formation to the dimethylammonium cations results in significant distortions to the metal chloride building blocks, which can be understood as second order Jahn-Teller-type distortions. In the absence of an extra-framework cation, the primary tetrahedral and octahedral building blocks were assembled into a condensed three-dimensional network Cu_2ZrCl_6, which is constructed from adamantane-type building blocks. Cu_2ZrCl_6 is shown to undergo reversible thermochromic phase changes because of a structural distortion of the cuprous chloride tetrahedra due to second-order mixing. This material also exhibits an approximately temperature independent (TIP), or Van Vleck, paramagnetism that increases at the low temperature phase transition. The change at the phase transition appears to be related to the band gap differences in the low- and high-temperature phases of Cu_2ZrCl_6. The reactivity of Cu^+ in the presence of the Lewis acidic Zr^{4+} is then demonstrated by the solvothermal reaction of Cu_2ZrCl_6 in benzene, which breaks up the three-dimensional framework into a one-dimensional

$[((bz)CuCl_3)_2Zr]_\infty$ chain that is described as a metal-halide phosphonate analog. Chains of $((bz)CuCl_3)_2Zr$ are linked along the crystallographic **c** direction *via* an edge-to-face π-stacking of the coordinated benzene molecules. The crystal packing forces are shown to influence dramatic second-order Jahn-Teller distortions making each of the two $((bz)CuCl_3)^{2-}$ units distinct. The distortions of the distinct $((bz)CuCl_3)^{2-}$ units emphasize the unique donor and acceptor properties of the Cu(I) ion. Addition of $ZrCl_4$ to the solvothermal reaction of Cu_2ZrCl_6 in benzene yields the molecular species $(bz)_2Cu_2Zr_2Cl_{10}$•bz, which loses solvent in a stepwise fashion. These desolvated materials exhibit reversible binding of ethylene reminiscent of the reversible sorption behavior typically observed for silicate-based clays.

DESIGN, CHARACTERIZATION, AND REACTIVITY OF COPPER(I)-ZIRCONIUM(IV) HALIDE ANALOGS OF METAL CHALCOGENIDES

by

ANDREW MARTIN DATTELBAUM

A dissertation submitted to the Graduate Faculty of
North Carolina State University
in partial fulfillment of the
requirements for the Degree of
Doctor of Philosophy

DEPARTMENT OF CHEMISTRY

Raleigh

2000

Approved by:

_____ _____

Chair of Advisory Committee

_____ _____

ACKNOWLEDGEMENTS

The work described in this dissertation would not have been possible without the help of many individuals. First, I would like to thank my dissertation advisor, James D. Martin, for the tremendous effort he has expended to bring this work to completion, as well as for the years he has invested into my development both professionally and personally. I would also like to thank my committee members, Dr. Jonathan Lindsey, Dr. Klaus Bachmann, and, especially, Dr. Mike Whangbo, for valuable discussions about my research during my stay at North Carolina State University. Many past and present members of the Martin group have also provided me with their scientific and emotional support, including Kevin Greenwood, Larken Euliss, Steve Smith, and Cristin Keary. In particular, I am indebted to Roger M. Sullivan, whom I began graduate school with five years ago. We joined the Martin group together, and have since worked well together as colleagues up to the writing of this work.

I would like to thank my wife, Dana, for her wonderful scientific insight and for always providing a light moment to brighten my days. My brother, Jonathan, also afforded me hours of stimulating scientific discussion across various disciplines, and provided me with a different perspective on graduate school. And, perhaps most important, I would like to thank my parents, Alan and Suzanne Dattelbaum, for providing a loving home, which allowed me to gain the self-confidence and humility I have needed to succeed in whatever I have set out to accomplish in my life.

PERSONAL BIOGRAPHY

I was born Andrew Martin Dattelbaum on November 20, 1973 in Fairfax, VA, along with my identical twin brother, Jonathan. Our first few days were rather precarious, because Jonathan and I had been born with abnormal ratios of red and white blood cells; he had 90% red and 10 % white, while I had 10% red and 90% white blood cells. The clever doctors at Fairfax County Hospital found a way to remove the blood from our newborn bodies, mix it together, then return it back to us. Of course, the procedure was successful, and I am told that it was written in a medical journal (my first publication!), although I do not have the reference. Most of my early childhood was then spent moving along the East Coast as my father moved up the corporate ladder. We lived as far north as Wilmington, Delaware, where my sister, Alison, was born, too as far south as Florence, South Carolina. In 1985, my family returned north and moved to Salisbury, MD, where I attended high school at James M. Bennett Senior High. At JMB I developed an interest in chemistry thanks largely to my high school chemistry teacher, Ronald Peterman. However, upon graduation in 1991, I went off to James Madison University in Harrisonburg, VA, where I started off as a pre-med. But, thanks to an outstanding group of professors in the Department of Chemistry, I became convinced that chemistry was the subject matter I really enjoyed. And, in 1995 I graduated *magna cum laude* with distinction in chemistry. During my time in the Department of Chemistry at JMU I met another outstanding chemistry major, Dana McGraw, who I eventually married in 1997. Since 1995 I have lived in Raleigh, NC where I have been attending graduate school in the Department of Chemistry at North Carolina State University.

TABLE OF CONTENTS

LIST OF FIGURES

LIST OF TABLES

Chapter 1:

Introduction

1.1. Introduction

With the increasing demand for new materials tailored for specific processes, there is a need for the ability to rationally design materials. Molecular chemists have a large body of systematized, experimental knowledge, as well as theoretical models, to draw from in order to rationally design specific molecules. Far less information is available to solid-state chemists in order to design materials with specific extended structures, thus presenting an enticing challenge to solid-state chemists. This is indeed a difficult task considering the large number of atoms typically involved in multi-dimensional solid-state materials that can be assembled in nearly an infinite number of combinations. Several researchers have chosen to address this problem using computerized algorithms that calculate the lowest potential energy structure for products assembled under a given set of coordination constraints for the atoms involved.[1-3] A more common approach, involves the exhaustive synthesis and characterization of numerous structures within a given system by varying conditions in order to fully explore and understand the structure-property relationships. Such a combinatorial approach has become a popular method in the pharmaceutical industry with the advent of automation, and has greatly facilitated the exploration of multivariable syntheses.[4] Solid-state chemists at Symyx Technologies and Bell Labs are currently leading the development of this new technology with respect to materials synthesis.[5]

An alternative approach to the exploratory methods described above involves the design of new materials *by analogy* utilizing the principles of structure and bonding obtained from the plethora of previously characterized materials and applying them to the design of new materials. An example of such synthesis by analogy is found in the effort

to incorporate transition metals into the frameworks of the now well established family of zeolite materials. Zeolites are aluminosilicate materials with the general formula $[A]_n(Al_nSi_{m-n}O_{2m})$ (where A = extra-framework cation), which have found tremendous utility in industrial processes in the areas of catalysis and gas sorption.[6] Substitution of the framework or the extra-framework cations in order to design new materials for a specific process is commonly done.[7] Incorporation of Lewis acidic and/or redox active transition metals into oxide frameworks has been actively pursued to design more reactive framework materials because of their potential value in novel catalytic or magnetic materials.[8] For example, partial substitution of cobalt ions into open-framework materials has led to novel catalysts for the autoxidation of cyclohexane[9] and *p*-cresol.[10] Such materials combine the size and shape selectivity of the framework with the reactivity of a transition element in a catalytically active metal oxide. In contrast to the extensive number of compounds designed by cationic substitution, relatively little work has involved the preparation of framework materials with anions other than oxygen. Significant progress has, however, been made in the preparation of sulfide,[11,12]cyanide,[13]and pnictide[14,15,16] framework materials.

The Martin group has chosen to investigate the syntheses of metal halide materials in order to exploit the reactivity of the metal-halide building blocks for potential catalytic applications. As is evident by reviewing any introductory organic chemistry textbook a variety of metal halide compounds are frequently utilized as catalysts for homogeneous or solution reactions. The activity of the metal halides are generally due to Lewis acidity, redox capability, and/or coordination flexibility of the metal atom. However, relatively little attention has been paid to the solid-state structural

design of such materials for potential heterogeneous catalytic applications. As described above, the most commonly used heterogeneous catalysts are metal-oxide framework materials, such as zeolites and metal phosphates, in which the oxide framework provides reactant, transition state, or product selectivity.[17] It is anticipated that framework materials constructed from metal halides would combine the catalytic ability of metal halide building blocks with the size and shape selectivity traditionally found for zeolites and clays. *Thus, it is our goal to organize reactive metal halide building blocks into framework constructions similar to metal oxide materials in order to obtain novel materials that are: 1) structurally well-defined and 2) possess novel catalytic properties.*

1.2. Halide for Chalcogenide Substitution Methodology

A search of the Inorganic Cambridge Structural Database (ICSD), summarized in Figure 1, dramatically demonstrates oxide-based materials to dominate the field of solid-state chemistry. Oxides exhibit widely diverse properties and are useful materials as high-temperature superconductors, catalysts, and optical materials.[18,19] Non-oxide, solid-state systems, although significantly underexplored, provide a similar range of properties. **My research has utilized the large number and variety of known oxide materials to develop an approach towards the design of new framework constructions that involves a halide for chalcogenide substitution strategy.** In this way, novel metal halide materials are designed as charge matched structural analogs of metal chalcogenides.[20] For example, part of the work described in this dissertation has developed the structural analogy between the tetrahedral building block $(CuCl_4)^{3-}$ and the

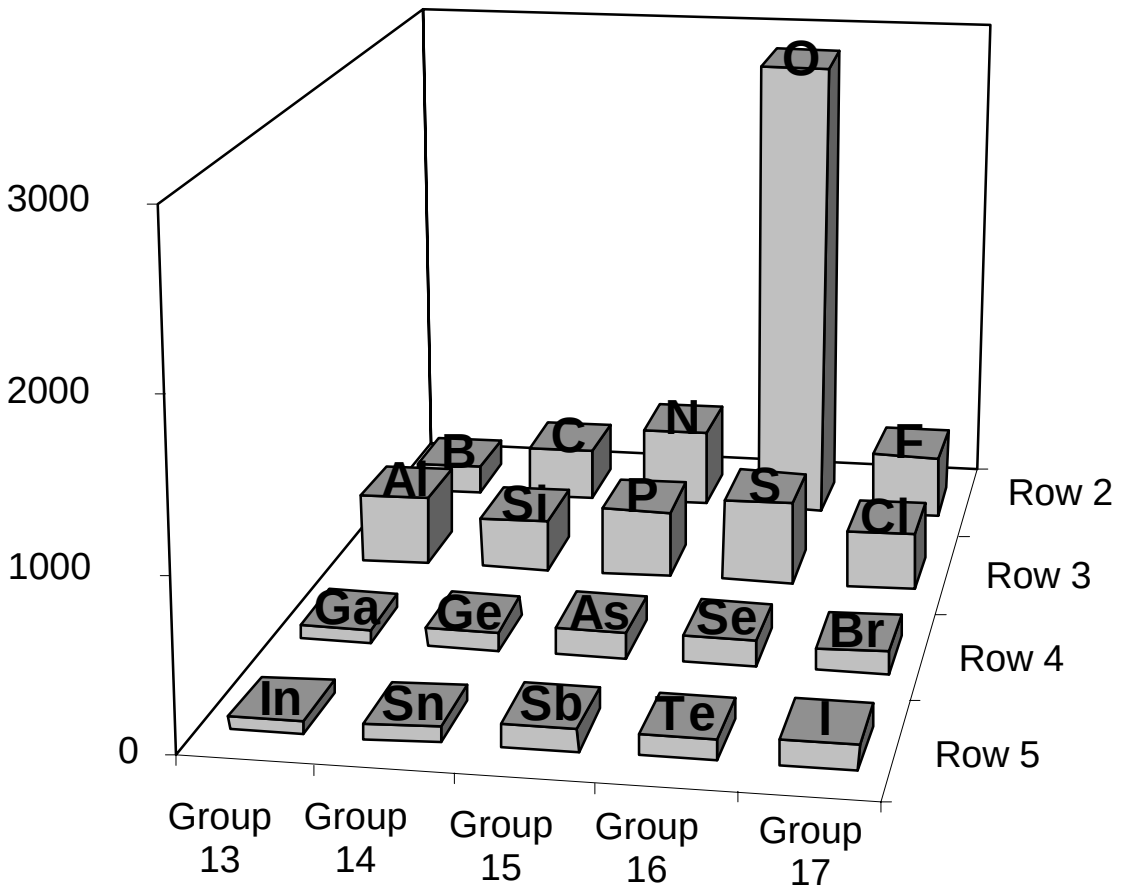

Figure 1.1. Summary of a search of the Inorganic Crystallographic Structural Database (ICSD).

isostructural and isoelectronic $(PO_4)^{3-}$ or $(PS_4)^{3-}$. The "building blocks" of a material refer to the framework cation and the surrounding coordination sphere of anionic ligands. This analogy will also be applied towards the design of metal halide analogs of phosphonate materials, where $[\mathbf{L}CuCl_3]^{2-}$or $[\mathbf{R}ZnCl_3]^{2-}$ (where **R**=alkyl or aryl group, **L** = neutral two electron donor) are charged matched and isostructural to $[\mathbf{R}PO_3]^{2-}$. This charge matching strategy is readily understood by the utilization of lower charged metal cations (a move to the left in the periodic table) to compensate for the lost charge on going from the oxide (-2) to the halide (-1) (a move to the right in the periodic table). It is not surprising that such analogies between chlorides and chalcogenides can exist as the radius and electronegativity of chloride (0.99 Å, 3.0) is intermediate that of oxygen and sulfur, O (0.74 Å, 3.5) and S (1.04 Å, 2.5).[21] Previous work in our group has demonstrated the design of novel materials by replacing the oxygen anions with halides in the preparation of several halozeotype materials, $[Cu_nZn_{m-n}Cl_{2m}]^{n-}$, shown in Figure 2a-c, which are direct analogs of aluminosilicate zeolites, $[Al_nSi_{m-n}O_{2m}]^{n-}$.[22]

1.3. The Utility of Copper(I) Halide Materials

The redox activity and coordination flexibility of Cu^I led us to initiate studies in which $(CuCl_4)^{3-}$ tetrahedra are constructed along with other Lewis acidic metals into open-framework, metal-halide materials. The chemistry of copper (I) has been the subject of numerous reports because of its reactivity and function in a number of catalytic[23,24] and biological systems.[25] Copper-catalyzed reactions include the addition of carbanions to α,β-unsaturated carbonyls,[26,27] cyclopropanation of alkenes by α-carbonyl

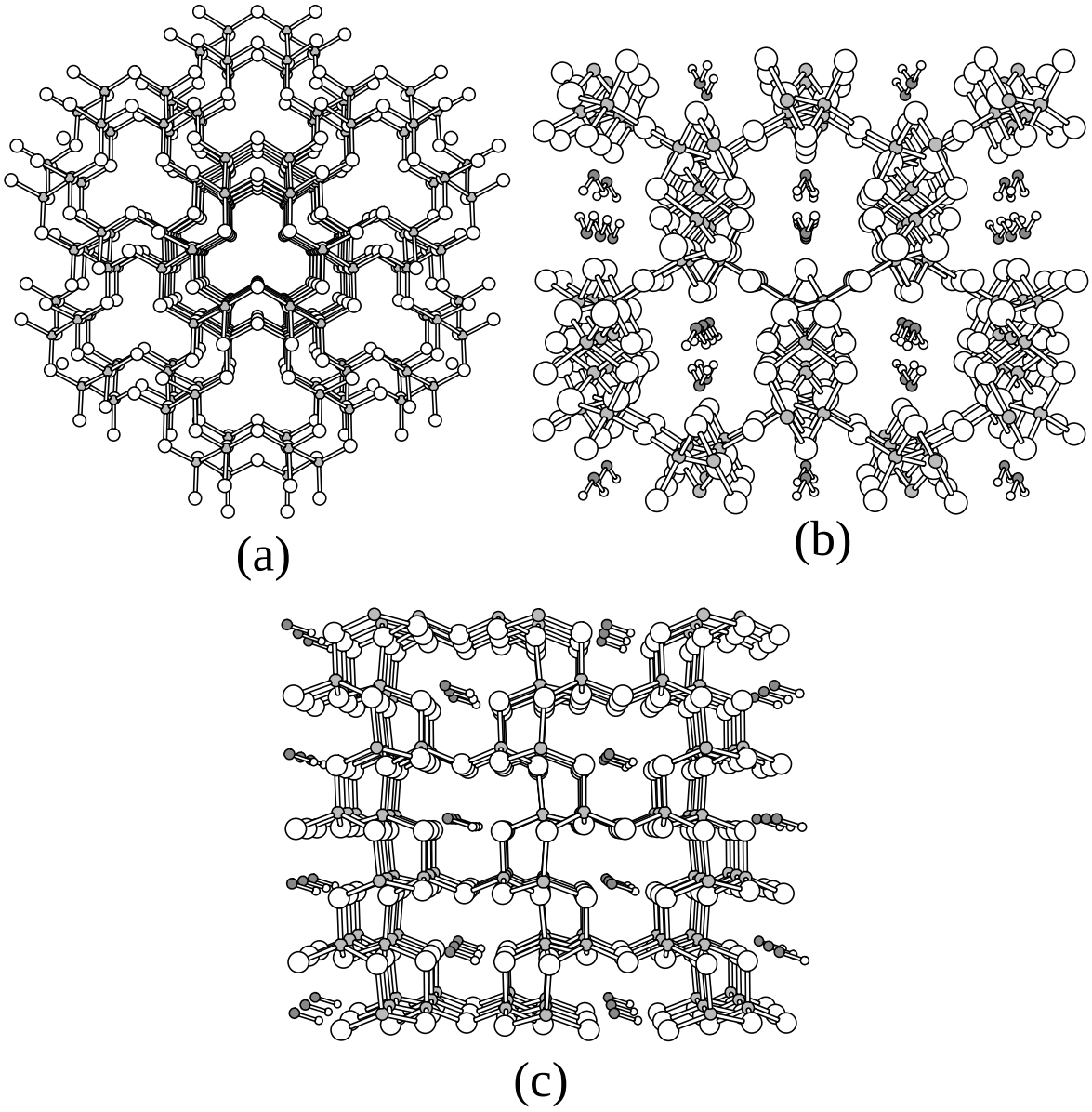

Figure 1.2. Ball and stick drawings of (a) $[NMe_3H]CuZn_5Cl_{12}$, (b) $A_2Cu_2Zn_4Cl_{12}$ (where A = NMe_2H_2 or NEt_2H_2), and (c) $ACu_2Zn_2Cl_7$ (where A = Rb or $NMeH_3$), which are metal halide analogs of aluminosilicate zeolites. Larger, unshaded spheres are chlorides, and the larger, shaded spheres represent either Zn^{2+} or Cu^{+}. The smaller, unshaded spheres are carbon atoms, and the smaller, shaded spheres are nitrogen atoms. The trimethyl ammonium cations have been omitted from (a) for clarity.

biazoalkanes,[28,29] and atom transfer radical polymerizations.[30,31] In biological systems, ethylene, the smallest plant hormone, binds to the copper receptor site ETR- 1,[32,33] which participates in a variety of stress responses and developmental processes.[34] The combination of Lewis acidic metals with $(CuCl_4)^{3-}$ tetrahedra has a dramatic influence on the reactivity of the copper chloride building blocks by making it more Lewis acidic. For example, the catalytic activity of copper (I) chloride in the presence of strong Lewis acids has received attention for the polymerization of benzene, and the insertion of carbon monoxide into aromatic C-H bonds.[35] Recent theoretical calculations on the Mukaiyama aldol reaction,[36] a conjugative addition reaction involving an organocuprate reagent, have shown that a copper-BF_3 complex has to form before the final C-C bond formation step can occur *via* reductive elimination.[37] Studies in our laboratory have shown that copper (I) tetrachloride tetrahedra in the presence of Lewis acids can reversibly bind and/or form stable complexes with olefinic[38,39] molecules like ethylene; whereas, CuCl by itself will only bind ethylene at low temperature (0°C) and high pressures (>60 atm C_2H_4).[40] Furthermore, Cu^+ incorporated into a polymer matrix has been employed in the separation of olefin/paraffin gas mixtures,[41] which is an important process in the petrochemical industry.[42] Maximum separation of ethylene/ethane and butene/butane gas mixtures were observed in the presence of the $(BF_4)^-$ anion, whereas only limited separation was achieved with the $(ClO_4)^-$ and $(SO_3CF_3)^-$ anions. This system demonstrates the unique, and potentially industrially important, information that may be obtained by correlating the structure/property relationships of the Cu(I)-based materials in the presence of Lewis acidic metal halides.

1.4. The Design of New Metal-Halide Analogs of Phosphates and Clay-type Materials

My dissertation research has focused on the synthesis of metal halide analogs of metal phosphates, phosphonates, and clay-type materials, thereby extending the structure-types of open-framework metal halides. Prior to this work only materials constructed from tetrahedral building blocks, such as zeolites, have been targeted for the design of metal-halide materials, as discussed above. Specifically, the types of metal-oxide materials targeted for the synthesis of novel metal-halide frameworks in the present work are shown in Figure 3. A polyhedral representation of the $BaV(O)_2PO_4$ lattice is shown in Figure 3a in order to emphasize that it is constructed from octahedral and tetrahedral building blocks, which are then organized into anionic layers separated by extra-framework cations.[43] In Figure 3b the octahedral and tetrahedral building blocks in an idealized structure of montmorillonite are organized into layers (Figure 3b), which are separated by both extra-framework cations and water molecules (omitted for clarity). In order to design metal halide analogs of the phosphate and clay-type materials, the oxide building blocks are replaced by the metal-halide building blocks. As described above $(CuCl_4)^{3-}$ is the charged matched and isostructural analog of $(PO_4)^{3-}$. Zirconium(IV) is utilized to link the $(CuCl_4)^{3-}$ or $(\mathbf{L}CuCl_3)^{2-}$ units because 1) it generally adopts an octahedral arrangement of halides as seen in the structure of $ZrCl_4$ shown in Figure 4, which consists of chains of edge-shared octahedra, and 2) zirconium is a strong Lewis acid utilized in a number of catalytic systems; most notably as a substituted dicylcopentadienyl in homogeneous Ziegler-Natta-type polymerization reactions.[44]

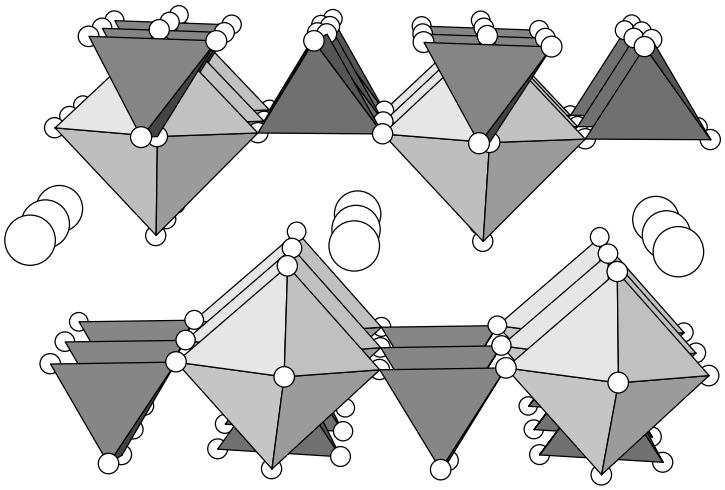

(A

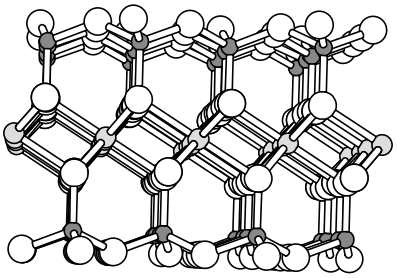

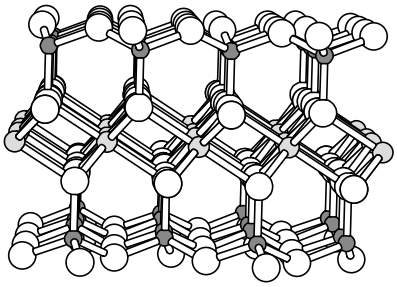

(B

Figure 1.3. A) Polyhedral representation of a vanadium phosphate, $BaV(O)_2PO_4$, shown to emphasis the octahedral and tetrahedral building blocks. B) An idealized ball and stick representation of montmorillonite, $Al_4Si_8O_{20}(OH)_4$.

1.5. Previous Work with Copper-Zirconium Materials

Relatively little work has been reported in which both copper and zirconium are incorporated within the same material. Copper-Zirconium alloys are used catalytically in the dehydrogenation of alcohols.[45,46] There are also several fluoride-based materials of copper(II) and zirconium(IV). A complete list of the known compounds constructed from copper(II) and zirconium(IV) fluorides is given in Table 1. The first materials, $Zr_2Cu_3F_{14}$•$16H_2O$ and $ZrCu_2F_8$•$12H_2O$, reported in this area were identified in 1860,[47] while the structures of these materials remained unknown for over a hundred years, until 1967 when Fischer and Wiess re-visited this system. In general, these copper(II)-zirconium(IV) fluorides consist of isolated Zr-Zr dimers, which exhibit an edge-shared octahedral or pentagonal bipyrimidyl geometry, and isolated $Cu^{II}(H_2O)_6$ octahedra that are Jahn-Teller distorted. In 1980 Müller reacted anhydrous ZrF_4 and CuF_2 in high temperature melts (>700°C), which yielded several three dimensional fluoride framework materials templated by alkali metal cations.[57,58,59] In these anhydrous materials, copper(II) and zirconium(IV) are octahedrally coordinated by fluoride anions. Based on an extensive search of the literature, there are no published accounts of materials with halides other than fluoride or that employ copper(I) in place of copper(II).[48] Synthesis of several molecular alkoxide-species of copper(I) and zirconium(IV) have, however, been recently reported by Caulton providing precedence for the proposed halide syntheses.[49,50]

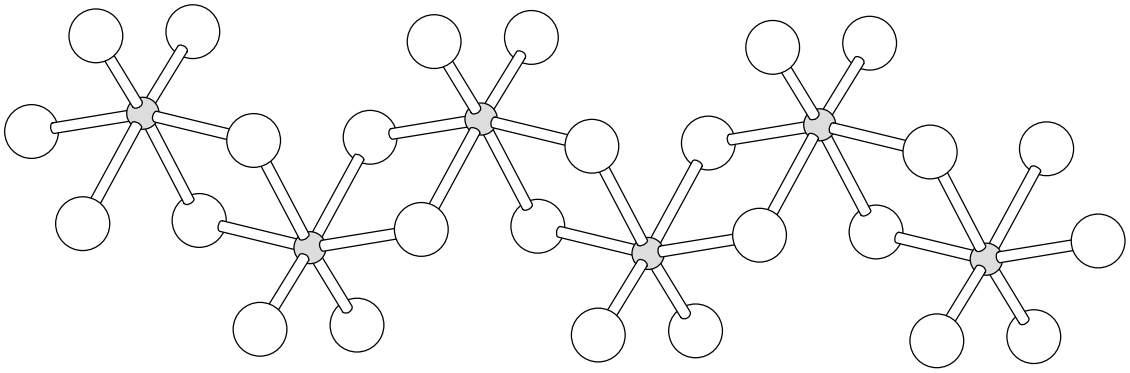

Figure 1.4. Ball and stick drawing of the edge-shared octahedral chains in $ZrCl_4$.

Table 1.1. Known Copper(II)-Zirconium(IV) Fluorides.

Compound	Reference
$Cu_3(ZrF_7)_2 \cdot 16H_2O$	51, 52
$Cu_2ZrF_8 \cdot 12H_2O$	53, 54
$CuZrF_6 \cdot 4H_2O$	55
$K_2Cu(ZrF_6)_2 \cdot 6H_2O$	56
$Cs_2Cu_3ZrF_{12}$	57
$NaCuZr_2F_{11}$	58
$CuAg_2Zr_2F_{14}$	59 (powder data only)

1.6. Scope

The methodology described above for the preparation of new metal halide materials required a considerable amount of synthetic planning and creativity. Two strategies were developed in order to obtain the desired structural control: 1) cationic directed synthesis and 2) solvent directed synthesis. Solvent directed syntheses utilize the solvent as a reaction medium, and as templates for neutral framework materials.

Cationic directed syntheses involving dimethyl ammonium cations to organize the copper(I) and zirconium(IV) primary building blocks into $(CuZrCl_6)^-$ chains, analogous to the thiophosphate chains in $(MPS_4)^-$, are discussed in Chapter 2. Hydrogen bond formation to the dimethylammonium cations results in significant distortions to the metal chloride building blocks which can be understood as second order Jahn-Teller-type distortions. In the absence of extra-framework cations, the primary tetrahedral and octahedral building blocks are assembled into a condensed three-dimensional network, Cu_2ZrCl_6, described in Chapter 3. The structure of Cu_2ZrCl_6 is complicated by a disorder

of the copper atoms about three crystallographically different sites in the unit cell. Cu_2ZrCl_6 is also shown to undergo reversible phase changes at the thermochromic transition temperature. The thermochromism is explained in terms of a structural distortion of the cuprous chloride tetrahedra, which result in a change in the energy gap as the temperature is varied. This material also exhibits an approximately temperature independent (TIP) or Van Vleck paramagnetism, which increases at the low temperature phase transition. The reactivity of Cu^+ in the presence of the Lewis acidic Zr^{4+} is then demonstrated by the solvothermal reaction of Cu_2ZrCl_6 in benzene, which breaks up the three-dimensional framework into a one-dimensional $[((bz)CuCl_3)_2Zr]_\infty$ chain that is described in Chapter 4 as a metal-halide phosphonate analog. Chains of $((bz)CuCl_3)_2Zr$ are linked along the crystallographic **c** direction *via* an edge-to-face π-stacking of the coordinated benzene molecules. The crystal packing forces are shown to influence dramatic second-order Jahn-Teller distortions making each of the two $((bz)CuCl_3)^{2-}$ units distinct. The distortions of the distinct $((bz)CuCl_3)^{2-}$ units emphasize the unique donor and acceptor properties of the Cu(I) ion. Addition of $ZrCl_4$ to the solvothermal reaction of Cu_2ZrCl_6 in benzene yields the molecular species $(bz)_2Cu_2Zr_2Cl_{10}$•bz, which loses solvent in a stepwise fashion resulting in the formation of a chain, then a layered material, respectively, as described in Chapter 5. The desolvated materials exhibits reversible binding of ethylene reminiscent of the behavior typically observed for silicate-based clays. The important findings of this work are then summarized in Chapter 6.

1.7. References

(1) Schön, J. C.; Jansen, M. *Angew. Chem., Int. Ed. Eng.* **1996**, *35*, 1286 and references therein.

(2) Boisen, M. B.; Gibbs, G. V; Bukowinski, M S. T. *Phys. Chem. Minerals* **1994**, *21*, 269.

(3) Boisen, M. B.; Gibbs, G. V; O'Keeffe, M.; Bartelmehs, K. L. *Microporous and Mesoporous Materials* **1999**, *29*, 219.

(4) Borman, S. *C &EN News* **2000**, *78 (20)*, 53.

(5) Dagani, R. *C &EN News* **2000**, *78 (20)*, 66.

(6) Breck, D. W. *Zeolite Molecular Sieves* Wiley: New York, 1974.

(7) Meier, W. M.; Olson, D. H. *Atlas of Zeolite Structure Types*; Butterworth-Heinemann: London, **1992**.

(8) Bellussi, G.; Rigutto, M. S. in *Advance Zeolite Science and Applications*, Jansen, C. J.; Stocker, M. Karge, H. G.; Weitkamp, J., eds., Elsevier: Amsterdam, 1994, pgs. 177-213.

(9) Lin, S. S.; Weng, H. S. *Appl. Catal.* **1993**, *A105*, 289.

(10) Dakka, J.; Sheldon, R. A. The Netherlands Patent 9,200,968, 1992.

(11) Bedard, R. L.; Wilson, L. D.; Bennett, J. M.; Flanigen, E. M. in *Zeolites: Facts, Figures, Future*, Jacobs, P. A.; van Santen, R. A., eds., *Stud. Surf. Sci. Catal.*, vol 49, part A, Elsevier Science Publishers B. V.: Amsterdam, 1989.

(12) Jiang, R.; Lough, A.; Ozin, G. A.; Bedard, R. L.; Broach, R. *J. Mater. Chem.* **1998**, *8*, 721.

(13) Bowes, C. L.; Ozin, G. A. *Adv. Mater.* **1996**, *8*, 13.

(14) Schnick, W.; Huppertz, H. *Chem. Eur. J.* **1997**, *3*, 679.

(15) Schnick, W.; Huppertz, H. *Angew. Chem., Int. Ed. Eng.* **1997**, *36*, 2651.

(16) Schnick, W. C*omm. on Inorg. Chem.* **1995**, *17*, 189 and references therein.

(17) For an overview see: Rouhi, A. M. *C & E News* **2000**, *78(34)*, 40.

(18) Cox, P. A. *Transition Metal Oxides: An Introduction to their Electronic Properties*; Clarendon: Oxford, 1992.

(19) Rao, C. N. R. *Transition Metal Oxides*; VCH: New York, 1995.

(20) Martin, J. D.; Dattelbaum,A. M.; Sullivan, R. M.; Thornton, T. A.; Wang, J.; Peachey, M. T. *Chem. Mater.* **1998**, *10*, 2699.

(21) Wells, A. F. *Structural Inorganic Chemistry*, 5th ed.; Oxford: Oxford, 1984.

(22) Martin, J. D.; Greenwood, K. B. *Angew. Chem., Int. Ed. Eng.* **1997**, *36*, 2072.

(23) B. J. Hathaway *Comprehensive Coordination Chemistry*; Wilkinson, G.; Gillard, R. D.; McCleverty, J. A., Eds.; Pergamon: London, 1987; vol. 5, ch 53.3.2.11, pp. 568-571.

(24) Karlin, K. D.; Gultneh, Y. *Prog. Inorg. Chem.* **1987**, *35*, 219.

(25) Karlin, K. D.; Tyeklar, Z., eds. *Bioinorganic Chemistry of Copper*; Chapman & Hall: New York, 1993.

(26) Hallnemo, G.; Olsson, T.; Ullenius, C. *J. Organomet. Chem.* **1985**, *282*, 133.

(27) Mori, S.; Nakamura, E. *Chem. Eur. J.* **1999**, *5*, 1534 and references therein.

(28) Mar Diaz-Requejo, M.; Nicasio, M. C.; Perez, P. J. *Organometallics* **1998**, *17*, 3051.

(29) Mar Diaz-Requejo, M.; Belderrain, T.; Nicasio, M. C.; Prieto, F.; Perez, P. J. *Organometallics* **1999**, *18*, 2601.

(30) Patten, T. E.; Matyhaszewshi, K. *Acc. Chem. Res.* **1999**, *32*, 895.

(31) Levy, A.T.; Olmstead, M. N.; Patten, T. E. *Inorg. Chem*. **2000**, *39*, 1628.

(32) Schaller, G. E.; Bleecker,, A. B. *Science* **1995**, *270*, 1809.

(33) Rodriguez, F. I.; Esch, J. J.; Hall, A. E.; Binder, B. M.; Schaller, G. E.; Bleecker, A. B. *Science*, **1999**, *283*, 996.

(34) Ecker, J. R. *Science* **1995**, *268*, 667 and references therein.

(35) Gatterman, L. and Koch, H. *Chem. Ber*. **1897**, *30*, 1622.

(36) Mukaiyama, T.; Banno, K.; Narasaka, K. *Chem. Lett.* **1973**, 1101.

(37) Nakamura, E.; Yamanaka, M.; Mori, S. *J. Am. Chem. Soc.* **2000**, *122*, 1826.

(38) Sullivan, R. M.; Martin, J. D. *J. Am. Chem. Soc.* **1999**, *121*, 10092.

(39) Sullivan, R. M.; Martin, J. D. in *Luminescent Materials*, McKittrick, J.; Di Bartolo, B.; Mishra, K., eds., *Proc. Mat. Res. Soc.*, **1999**, 560, 39.

(40) Gilliland, E. R.; Seebold, J. E.; Fitzhugh, J. R.; Morgan, P. S. *J. Am. Chem. Soc.* **1939**, *61*, 1960.

(41) Kim, Y. H.; Ryu, J. H.; Kang, Y. S.; Kim, H. S. *Chem Comm.* **2000**, 195.

(42) Rege, S. U.; Padiu, J.; Yang, R. T. *AIChE J*. **1998**, *44*, 799.

(43) Roca, M.; Marcos, M. D.; Amoros, P.; Alamo, J.; Beltran-Porter, A.; Beltran-Porter, D. *Inorg. Chem.* **1997**, *36*, 3414.

(44) Cardin, D. J.; Lappert, M. F.; Raston, C. L. *Chemistry of Organo-Zirconium and Hafnium Compounds*, John Wiley & Sons: New York, 1986.

(45) Molnár, A.; Domokos, L.; Katona, T.; Martinek, T.; Mulas, G.; Cocco, G.; Bertóti, I; Szépvölgyi, J. *Mater. Sci. Eng. A* **1997**, *226-228*, 1074.

(46) Molnár, A.; Bertóti, I; Szépvölgyi, J.; Mulas, G.; Cocco, G. *J. Phys. Chem. B* **1998**, *102*, 9258.

(47) Marignac, M. C. *Ann. Chim. Phys.* **1860**, *60*, 257.

(48) CuF has never been isolated.

(49) Vaartstra, B. A.; Samuels, J. A.; Barash, E. H.; Martin, J. Dd.; Streib, W. E.; Gasser, C.; Caulton, K. G. *J. Organometallic Chem.* **1993**, *449*, 191.

(50) Baxter, D. V.; Caulton, K. G. *Inorg. Chem.* **1994**, *33*, 2167.

(51) Fischer, J.; Weiss, R. *Chem. Comm.* **1967**, 328.

(52) Fischer, J.; Weiss, R. *Acta Cryst.* **1973**, *B29*, 1963.

(53) Fischer, J.; Weiss, R. *Chem. Comm.* **1967**, 329.

(54) Fischer, J.; Elchinger, R.;Weiss, R. *Acta Cryst.* **1973**, *B29*, 1967.

(55) Fischer, J.; Weiss, R. *Acta Cryst.* **1967**, *22*, 1963.

(56) Fischer, J.; Weiss, R. *Chem. Comm.* **1968**, 1137.

(57) Müller, M.; Müller, B. G. *Z. Anorg. Allg. Chem.* **1995**, *621*, 993.

(58) Müller, B. G.; Bialowons, H. *Z. Anorg. Allg. Chem.* **1996**, *622*, 1187.

(59) Müller, B. G. *Z. Anorg. Allg. Chem.* **1987**, *533*, 196.

Chapter Two:

$[H_2NMe_2]CuZrCl_6$: Hydrogen Bond Induced Distortions in a Copper Zirconium-Chloride Analog of a Thiophosphate.

Andrew M. Dattelbaum and James D. Martin*

Department of Chemistry, North Carolina State University, Raleigh, NC 27695.

(As Published in *Inorg. Chem.* **1999**, *38*, 2369)

Abstract

The copper(I)-zirconium(IV) halide, $[H_2NMe_2]CuZrCl_6$(**1**), has been synthesized and its single crystal X-ray structure was determined. The crystal undergoes a phase transition at -60ºC giving a room temperature structure with **a** = 10.1105(6), **b** = 9.9463(5), **c** = 12.7254(8), β = 110.287(5)° in the monoclinic space group C2/c, Z = 4, and a low temperature structure (-116°C) with **a** = 10.234(2), **b** = 9.427(1), **c** = 12.691(2), β = 109.90(2)° in the monoclinic space group $P2_1/c$, Z = 4. $[H_2NMe_2]CuZrCl_6$ is constructed from unique one-dimensional chains with zirconium and copper in alternating octahedral and tetrahedral coordination environments, respectively. The structural relationship between $(CuCl_4)^{3-}$ and $(PS_4)^{3-}$ is demonstrated by the analogy of this structure to that of $KNiPS_4$. The phase transition, which occurs at approximately -60°C, results in altered configurations of the dimethylammonium to metal-chloride hydrogen bonding. In addition, a remarkable distortion in the cuprous chloride tetrahedral unit is observed in the room temperature structure, whereas the zirconium chloride octahedron is distorted in the low temperature crystal structure. These distortions are discussed in terms of hydrogen-bond driven second-order Jahn-Teller-type distortions.

2.1. Introduction

Charge matching techniques have been broadly utilized to specifically tailor the properties of materials within a given structure-type. Zeolites represent a classic case where such charge matching strategies are utilized. For example, the sodalite structure is observed for silicates,[1] aluminosilicates,[2] aluminophosphates,[3] zinc arsnates,[4] etc., all of which can be considered isoelectronic or charge matched to the parent phase SiO_2. We recently demonstrated an extension of such charge matching techniques to include substitutions of framework anions in the preparation of halozeotypes, $[Cu_nZn_{m-n}Cl_{2m}]^{n-}$, which are direct analogs of aluminosilicates.[5] Our halide for oxide substitution strategy, by which novel metal halide materials are designed as charge matched analogs of metal oxides, can further be utilized to describe $(CuCl_4)^{3-}$ as a charge matched and isostructural analog of $(PO_4)^{3-}$ or $(PS_4)^{3-}$. Such phosphate analogs of early transition metals provide an entry into a new class of materials constructed from the tetrahedral, $(CuCl_4)^{3-}$, building blocks and octahedral early-transition metal halide building blocks. We report here the synthesis of a Cu(I), Zr(IV) halide material, $[H_2NMe_2]CuZrCl_6$(**1**), consisting of chains of alternating zirconium octahedra and copper tetrahedra. Such materials prepared from the redox active copper chloride and Lewis acidic zirconium chloride building blocks are attractive for potential catalytic applications. For example, the catalytic activity of copper (I) chloride in the presence of strong Lewis acids has received attention for the polymerization of olefins,[6,7] and the insertion of carbon monoxide into aromatic C-H bonds.[8,9] $AlCl_3$ is commonly employed as the Lewis acid for such catalytic systems and we have recently described the relationship of the copperhaloaluminate framework

structures to those of the aluminophosphates.[10] This report describes our initial synthetic preparations of metal-halide structural analogs to phosphates using copper chloride and Lewis acidic group IV metals.

2.2. Experimental

General Procedures. All reactions were performed under an inert atmosphere in a N_2 filled glove box or using vacuum and Schlenk techniques. CuCl was prepared from Cu metal and $CuCl_2 \cdot 2H_2O$ (Aldrich, 97%) according to a literature procedure.[11] $ZrCl_4$(99.9%) was used as received from Aldrich. Dimethylamine hydrochloride was heated under vacuum at 100°C for 24 hours in order to remove any water from the material. Benzene (Aldrich) was distilled from Na/benzophenone and stored over 4 Å molecular sieves. All powder X-ray diffraction measurements were obtained using an Enraf-Nonius Guinier camera and were indexed with respect to a silicon standard. IR spectra were measured using a Perkin Elmer 1600 series FT-IR Spectrophotometer.

2.3. Synthesis

$[H_2NMe_2]CuZrCl_6$(1). 0.099g $ZrCl_4$ (0.425mmol), 0.045g CuCl (0.454mmol), and 0.035g $[H_2NMe_2]Cl$ (0.429mmol) were placed in a thick walled (12mm O.D. 8mm I.D.) fused silica tube. On a Schlenk line, 1.0 ml of benzene was added to the reaction vessel. The reaction mixture was frozen in liquid N_2 and sealed with a torch such that the fused silica vessel was filled to 25% volume. The reaction mixture was heated to 150°C for one week then slow cooled at a rate of 0.05°C/min to yield a colorless crystalline solid from which a single crystal was isolated for an X-ray structure determination. (*Note of*

Caution: upon heating the sealed reaction vessel significant pressures are generated which can lead to vessel rupture. Appropriate shielding should be utilized such as placing the reaction vessels in a capped iron pipe during heating.) Guinier X-ray powder diffraction and elemental analysis indicated a single-phase material. This material has also been prepared single phase from reactions in superheated CH_2Cl_2. Synthesis from a melt of the reagents at 300°C resulted in greater than >95% **1** with <5% of an unidentified impurity as determined by X-ray powder diffraction. Elemental analysis: observed for $C_2H_8NCl_6CuZr$, C: 6.78%, H: 2.46%, N: 3.77%; calculated, C: 5.81%, H 1.95% and N 3.39%. IR Data (cm^{-1}): 3195 (s), 1624 (m), 1578 (m), 1457 (m), 1393(w), 1013 (m), 871 (w), 811 (m).

2.4. X-ray Structure Determination.

Room temperature crystal structure analysis of 1. A colorless, single crystal of **1** (0.42 X 0.22 X 0.12 mm) was mounted in a Pyrex capillary under a nitrogen atmosphere using silicone grease. Data were collected on an Enraf-Nonius CAD4 diffractometer at 25°C with monochromatic Mo(Kα) radiation. Lattice constants were determined by a symmetry constrained fit of 24 well centered reflections between $37°<2\theta<40°$ and their Friedel pairs. A unique hemisphere, ±h, ±k, l, was collected with 3541 independent reflections measured by $\theta/2\theta$ scans with $0°<2\theta<60°$. The data were scaled to three intensity check reflections using a five point smoothing routine. An empirical absorption correction was applied using psi scan data.

Systematic absences were consistent with the space group C2/c, which was confirmed in the subsequent refinement. All non-hydrogen atoms were found by direct

methods using the SIR92 program. The carbon and nitrogen atoms were refined isotropically and all other non-hydrogen atoms were refined anisotropically. A full matrix least squares calculation on 1379 unique reflections [$I > 2.5\sigma(I)$] were used in the final refinement using the NRCVAX programs.[12] Final residuals of R=0.028 and R_w=0.040 were obtained.

Low temperature crystal structure analysis of 1. The crystal, which was used for the room temperature data collection, was removed from the capillary under a flow of argon, placed on the end of a glass fiber, covered in silicone grease and immediately transferred to the diffractometer where it was cooled to -116°C under a stream of dry nitrogen. Data were then collected on an Enraf-Nonius CAD4-Mach diffractometer with monochromated Mo(Kα) radiation. Lattice constants were determined by a symmetry-constrained fit of 24 well centered reflections between $34° < 2\theta < 38°$ and their Friedel pairs. A unique hemisphere, ±h, ±k, l, was collected with 2010 independent reflections by ω-scans with $0° < 2\theta < 50°$. The data were scaled to three intensity check reflections using a five point smoothing routine. An empirical absorption correction was applied using psi scan data. Upon cooling a phase transition took place such that the C-centered reflections (h + k = 2n + 1) were observed indicating the space group $P2_1/c$; this was subsequently confirmed in the final refinement. All of the heavy atoms were located using a Patterson map. The nitrogen, carbon and hydrogen positions were then found using difference Fourier techniques. All non-hydrogen atoms were refined anisotropically. The hydrogen positions were idealized to N-H= 0.90 Å and C-H=0.96 Å, then refined isotropically. A full matrix least squares calculation on 1407 unique

reflections [$I > 2.5\sigma(I)$] was used in the final refinement using the NRCVAX programs.[12] Final residuals of R=0.049 and R_w=0.058 were obtained.

Variable temperature studies. Upon completing the data collection, the crystal was warmed up at 20°C intervals in order to ascertain the temperature of the phase transition. The unit cell was determined at each temperature from a set of 24 well-centered reflections. In addition, twenty of the defining reflections for the C-centering were measured at each temperature. The grease holding the crystal to the glass fiber softened at -40°C such that this crystal could not be studied further. A second crystal was mounted on the end of a glass fiber with epoxy, then coated in grease and cooled to -35°C under a cold stream of dry nitrogen on the diffractometer. Lattice constants were determined and 20 defining reflections for the C-centering were measured at approximately $5° \pm 3°$C intervals, upon cooling from -35°C to

-65°C.

Extended Hückel Calculations. Extended Hückel[13] tight binding calculations[14] were performed on the $[CuZrCl_6]^-$ using coordinates taken directly from both the room temperature and low temperature single crystal structures, and atomic parameters summarized in Table 2.1. The disorder in the copper position in the room temperature structure was modeled by utilizing twice the chain repeat unit. Atomic charges given in Table 2.2 were calculated based on six k points between (0, 0, 0) and (0, 0, c*/2).

Table 2.1. Parameters Used in EHTB Calculations.

atom	χ_i	H_{ii}(eV)	ξ_i	c_1	ξ_i	c_2
Zr	5s	-9.8700	1.81700			
	5p	-6.7600	1.77600			
	4d	-11.1800	3.83500	0.62242	1.50500	0.57822
Cu	4s	-11.4000	2.20000			
	4p	-6.0600	2.20000			
	3d	-14.0000	5.95000	0.59332	2.30000	0.57442
Cl	3s	-26.3000	2.18300			
	3p	-14.2000	1.73300			

Table 2.2. Calculated Atomic Charges for Chlorides in **1**.

Room Temp		Low Temp	
Atom	Calc. Charge	Atom	Calc. Charge
Cl(1)-long	-0.707	Cl(1)	-0.648
Cl(1)-short	-0.698	Cl(2)	-0.647
Cl(2)	-0.699	Cl(3)	-0.650
		Cl(4)	-0.648
Cl(3)	-0.731	Cl(5)	-0.726
		Cl(6)	-0.718

Table 2.3. Crystallographic data for $[N(CH_3)_2H_2]CuZrCl_6$(**1**).

formula	$[N(CH_3)_2H_2]CuZrCl_6$	
formula weight(g/mol)	413.57	
	Room Temperature	Low Temperature
temp, °C	25	-116
space group (No.)	C 2/c (15)	P 2_1/c (14)
a (Å)	10.1105(6)	10.235(2)
b (Å)	9.9463(5)	9.427(1)
c (Å)	12.7254(8)	12.691(2)
β, °	110.287(5)	109.90(2)
V (Å^3)	1200.3(1)	1151.3(3)
Z	4	4
ρ_{calcd} (mg cm^{-3})	2.244	2.386
λ(Mo K_α), Å	0.71073	0.71073
μ (cm^{-1})	39.3	40.9
R^a	0.028	0.049
$R_w{}^b$	0.040	0.058

$^aR_f = \sum(F_0 - F_c)/ F_0$. $^bR_w = [\sum(w(F_0 - F_c)^2)/ wF_0^2)]^{½}$.

Table 2.4. Atomic Coordinates and Isotropic Displacement Parameters for $[N(CH_3)_2H_2]CuZrCl_6$ (25°C and -116°C).

Room Temp.	x	y	z	B_{iso}
Zr	0	0	0	2.41(2)
Cu	-0.0080(5)	0.0605(1)	0.2409(4)	5.6(1)
Cl(1)	-0.14980(9)	-0.08332(9)	0.10606(7)	3.67(3)
Cl(2)	0.1032(1)	0.17811(9)	0.14397(6)	3.87(3)
Cl(3)	0.18643(9)	-0.1522(1)	0.10434(8)	4.44(5)
N	0.458(1)	0.120(1)	0.251(2)	10.6(4)
C(1)	0.519(2)	0.052(2)	0.181(1)	8.0(4)
C(2)	0.495(1)	0.052(1)	0.365(1)	6.5(3)

Low Temp.	x	y	z	B_{iso}
Zr	0.2503(1)	0.2538(1)	0.9996(1)	0.86(3)
Cu	0.2526(1)	0.3043(1)	0.2571(1)	1.63(4)
Cl(1)	0.1097(2)	0.1615(2)	0.1102(1)	1.26(7)
Cl(2)	0.3572(2)	0.4336(2)	0.1518(1)	1.12(7)
Cl(3)	0.4048(2)	0.3393(2)	0.8969(1)	1.23(7)
Cl(4)	0.1466(2)	0.0681(2)	0.8583(1)	1.29(7)
Cl(5)	0.4416(2)	0.0933(2)	0.1045(1)	1.35(7)
Cl(6)	0.0778(2)	0.4233(2)	0.9031(2)	1.46(8)
N	0.3286(6)	0.8023(7)	0.1954(5)	1.6(3)
C(1)	0.2500(9)	0.8129(9)	0.2763(7)	2.1(4)
C(2)	0.2366(8)	0.7821(9)	0.0782(7)	1.9(3)

B_{iso} is the Mean of the Principal Axes of the Thermal Ellipsoid.

Table 2.5. Selected bond distances (Å) for $[N(CH_3)_2H_2]CuZrCl_6$ (25°C and -116°C).

Room Temperature		Low Temperature	
Zr-Cu	3.152(5)	Zr-Cu	3.294(1)
Zr-Cu(b)	3.325(5)	Zr-Cu(b)	3.134(1)
Zr-Cl(1) ×2	2.4939(7)	Zr-Cl(1)	2.485(2)
		Zr-Cl(3)	2.501(2)
Zr-Cl(2) ×2	2.5016(7)	Zr-Cl(2)	2.523(2)
		Zr-Cl(4)	2.471(2)
Zr-Cl(3) ×2	2.4233(8)	Zr-Cl(5)	2.473(2)
		Zr-Cl(6)	2.387(2)
Cu-Cl(1)	2.496(4)	Cu-Cl(1)	2.360(2)
Cu-Cl(2)	2.328(4)	Cu-Cl(2)	2.322(2)
Cu-Cl(1)	2.311(3)	Cu-Cl(3)	2.350(2)
Cu-Cl(2)	2.261(4)	Cu-Cl(4)	2.286(2)
N(a)⋯Cl(1)	3.45(1), 3.65(1)	N⋯Cl(2)	3.374(6)
N(a)⋯Cl(2)	3.41(1)	N⋯Cl(2)	3.547(6)
N(a)⋯Cl(3)	3.54(2), 3.85(1)	N⋯Cl(3)	3.573(7)
		N⋯Cl(5)	3.333(6)
		N⋯Cl(5)	3.435(6)

2.5. Results

A summary of crystallographic data for the room temperature and low temperature structure determinations of $[H_2NMe_2]CuZrCl_6$, **1**, is given in Table 2.3, positional parameters in Table 2.4, and selected bond distances in Table 2.5. Comparable chains of $[CuZrCl_6]^-$ run along the **c**-direction in both the room temperature and low temperature structures. These chains are constructed from alternating zirconium chloride octahedra and copper chloride tetrahedra that share common edges to form a one-dimensional chain, as shown in Figure 2.1. The opposing edges of the copper chloride tetrahedra require the zirconium chloride octahedra to be linked in an orthogonal pattern along the chain, which is readily visualized by the orientation of the pairs of terminal Zr-Cl bonds on neighboring octahedra. The $[CuZrCl_6]^-$ chain is notably puckered as seen by the Zr-Cu-Zr angles of 158.40(5)° and 161.63(4)° for the RT and LT structures, respectively. The Cu-Zr-Cu angles are approximately 180°. The orientation of the alkylammonium cations provides the greatest differentiation between the RT and LT structures (Figure 2.2), however, significant distortions to the copper chloride and zirconium chloride building blocks are also observed.

Room Temperature Structure of 1. In the room temperature structure, the Cu and N atoms are located in the immediate vicinity of 2m crystallographic sites. However, an examination of the electron density map revealed multiple maxima at both sites. The electron density map around the nitrogen position revealed five regions of electron density with a clear dominance of two sites, N(a) in Figure 2.3. The shortest N···Cl contacts for each of the five possible nitrogen positions are also shown in Figure 2.3,

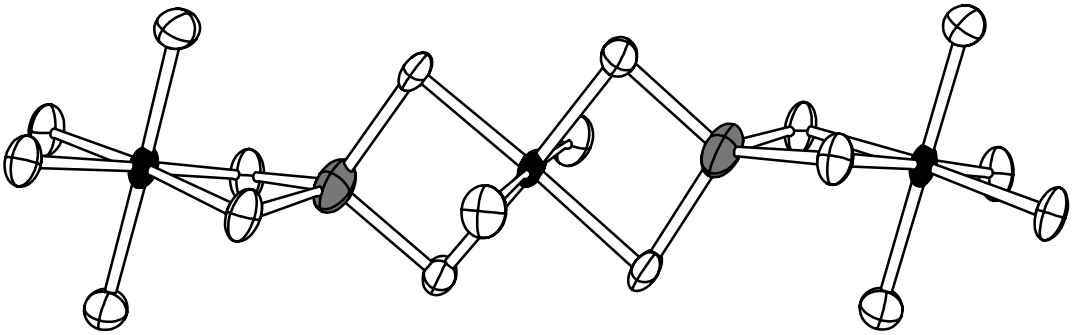

Figure 2.1. ORTEP drawings of the $[CuZrCl_6]^-$ chains in **1** (low temperature structure). Thermal displacement ellipsoids are drawn at 95%. Cu atoms are shaded gray, Zr atoms are shaded black, and Cl atoms are unshaded.

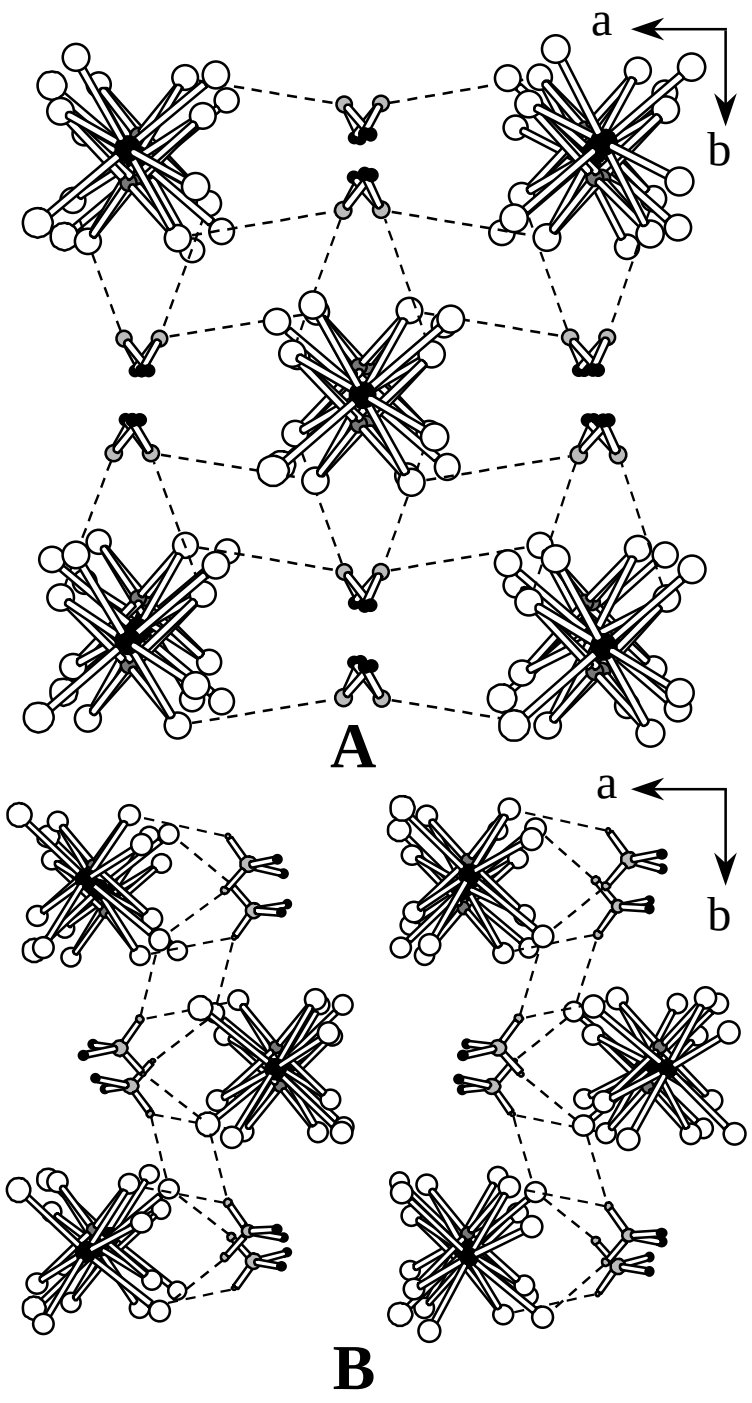

Figure 2.2. Ball and stick representations of the crystal packing in the room temperature structure, **A**, and the low temperature structure, **B**, of **1** viewed down the (001) direction. N···Cl distances <3.5Å in **A** and NH···Cl distances <2.7Å in **B** are indicated by dashed lines. Cu and N atoms are shaded gray, Zr and C are black and Cl atoms are unshaded. The disordered Cu and N(a) positions are both shown in **A**.

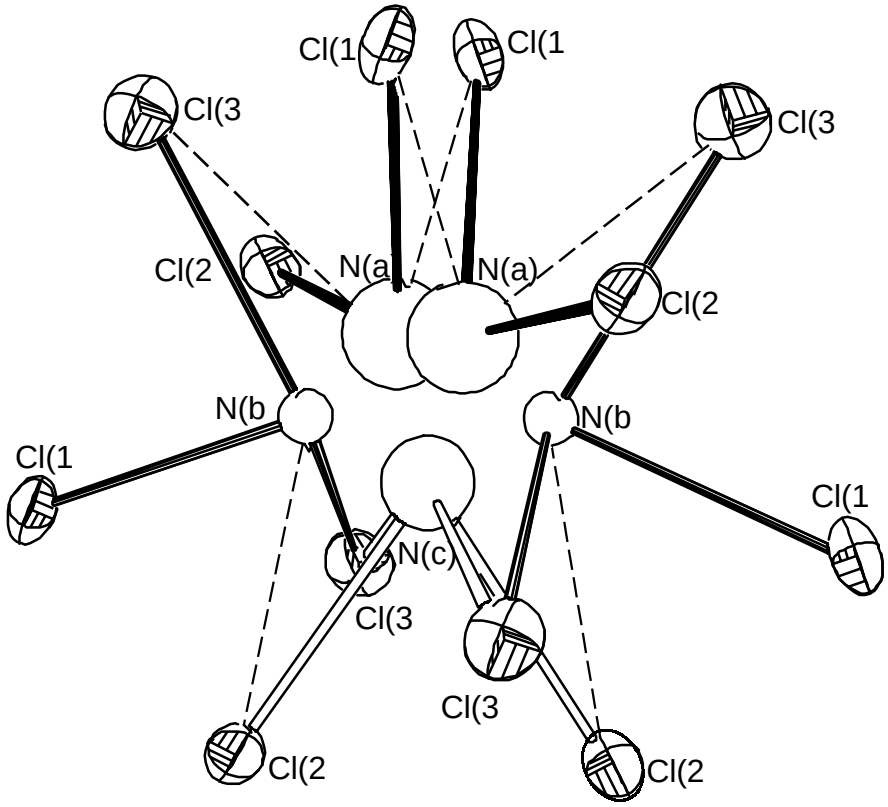

Figure 2.3. Drawing of the nitrogen positions found in the final difference map of the room temperature structure are shown along with the closest Cl contacts at each site (N···Cl < 3.49Å are solid lines, while 3.5 Å < N···Cl < 3.7Å are dashed lines). The size of the nitrogen atoms has been scaled to the relative electron density at each site.

which gives an indication of the possible N-H···Cl hydrogen bonding. Nevertheless, refinement of a simpler two site model with a 50% site occupancy of the dominant N(a) site yielded the most reasonable refinement of both occupancy and isotropic thermal parameters. The disorder of the N positions required a corresponding disorder of the carbon positions in order to achieve a reasonable structural model; this was attempted only for the two-site model of the nitrogen disorder.

The electron density map also clearly indicated that the Cu was disordered across the mirror plane, and thus was refined on general site with a 50% occupancy. The two positions are symmetrically equivalent and result from the distortion of the copper toward one of two faces within a tetrahedron of four chlorides. Figure 2.4 illustrates the coordination environment of one of the two symmetrically equivalent copper positions. The distortion coordinate is along a pseudo three-fold axis of the tetrahedral building unit and results in the lengthening of one CuCl bond, Cu-Cl(1)=2.496(4)Å, compared with Cu-Cl(1)=2.311(3), Cu-Cl(2)=2.261(4)Å and 2.328(4)Å. This distortion also results in a flattening of the tetrahedral base with basal Cl_b-Cu-Cl_b angles of 102.3(2)°, 118.38(6)° and 119.5(2)° and basal/axial Cl_b-Cu-Cl_a angles of 95.1(2)°, 106.79(6)° and 114.7(2)°. The smallest angles of 102° and 95° correspond to the edges shared with the zirconium octahedra. The thermal displacement ellipsoids for the split copper position are somewhat elongated along the Cu-Cl(1) bond.

In the room temperature structure, the $ZrCl_6$ octahedra adopt a nearly ideal octahedral geometry with the average Zr-Cl distance of 2.47Å: Zr-Cl(1) = 2.4939(7)Å, Zr-Cl(2) = 2.5016(7)Å, Zr-Cl(3) = 2.4233(8)Å. The distances to the bridging halides,

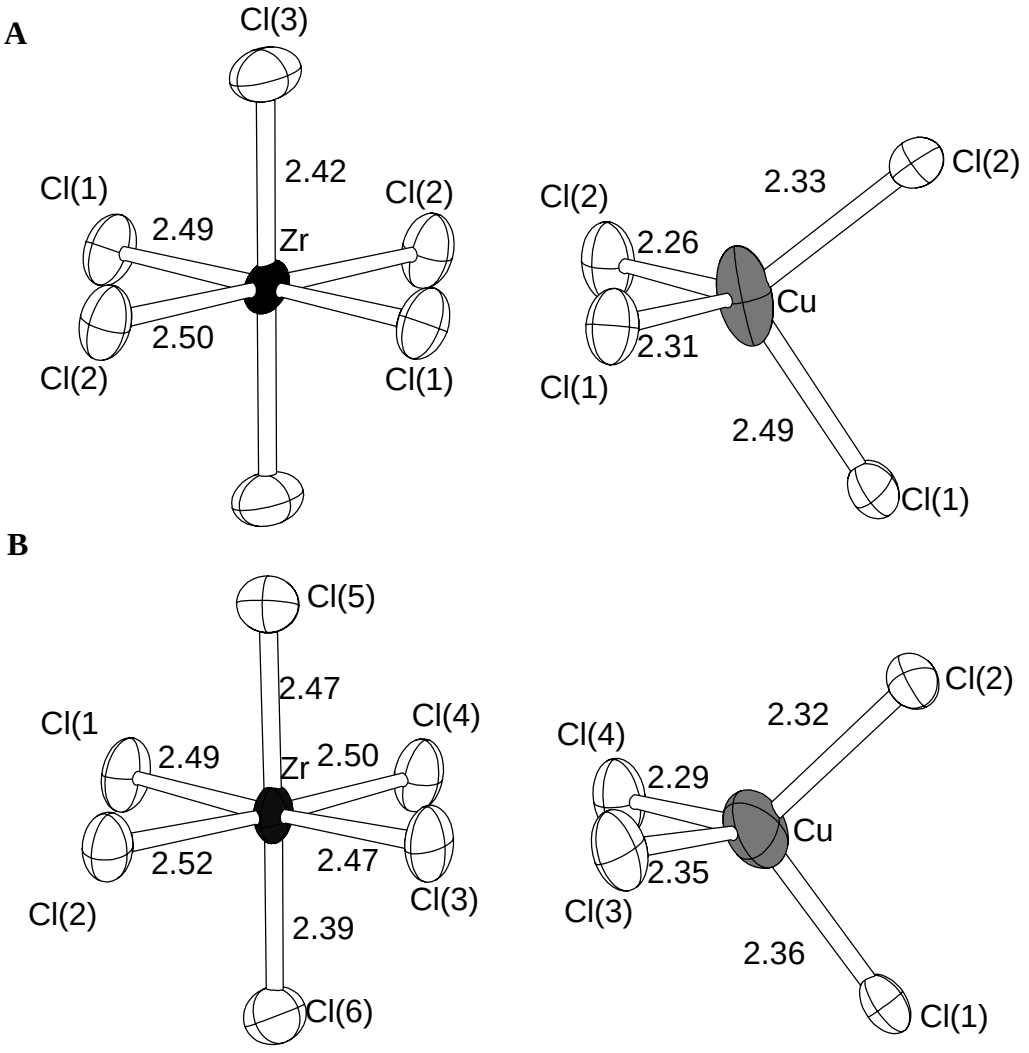

Figure 2.4. ORTEP drawings showing the distortions of the copper chloride and zirconium chloride building blocks in the room temperature, **A**, and low temperature, **B**, structures. Thermal displacement ellipsoids are drawn at 50% for the room temperature building blocks and 95% for the low temperature building blocks.

Cl(1) and Cl(2), are longer than those to the terminal chlorides as expected. However, the distance of 2.4233(8)Å is relatively long for a terminal Zr-Cl bond when compared to other terminal Zr-Cl bonds (in $ZrCl_4$, Zr-Cl_t = 2.31Å and Zr-Cl_b = 2.50Å and 2.66Å).[15]

Low Temperature Structure 1. Diffraction data were collected at -116°C and the structure determined in order to more carefully examine the influence of the hydrogen bonded ammonium cations on the metal halide chain. A phase transition from a C-centered to a primitive lattice occurred upon cooling the crystal resulting from a reorientation of the ammonium cations as seen in Figure 2.2. At low temperature, the ammonium cations reside in a site analogous to the N(b) sites of the room temperature model, alternating the direction of their dipole (protons vs. methyl groups) by ±**a**, along the **b** direction. All short N···Cl contacts linking chains along **a** are lost in favor of the formation of interchain hydrogen bonds along **b**. This reorganization from the C-centered cell (RT) to the primitive cell (LT) causes a 0.52 Å contraction of the **b** lattice constant and an expansion of the **a** lattice constant by 0.12 Å as shown in Figure 2.5. There is no significant change to the **c** lattice constant, which is also the direction of the covalent metal-halide chain.

At low temperature, the copper site is fully occupied in approximately the center of a chloride tetrahedron. Nevertheless, a remnant of the room temperature distortion in the Cu tetrahedron is present but much less obvious in the low temperature structure, with Cu-Cl bonds distances of Cl(1) 2.360(2) Å, Cl(2) 2.322(2) Å, Cl(3) 2.350(2) Å and Cl(4) 2.286(2) Å. The tetragonal distortion along the shared edges of the chain is the primary distortion from a tetrahedral geometry, as seen in the bond angles Cl-Cu-Cl = 97.38(7)

and 101.43(7) for the tetrahedral edges that are shared with the octahedra (vs. angles of 109.95(8), 114.31(8), 116.56(8) and 117.31(8) for the non-shared edges).

By contrast the zirconium chloride octahedron exhibits a striking distortion in the terminal Zr-Cl distances at low temperature. The distances to the four bridging chlorides (Zr(1)-Cl(1) = 2.485(2) Å, Zr(1)-Cl(2) = 2.523(2) Å, Zr(1)-Cl(3) = 2.501(2) Å and Zr(1)-Cl(4) = 2.471(2) Å) are consistent with expected Zr-chloride bridge distances and the Zr-Cl(6) distance of 2.387(2)Å is consistent with that expected for a terminal chloride.[15] However, the Zr-Cl(5) bond (2.473(2)Å) is elongated by almost 0.1Å in the direction of the alkylammonium cations.

Phase Transition Temperature. To determine the temperature at which the phase transition occurred, two crystals were examined upon heating (at 20°C intervals) and cooling (5°C intervals), respectively, between -116°C and -35°C. An abrupt change in the **a** and **b** lattice constants was observed around -60°C as shown in Figure 2.5. The primitive reflections that were systematically extinct in the room temperature C-centered cell were not observed to grow in upon slow cooling, presumably because of the destruction of crystal quality after passing through the phase transition which resulted in a severe loss in diffraction intensity. Upon warming this crystal back to -35°C the high-temperature lattice constants were observed indicating a reversible phase transition even though the crystal was obviously damaged.

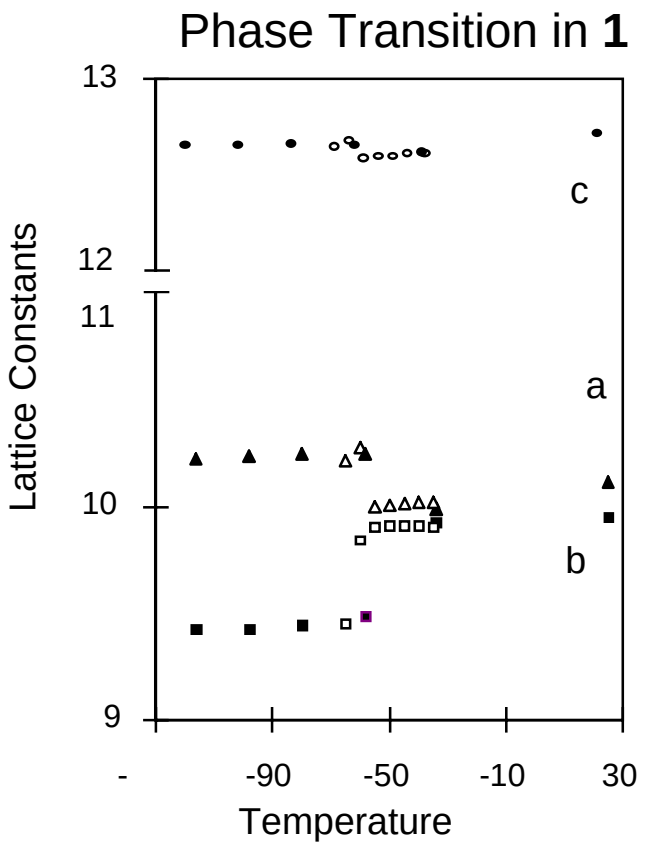

Figure 2.5. A plot of lattice constants of **1** versus temperature. The **a** lattice constant is plotted as triangles, the **b** lattice constant is plotted as squares and the **c** lattice constant is plotted as ovals. Shaded symbols represent the data for the crystal on warming and unshaded symbols represent data for a second crystal upon cooling.

2.6. Discussion

A Thiophosphate Analog. The structural motif exhibited by the chains in **1**, where octahedral building blocks are linked through edge sharing with tetrahedral units, has been previously observed for $(PPhMe_2)_2Mn_2I_4$[16] and $(DMSO)_2Cd_2I_4$[17] (DMSO = dimethylsulfoxide). However, to the best of our knowledge **1** is the first homoleptic metal-halide material and the first metal-chloride to exhibit this structure type. In the manganese and cadmium structures, one metal center is octahedrally coordinated by two terminal, neutral, ligands and four bridging iodides, while a second metal is tetrahedrally coordinated by four iodides. Such constructions in which a given metal can adopt two distinct coordination geometries is possible due to the d^5 and d^{10} configurations of Mn^{II} and Cd^{II}, respectively, which exhibit no crystal field stabilization.

A more direct structural analog was identified in the $[MPS_4]^-$ chains (M = Ni[18] or Pd[19]) in which tetrahedral thiophosphate building blocks link square planar metal centers through shared edges. The tetrahedral building block in **1**, $(CuCl_4)^{3-}$, is the charge-matched and structural equivalent of PS_4^{3-}. Similarly, with two terminal, axial chlorides, $ZrCl_2^{2+}$ is the charge-matched and structural equivalent of the square planar Ni^{2+} or Pd^{2+} building blocks in $(MPS_4)^-$. It is interesting to note, however, that only in the structure of **1** are these octahedral/tetrahedral chains puckered. Except for **1** where the M-M'-M angles are 158.40(5)° at room temperature and 161.63° at low temperature, these analogous chains all exhibit M-M'-M angles of 180°.

Understanding the Metal-Chloride Bond Distortions. Remarkable distortions to the metal chloride bonds are observed in the $CuCl_4$ tetrahedra and $ZrCl_6$ octahedra at

room temperature and low temperature, respectively. As described above, in the room temperature structure, the $CuCl_4$ unit is significantly distorted along the direction of one of the tetrahedral three-fold axes with the copper moving toward a trigonal planar face resulting in an elongation of one Cu-Cl bond by on the order of 0.2 Å. At room temperature, the zirconium chloride octahedra adopt a nearly ideal geometry in which the terminal Zr-Cl bonds are slightly elongated toward a bond distance nearly equivalent to the bridging chlorides. At low temperature (-116°C) the distortion pattern is reversed. The distortion from a tetrahedral geometry is minimized for the $CuCl_4$ units, whereas the $ZrCl_6$ octahedra are tetragonally distorted with about a 0.1 Å difference between the two terminal Zr-Cl bonds. The magnitude of these observed distortions is on the order of that expected for Jahn-Teller-type distortions. First order Jahn-Teller distortions are precluded for the d^{10}-tetrahedral and d^0-octahedral fragments. However, in **1**, second order Jahn-Teller-type distortions, whereby higher lying empty orbitals on the metal and the acceptor orbital of the hydrogen-bond donor mix with the occupied M-Cl σ^* or σ orbitals (schematically represented below), reasonably account for the observed bond distortions. Related second order distortions have previously been described for other Cu-d^{10} and Zr-d^0 systems.[20,21] In **1** these distortions also appear to be directly related to the formation of hydrogen bonds to the alkylammonium cations.

To understand these distortions, it is necessary to carefully consider the hydrogen bond contacts between the alkylammonium cations and the metal halide chains. Crystal packing requirements with respect to the orientation of the dimethyl ammonium cations in the structure of **1** appear to be quite flexible, as seen by the difference between the

ambient and low temperature structural solutions, and the possible disordered sites of the ammonium cations in the room temperature structure. Curiously, though, in the room temperature structure, the preferred orientation is such that the closest hydrogen-bonding contacts are between the ammonium cations and the bridging chlorides, which are expected to carry a smaller negative charge than the terminal chlorides. A one-dimensional Extended Hückel band structure calculation of this chain confirms that the terminal halides have a higher charge density (-0.731) than do the bridging halides (-0.698 and -0.707). Nevertheless, N···Cl contacts of 3.45(1)Å and 3.65(1)Å to bridging Cl(1) and 3.41(1)Å (*and 4.21(1)Å*) to bridging Cl(2) are observed whereas somewhat longer contacts to the terminal Cl(3), 3.54(2) Å and 3.85(1)Å, are observed. (The two distances given correspond to the distances to each of the two disordered nitrogen sites.) Although the description of the hydrogen bonding is complicated by disorder of the ammonium cation, the average contacts, 2 × 3.55Å to Cl(1), 2 × 3.81Å to Cl(2) and 2 × 3.69Å to Cl(3) suggests that the hydrogen bonding to Cl(1) > Cl(3) > Cl(2). This precisely corresponds with the direction of the dramatic Cu-Cl(1) bond elongation in the room temperature structure. Interestingly, each of the two lesser occupied nitrogen sites exhibit shorter contacts to the terminal halide (N(b)···Cl(3) = 3.61Å and 3.66Å and N(c)···Cl(3) = 3.29Å). By contrast, at low temperature no disorder in the structure is observed and the orientation of the dimethylammonium cations is consistent with the expected strongest hydrogen bond formation to the terminal chloride, NH···Cl(5) = 2.60Å and 2.63Å (N···Cl(5) = 3.33Å and 3.43Å), whereas longer contacts are observed to the bridging chlorides, NH···Cl(2) 2.63Å and 3.17Å (N···Cl(2) = 3.37Å and 3.55Å) and

NH···Cl(3) 3.06Å (N···Cl(3) = 3.57Å). This too precisely corresponds to the distortion of the Zr-Cl(5) bond at low temperature.

Distortion of the $CuCl_4$ tetrahedra. In their recent discussion of the complex coordination chemistry of copper (I) and silver (I) with relation to occurrence of ionic conduction, Burdett and Eisenstein noted that the relatively low energy of the unoccupied Cu (s,p) orbitals allows for significant mixing with occupied Cu 3d orbitals.[20] Because these orbitals are Cu-Cl anti-bonding in character, mixing with the occupied 3d orbitals results in structural distortions of which the most favored appears to be movement of the metal toward one trigonal plane of ligands. They further noted that such distortions are not observed for systems with large energetic separation between the 3d and the 4s and 4p orbitals such as is the case for zinc (II). We suggest that, as shown in Scheme I A, overlap with the unoccupied acceptor orbital of the alkylammonium hydrogen-bond

Scheme I

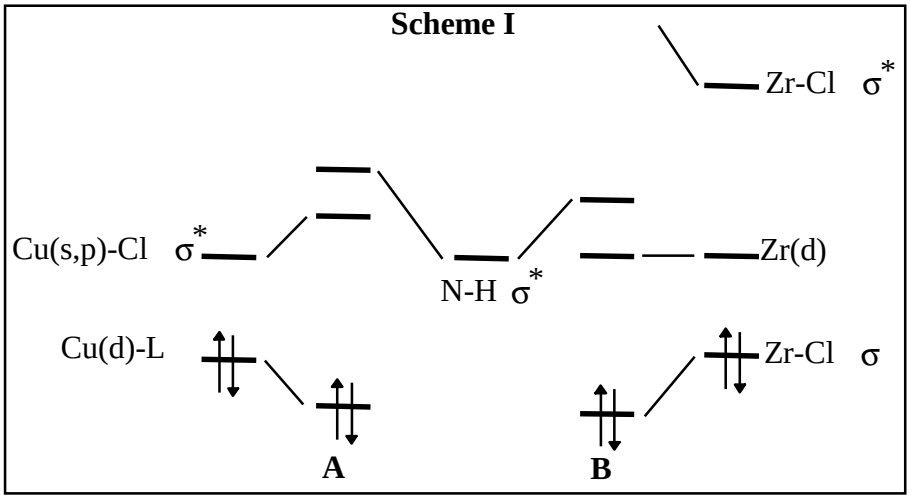

donor can further stabilize the Cu (s,p) orbital and thus reduce the promotional energy required for this second order mixing. Since the charge on the terminal chloride is greater than that of the elongated bridging chloride in the room temperature model, it is reasonable to suggest that the structural reorganization results from the stabilization brought about by the second order mixing rather than only a redistribution of charge. Why then is there a difference between the room and low temperature structures? At low temperature the ammonium cations are locked into an orientation which prevents significant mixing with the copper chloride tetrahedra. A reorganizational energy for the alkylammonium cation, which must be on the order of *k*T, must be overcome in order to bring the hydrogen bond donor into a geometry appropriate to induce the second-order orbital mixing.

Distortion of the $ZrCl_6$ octahedra. At low temperature, the ammonium cations are frozen into the geometry that maximizes the interaction between hydrogen-bond donor and the more highly charged terminal chlorides of the hydrogen-bond acceptor. While this orientational preference appears to be dominated by the electrostatic attraction between donor and acceptor, the corresponding elongation of Zr-Cl(5) by 0.1 Å with respect to Zr-Cl(6) appears also to result from a second order mixing of the occupied Zr-Cl bonding orbitals with the acceptor orbitals of the hydrogen bond donor, as shown in Scheme IB. Related distortions derived from orbital-mixing have been described by Kang, Eisenstein and Albright for other d^0 systems such as the trigonal prismatic distortion of $ZrMe_6^{2-}$ in which a second-order Jahn-Teller distortion mixes the

unoccupied metal based orbitals into the occupied M-X bonding orbitals.[21] The symmetry of the extended chain of **1** precludes significant mixing of the Zr d orbitals, however, a mixing of the low lying and empty ammonium acceptor orbital and high lying Zr p orbitals with the occupied Zr-Cl bonds results in the observed tetragonal distortion. Interestingly, only a much smaller elongation of the Zr-Cl(2) bond is observed in the low temperature structure of **1** where N···Cl distances reasonable for hydrogen bonds are present but the orientation of the NH bonds are not favorable, thus indicating the directional requirements of the orbital overlap induced distortion. While of smaller magnitude, hydrogen-bonding of the ammonium cations to the terminal Zr-Cl(3) bonds in the room temperature structure also accounts for its elongation to a distance similar to that of a bridging Zr-Cl bond.

The distortions observed in the copper chloride and zirconium chloride bonds of **1** are thus consistent with a significant charge transfer component, as opposed to a solely electrostatic model, of hydrogen bonding. Based on this structural chemistry we suggest that the orbital mixing arguments account for the magnitude and directionality of the observed metal-chloride bond distortions, but that electrostatic components likely account for a majority of the strength of hydrogen-bonds.

Acknowledgments

We would like to thank Ann E. Bunner for the contributions she made on this project as part of a summer high school research program and Dr. Paul Boyle for collecting the crystallographic data. This work was supported by the National Science

Foundation CAREER award, (DMR-9501370) and instrumentation grant (CHE-9509532). J. D. Martin is a Cottrell Scholar of the Research Corporation.

Supporting Information Available: X-ray crystallographic files, in CIF format, are available for both the room and low temperature structures of **1**. Access and/or ordering information is given on any current masthead page.

2.7. References

(1) Bibby, D. M.; Dale, M. P. *Nature* **1985**, *317*, 157.

(2) (a) Pauling, L. *Z. Kristallogr.* **1930**, *74*, 213. (b) Loens, J.; Schulz, H. *Acta Cryst.* **1967**, *23*, 434.

(3) Wilson, S. T.; Lok, B. M.; Mesina, C. A.; Cannon, T. R.; Flanigen, E. M. *J. Am. Chem. Soc.* **1982**, *104*, 1146.

(4) Nenoff, T. N.; Harrison, W. T. A.; Grier, T. E.; Stucky, G. C. *J. Am. Chem. Soc.* **1991**, *113*, 378.

(5) Martin, J. D.; Greenwood, K. B. *Angew. Chem., Int. Ed. Eng.* **1997**, *36*, 2072.

(6) Ziegler, K.; Holzkamp, E.; Breil, H. *Angew. Chem*. **1955**, *67*, 541.

(7) Natta, G. *Macromol. Chem.* **1955**, *16*, 213.

(8) Gatterman, L.; Koch, H. *Chem. Ber*. **1897**, *30*, 1622.

(9) (a) Dilke, M. H.; Eley, D. D. *J. Chem Soc.* **1949**, 2601. (b) ibid. 2613.

(10) Martin, J. D.; Leafblad, B. R.; Sullivan, R. M.; Boyle, P. D. *Inorg. Chem.* **1998**, *37*, 1341.

(11) Kaufmann, G. B. *Inorg. Synth.* **1983**, *22*, 101.

(12) Gabe, E. J.; Le Page, Y.; Charland, J.-P.; Lee, F. L.; White, P. S. *J. Appl. Crystallogr*. **1989**, *22*, 384.

(13) Hoffman, R. D. *J. Chem. Phys.* **1963**, *39*, 1397.

(14) Whangbo, M.-H.; Hoffman, R. *J. Am. Chem. Soc.* **1978**, *100*, 6093.

(15) Krebs, B. *Angew. Chem*. **1969**, *81*, 120.

(16) Beagley, B.; Briggs, J. C.; Hosseiny, A.; Hill, W. E.; King, T. J.; McAuliffe, C. A.; Minten, K. *J. Chem Soc., Chem. Comm.* **1984**, 305.

(17) Nieuwenhuyzen, M.; Wen , H.; Wilkens, C. J. *Z. anorg. Allg. Chem*. **1992**, *615*, 143.

(18) Elder, S. H.; Van der Lee, A.; Brec, R.; Canadell, E. *J. Solid State Chem*. **1995**, *116*, 107.

(19) Chondoudis, K.; Kanatzidis, G.; Sayettat, J.; Jobic, S.; Brec, R. *Inorg. Chem*. **1997**, *36*, 5859.

(20) Burdett, J. K.; Eisenstein, O. *Inorg. Chem.* **1992**, *31*, 1758.

(21) Kang, S. K.; Albright, T. A.; Eisenstein, O. *Inorg. Chem.* **1989**, *28*, 1613.

Chapter 3:

Thermochromism and Van Vleck Paramagnetism in Cu_2ZrCl_6

Abstract

The solid-state reaction of CuCl and $ZrCl_4$ in a 2:1 mole ratio, respectively, at 450°C is reported to yield Cu_2ZrCl_6, a yellow, crystalline solid. The structure of Cu_2ZrCl_6 was characterized by single crystal X-ray with **a** = 10.9892(4) Å and **c** = 6.1517(2) Å in the hexagonal space group $P\bar{3}m1$ (no. 164) with Z = 6. Cu_2ZrCl_6 was found to have a condensed three-dimensional structure that is complicated by a disorder of the two copper atoms about three crystallographically different positions within the unit cell. The disorder is understood by relating the condensed framework in Cu_2ZrCl_6 to a defect version of $ZrCl_3$, where half of the zirconium atoms are removed and the copper atoms partially occupy the tetrahedral interstices about an octahedral vacancy. Cu_2ZrCl_6 is shown to undergo thermochromic phase changes at –140°C and 400°C, which are related to a second-order Jahn-Teller distortion of the cuprous chloride building blocks. This material also exhibits an approximately temperature independent (TIP) or Van Vleck paramagnetism, which increases at the low temperature phase transition.

3.1. Introduction

Semiconducting materials generally exhibit an extended network structure with valence and conduction bands separated by a few tenths of an electron-volt up to about 3.5 eV. The ability to precisely control this energy gap, and hence the optical and electronic properties, through the incorporation of dopants has made semiconductors invaluable materials in electronic and optical devices. CuCl is a wide band gap semiconductor (E_g = 3.2eV) that has been utilized by our group for the preparation of many metal-halide analogues of metal oxides; for example, in metal halide analogs of aluminosilicate zeolites, $[CuZn_5Cl_{12}]^-$, and aluminophosphates, $CuMCl_4$ (where M = Al or Ga).[1] Copper(I) is a unique species with high-lying, filled d-orbitals and low lying unfilled s and p orbitals. Because of this, the highest occupied molecular orbital (HOMO) and the lowest unoccupied molecular orbital (LUMO) can interact, or mix, in a second-order fashion raising the energy of the higher lying orbitals and lowering the energy of the lower lying orbitals, which results in a distortion of the coordination geometry about copper.[2] In a wide band gap semiconductor, such as CuCl, these structural distortions due to orbital mixing can also lead to an observed thermochromism as the band gap changes with the distortion. Furthermore, mixing of states by similar symmetry considerations can generate a small paramagnetic moment for materials normally be thought of as diamagnetic. This type of paramagnetism has been described by Van Vleck results from the mixing excited state character into the ground state when it is placed in a magnetic field.[3]

Strong Lewis acids (electron withdrawing) have been stoichiometrically doped into the CuCl lattice with the preparation of $CuMCl_4$ materials, M = Al^{3+} and Ga^{3+}.[4] One

result of stoichiometric doping with these Lewis acids was to significantly increase the band gap of CuCl by about 1.1 eV (E_g for CuCl = 3.2 eV, $CuAlCl_4$ = 4.0 eV, and $CuGaCl_4$ = 4.2 eV)[5] by diminishing the Cu-Cl σ^* destabilization of the filled copper orbitals. Nevertheless the lowest energy electronic transition remains a $3d^{10}$ to $3d^94s^1$ copper-centered transition as is observed for CuCl. Neither aluminum nor gallium have unfilled p-orbitals low enough in energy to become involved in this lowest energy transition. By contrast, the energy gap in CuCl may be decreased by the stoichiometric incorporation of Lewis acidic transition elements with low lying unfilled d-orbitals, like Zr^{4+}. The empty orbitals of the d^0 Zr(IV) are at intermediate energy with respect to the CuCl band gap. Such stoichiometric doping of Zr^{4+} in CuCl is anticipated to change the nature of the lowest energy transition from one that is centered on copper to one that is between the high lying, filled orbitals on copper and the low lying unfilled orbitals on zirconium.

In the previous chapter, $[CuCl_4]^{3-}$ was described as a structural and electronic analog to $[PO_4]^{3-}$ or $[PS_4]^{3-}$ in $[N(CH_3)_2H_2]CuZrCl_6$ utilizing a building block approach for the design of new metal-halide analogs of targeted metal oxides.[6-8] The preparation of this material demonstrated the possibility of incorporating copper(I) and zirconium(IV) into the same material in the presence of an extra-framework cation. To further examine the control over the CuCl band gap by Lewis acid doping, CuCl and $ZrCl_4$ were reacted in the solid state. This reaction yielded Cu_2ZrCl_6, a yellow, crystalline solid, which is described as a defect $ZrCl_3$ structure. This material also exhibits interesting thermochromic and magnetic properties. Thermochromic materials undergo a reversible color change as the temperature is varied, and have found application as, for example,

holographic storage materials.[9,10] The thermochromic transitions for Cu_2ZrCl_6 are observed over very small temperature ranges around –140°C and 400°C. These thermochromic transitions are accompanied by structural phase transitions characterized by differential scanning calorimetry (DSC), as well as X-ray and neutron powder diffraction. Both the structural and thermochromic phase changes are shown to arise from a distortion of the copper chloride tetrahedra, which are allowed due to second-order mixing of the high-lying filled and low-lying unfilled orbitals on copper. Furthermore, an approximately temperature independent or Van Vleck paramagnetism is observed for Cu_2ZrCl_6, which is shown to significantly increase at the low temperature phase transition. The Van Vleck paramagnetism can be understood in terms of an indirect coupling between copper and zirconium through the chloride bridges as described below.

3.2. Experimental

General Procedures. All reactions were performed under an inert atmosphere of dry N_2 in a glove box or using Schlenk line techniques. $ZrCl_4$ (99.99%) was used as received from Aldrich. The CuCl was prepared from Cu metal and $CuCl_2$ (Aldrich) according to literature methods and further purified by sublimation.[11] All powder X-ray diffraction measurements were obtained using an Enraf-Nonius Guinier camera and were indexed with respect to a silicon standard. Diffraction patterns obtained on a Guinier camera were digitized by scanning the film using NIH *Image*.[12] Theoretical diffractograms were calculated using PowderCell 1.0.[13]

Preparation of Cu_2ZrCl_6. A sample of 0.200 g of $ZrCl_4$ (0.858 mmols) and 0.140 g of CuCl (1.72 mmols) were ground together in a mortar and pestle, then transferred to a fused silica tube (6mm I.D. × 8 cm). The reaction vessel was evacuated and sealed with a torch. The reaction was heated to 450°C (above the melting point of CuCl) in a box furnace for one day, followed by cooling at 1.0°C/min. A small temperature gradient in the furnace (ca. 5-10°C) caused the Cu_2ZrCl_6 to crystallize on the cool end of the tube. A greater than 95% yield of Cu_2ZrCl_6 was obtained with the purity of the bulk material determined by X-ray powder pattern and magnetic susceptibility measurements.

Physical Characterization. Diffuse reflectance spectra were taken using a Cary 3e UV-vis spectrometer equipped with an integrating sphere. Spectra were measured with respect to a pressed polytetrafluoroethylene powder standard. Reflectance spectra were collected as $R_\infty = R_{sample}/R_{reference}$, then plotted as the remission function, $F(R_\infty) = (1 - R_\infty)^2/2\ R_\infty$, based on the Kubelka-Munk theory of diffuse reflectance.[14]

Differential Scanning Calorimetry (DSC) data were collected on a Perkin-Elmer DSC 7 and analysis was performed by the Perkin-Elmer Thermal Analysis software. Samples of approximately 20 mg were placed into stainless steel, high-pressure pans and hermetically sealed with gold foil caps. Samples were heated from room temperature to 500°C at $10°\cdot min^{-1}$, and then cooled at the same rate. Low temperature DSC measurements were made from room temperature to –185°C at $20°\cdot min^{-1}$.

Magnetic susceptibility measurements were performed on a Quantum Designs MPMS-5S SQUID magnetometer with a 5 T magnet in fused silica magnetic susceptibility containers[15] or in a Delrin sample holder. Magnetic susceptibility

measurements were taken at fields of 0.05, 0.5, 1.0, 2.0, and 5.0 T on approximately 50 mg samples of Cu_2ZrCl_6. Susceptibility measurements at 0.5, 1.0, and 2.0 T were also made on 43.8 mg of $[NMe_2H_2]CuZrCl_6$. Measurements of the magnetization as a function of field were made at 300 K and 5.0 K.

Variable temperature X-ray diffraction experiments were performed at the X7B beamline of the National Synchrotron Light Source at Brookhaven National Laboratories. This beamline was equipped with a MAR345-camera and an image plate detector.[16] The wavelength (λ = 0.989), sample to detector distance, tilting angle of the IP and zero shift position of the IP for the data collection were determined using full Debeye-Scherrer rings of LaB_6. Samples of material, approximately 2 mm in height, were placed in 0.5 mm capillaries and cooled to 100 K using an Oxford cryostat.

X-ray structure determination of Cu_2ZrCl_6 at 298 K. A single crystal (0.24 x 0.22 x 0.12 mm) covered in silicone grease was mounted in a Pyrex capillary and sealed under a N_2 atmosphere. Single crystal X-ray data were collected on an Enraf-Nonius CAD4 diffractometer at 298 K using Mo K_α radiation (λ = 0.71073 Å). Final cell constants were determined by a symmetry constrained fit of 24 well centered reflections ($33° < 2\theta < 35°$) and their Friedel pairs. Regions of reciprocal space were examined in order to determine whether the **a** or **c-**axis should be doubled; however, zero-layer Wiessenburg and axial photographs on the CAD-4 gave no indication such a doubling of of either lattice constant. A hemisphere of data, ±h, k, ±l, with 2878 independent reflections was then collected by the $\theta/2\theta$ scan mode out to $\theta < 27°$. Data were scaled to the intensity check reflections using a five point smoothing curve fitting routine. An empirical absorption correction was applied using psi scan data.

Systematic absences were found to be consistent with the space group P-3m1, and the structure was then refined using the NRCVAX suit of programs.[17] All the zirconium and chlorine atoms were initially located by direct methods using the SIR92 program.[18] One copper site (Cu(1)) was also observed in the initial direct methods solution. Subsequent difference maps identified two additional sites that are partially occupied by copper atoms. All atoms were refined anisotropically in the final refinement. A full matrix least squares calculation using the 452 unique reflections ($I > 2.5\ \sigma(I)$) gave a final refinement with R factors of R = 0.053 and R_w = 0.087.

X-ray Structure determination of Cu_2ZrCl_6 at –116°C. The crystal used for the room temperature data collection was removed from the capillary under a flow of argon, covered in silicone grease, placed on the end of a glass fiber, and immediately transferred to the diffractometer where it was cooled to –116°C under a stream of dry nitrogen. Data were then collected on an Enraf-Nonius CAD4-Mach diffractometer with monochromated Mo(Kα) radiation. Lattice constants were determined by a symmetry-constrained fit of 24 well-centered reflections between $33° < 2\theta < 36°$ and their Friedel pairs. A unique hemisphere, ±h, k, ±l, was collected with 2434 independent reflections by ω-scans with $0° < 2\theta < 60°$. These data were scaled to three intensity check reflections using a five point smoothing routine. An empirical absorption correction was applied using psi scan data.

Systematic absences were found to be consistent with the Laue symmetry -3m1. The structure was then refined using the NRCVAX suit of programs in P-3m1. Refinement of the low temperature data yielded nearly the same structure solution as that found for the room temperature data, but with small variation in certain atom positions.

However, the low temperature data could not be as well refined as the room temperature data. All atoms were allowed to refine anisotropically in same space group, P-3m1. A full matrix least squares calculation on 885 unique reflections [$I > 1.0\sigma(I)$] was used in the final refinement using the NRCVAX programs.[12] Refinement values of R = 10.2 and R_w = 12.9 (GOF = 3.99) with the space group P-3m1 were obtained

Neutron Powder Diffraction. Cu_2ZrCl_6 (6.0 g, 0.014 mols) was sealed in a vanadium container of length 50 mm and diameter 6.0 mm (I. D.) inside a dry, He-filled glove box. Data were collected under ambient conditions, or using a closed-cycle He refrigerator for temperature control. Neutron powder diffraction data were collected using the BT-1 32 detector neutron powder diffractometer at the NIST Center for Neutron Research reactor, NBSR. A Cu(311) monochromator with a 90° take-off angle, λ = 1.5402(2) Å, and in-pile collimation of 15 minutes of arc were used. Data were collected over the range of 3-168° 2θ with a step size of 0.05°. The instrument is described in the NCNR web site (http://www.ncnr.nist.gov).

Neutron diffraction data collected at room temperature (25°C) were analyzed using the Reitveld technique[19,20] in conjunction with the GSAS (Generalized Structure Analysis System) suite of Larson and Von Dreele.[21] Lattice constants obtained from the CAD-4 data were initially used to fit the neutron, powder diffraction data. Doubling of the **c**-axis was also attempted, but it did not improve the overall fit of the data. Atomic positions obtained from the single crystal structure solution were then incorporated into the Reitveld refinement. All atoms were initially refined isotropically; however, the copper atoms were aniosotropically refined in the final least squares calculation. As was

the case for the structure solution from the single crystal data, partial occupancy of the copper atoms yielded the best refinement factors (R = 0.0739).

3.3. Results

Structure of Cu_2ZrCl_6 (1) at 25°C. A summary of the cyrstallographic data for the room temperature structure determination of Cu_2ZrCl_6 is presented in Table 3.1. Atomic positions, selected bond distances, and bond angles are listed in Tables 3.2, 3.3, and 3.4, respectively. In Cu_2ZrCl_6 two crystallographically different zirconium atoms reside in 1/6 of the octahedral interstices of the hcp chloride sublattice. Zr(1) and Zr(2) sites are located on 3-fold and $\bar{3}$-axes, respectively, with Zr(1)-Cl(1) = 2.481(3) Å × 3 and Zr(1)-Cl(3) = 2.478(3) Å × 3, and Zr(2)-Cl(2) = 2.474(2) Å × 6. Cu^+ cations were found to be disordered over three crystallographically different sites, labeled Cu(1), Cu(2), and Cu(3) with occupancies of 52(5)%, 32(1)%, and 16(1)%, respectively.

The disorder of the copper atoms observed in Cu_2ZrCl_6 prompted an examination of the experimental determination of both the space group and the unit cell in which the data was refined. Numerous attempts were initially made to find a lower symmetry space group that would allow for stoichiometric occupancy of all the copper sites. However, refinement in space groups of lower symmetry resulted in the same structural solution and always indicated structural symmetry of the original space group choice $P\bar{3}m1$. Furthermore, throughout the structure refinement I was particularly concerned with the possibility of having collected data on a twinned crystal, which could result in the apparent disorder of the copper positions. Neither Wiessenburg nor axial photographs indicated the presence of a non-merohedral twin, i.e. a material with two ordered regions

Table 3.1. Crystallographic data for Cu_2ZrCl_6 (**1**) at 25°C and -116°C.

formula	Cu_2ZrCl_6	
formula weight(g/mol)	431.22	
crystal dimensions (mm)	0.24 × 0.22 × 0.12	
crystal class	trigonal	
Temperature (°C)	25	-116
space group (No.)	P -3m1 (164)	P –3m1 (164)
a (Å)	10.9892(4)	10.9061(2)
c (Å)	6.1517(2)	12.2335(1)
V (Å^3)	643.37(3)	1260.1(2)
no. reflns for final unit cell	24	24
min and max 2theta values for final cell	33°, 35°	33°, 36°
R-merge	0.020	0.061
Z	6	6
F(000)	595.88	1184.04
ρ_{calcd} (mg cm^{-3})	3.338	3.386
λ(Mo K$_\alpha$), Å	0.71073	0.71073
μ (cm^{-1})	78.8	80.4
diffractometer	Enraf-Nonius CAD4	Enraf-Nonius CAD-Mach
scan type	θ-2θ	ω-scans
max 2θ	54.0	50.0
no. reflns measured	2878	2796
no. reflns unique	537	1402
min and max transmission	0.594, 0.997	0.597, 0.995
no. obs. data $I_{net}>2.5\sigma(I)$	452	931 (>1.0σ(I))
number of parameters in least-squares	42	79
R[a]	0.053	0.103
R_w[b]	0.087	0.111
GOF[c]	2.87	4.52
min and max peak heights on final DF map (e$^-$/Å^3)	-1.61, 1.62	-3.48, 5.76

[a]$R_f = \Sigma(F_0 - F_c)/ F_0$. [b]$R_w = [\Sigma(w(F_0 - F_c)^2)/ wF_0^2)]^{½}$
[c]$GOF = [\Sigma(w(F_0 - F_c)^2)/(\text{No. of reflns.} - \text{No. of parameters})]^{½}$

Table 3.2. Atomic Coordinates and Isotropic Displacement Parameters for Cu_2ZrCl_6 (**1**) at 25°C.

	Occupancy[37]	x	y	z	Biso
Zr(1)	1.0	1/3	2/3	0.0244(2)	1.64(5)
Zr(2)	1.0	0	0	1/2	1.52(6)
Cu(1)	0.516(50)	0.2279(3)	0.7721(3)	0.4344(6)	6.2(2)
Cu(2)	0.317(10	0.1083(4)	0.8917(4)	0.9122(1)	6.3(3)
Cu(3)	0.167(10)	0.4242(8)	0.5758(8)	0.609(2)	5.8(5)
Cl(1)	1.0	0.4405(1)	0.5595(1)	0.2539(4)	2.31(9)
Cl(2)	1.0	0.1070(1)	0.8930(1)	0.2716(4)	2.35(8)
Cl(3)	1.0	0.2261(1)	0.7739(1)	0.7958(4)	2.56(8)

Table 3.3. Bond distances (Å) for Cu_2ZrCl_6 (**1**) at 25°C and -116°C.

25°C		-116°C			
Zr(1)-Cl(1)	2.481(3) × 3	Zr(1)-Cl(3) × 3	2.492(4)	Zr(3)-Cl(1)	2.464(6) × 3
Zr(1)-Cl(3)	2.478(3) × 3	Zr(1)-Cl(5) × 3	2.509(3)	Zr(3)-Cl(2)	2.480(6) × 3
Zr(2)-Cl(2)	2.474(2) × 6	Zr(2)-Cl(1)	2.483(2) × 3		
		Zr(2)-Cl(6)	2.486(5) × 3		
Cu(1)-Cl(1)	2.308(3) × 2	Cu(1)-Cl(2)	2.124(7)	Cu(4)-Cl(1) × 2	2.277(5)
Cu(1)-Cl(2)	2.511(6)	Cu(1)-Cl(5) × 2	2.274(4)	Cu(4)-Cl(3)	2.291(7)
Cu(1)-Cl(3)	2.223(4)	Cu(1)-Cl(6)	2.493(6)	Cu(4)-Cl(4)	2.493(6)
Cu(2)-Cl(2)	2.340(7) × 2	Cu(2)-Cl(3)	2.155(8)	Cu(5)-Cl(2)	2.61(1)
Cu(2)-Cl(2)	2.211(6)	Cu(2)-Cl(6)	2.330(7)	Cu(5)-Cl(1)	2.143(7)
Cu(2)-Cl(3)	2.354(7)	Cu(2)-Cl(6) × 2	2.344(5)	Cu(5)-Cl(2) × 2	2.251(6)
Cu(3)-Cl(1)	2.204(9)	Cu(3)-Cl(1)	2.61(2)	Cu(6)-Cl(1)	2.23(1)
Cu(3)-Cl(1)	2.71(2)	Cu(3)-Cl(2) × 2	2.20(1)	Cu(6)-Cl(1) × 2	2.22(1)
Cu(3)-Cl(3)	2.226(7) × 2	Cu(3)-Cl(5)	2.14(1)	Cu(6)-Cl(5)	2.81(1)

Table 3.4. Bond angles (deg.) for Cu_2ZrCl_6 (**1**) at 25°C.

Cl(1)-Zr(1)-Cl(1)	90.81(8) × 3	Cu(1)-Cl(1)-Cu(1)	97.7(1)
Cl(1)-Zr(1)-Cl(3)	179.87(8) × 3	Cu(1)-Cl(1)-Cu(3)	57.3(2)
Cl(1)-Zr(1)-Cl(3)	89.10(7) × 6	Cu(1)-Cl(1)-Cu(3)	106.1(2)
Cl(3)-Zr(1)-Cl(3)	90.99(8) × 3	Cu(1)-Cl(2)-Cu(2)	112.9(2)
		Cu(1)-Cl(2)-Cu(2)	125.9(2)
Cl(2)-Zr(2)-Cl(2)	180.0(1) × 3	Cu(1)-Cl(3)-Cu(3)	58.3(3)
Cl(2)-Zr(2)-Cl(2)	90.92(8) × 6	Cu(1)-Cl(3)-Cu(2)	108.6(2)
Cl(2)-Zr(2)-Cl(2)	89.08(8) × 6		
		Cu(2)-Cl(2)-Cu(2)	61.4(2)
Cl(1)-Cu(1)-Cl(1)	99.9(1)	Cu(2)-Cl(2)-Cu(2)	99.4(2)
Cl(1)-Cu(1)-Cl(2)	101.5(2) × 2	Cu(2)-Cl(3)-Cu(3)	131.4(1)
Cl(1)-Cu(1)-Cl(3)	119.2(1) × 2		
Cl(2)-Cu(1)-Cl(3)	112.6(2)	Cu(3)-Cl(1)-Cu(3)	79.9(4)
		Cu(3)-Cl(3)-Cu(3)	84.6(2)
Cl(2)-Cu(2)-Cl(2)	118.6(2) × 2		
Cl(2)-Cu(2)-Cl(2)	97.8(3)	Zr(1)-Cl(1)-Cu(1)	84.53(1)
Cl(2)-Cu(2)-Cl(3)	108.3(4)	Zr(1)-Cl(1)-Cu(3)	116.6(4)
Cl(2)-Cu(2)-Cl(3)	106.1(2) × 2	Zr(1)-Cl(1)-Cu(3)	163.5(2)
Cl(1)-Cu(3)-Cl(1)	100.1(4)	Zr(1)-Cl(3)-Cu(1)	123.7(2)
Cl(1)-Cu(3)-Cl(3)	123.9(2) × 2	Zr(1)-Cl(3)-Cu(2)	127.7(2)
Cl(1)-Cu(3)-Cl(3)	98.1(5) × 2	Zr(1)-Cl(3)-Cu(3)	81.9(3)
Cl(3)-Cu(3)-Cl(3)	105.2(3)		
		Zr(2)-Cl(2)-Cu(1)	121.9(1)
		Zr(2)-Cl(2)-Cu(2)	125.3(2)
		Zr(2)-Cl(2)-Cu(2)	85.5(2)

within the solid that oppose each other in some fashion. Flack's method of left coset decomposition was then used to determine the possible twin laws for the merohedral or perfect twin.[22] The twin laws obtained were identical to those published by Le Page for the Laue group $\bar{3}$m1.[23] Information about each possible twin law was incorporated into the structure model using the twin refinement options provided by SHELXL97.[24] None of the possible twin laws led to an improvement of the refinement factors. Therefore, a structural model with partially occupied copper position for Cu_2ZrCl_6 appears to be correct, and is not the result of data collected on a twinned crystal.

ORTEP drawings of the chain-type structure defined by the occupancy of each copper site, respectively, are shown in Figures 3.1a-c. The Cu(1) and Cu(3) sites are in the vicinity of the 3-fold axis such that a copper-shared three-membered ring of copper chloride tetrahedra is observed. These cuprous chloride rings are capped by $Zr(1)Cl_6$ octahedra as seen in Figures 3.1a and 3.1c. The tetrahedral arrangement of the three copper chloride tetrahedra and one $Zr(1)Cl_6$ octahedra shown in Figures 3.1a and 3.1c can be described as Cu_3ZrCl_9 adamantane-like building units. Occupation of the Cu(1) sites result in the adamantane-type building blocks pointed along the **+c** direction, whereas occupation of the Cu(3) site results in the building blocks pointed in the opposite direction. These building units are then stacked along **c** to form one-dimensional chains. When plotted as one chain the Cu(1) and Cu(3) positions occupy the six tetrahedral interstices surrounding an empty octahedral interstice. These two copper sites each have a trigonal pyramidal coordination of halides, and are approximately related by a $\bar{3}$-axis along the chain as seen in Figure 3.2a. However, the $\bar{3}$ symmetry is destroyed by a 0.2 Å elongation of the apical Cu-Cl distance at the Cu(3) trigonal pyramid, Cu(3)-Cl(1) =

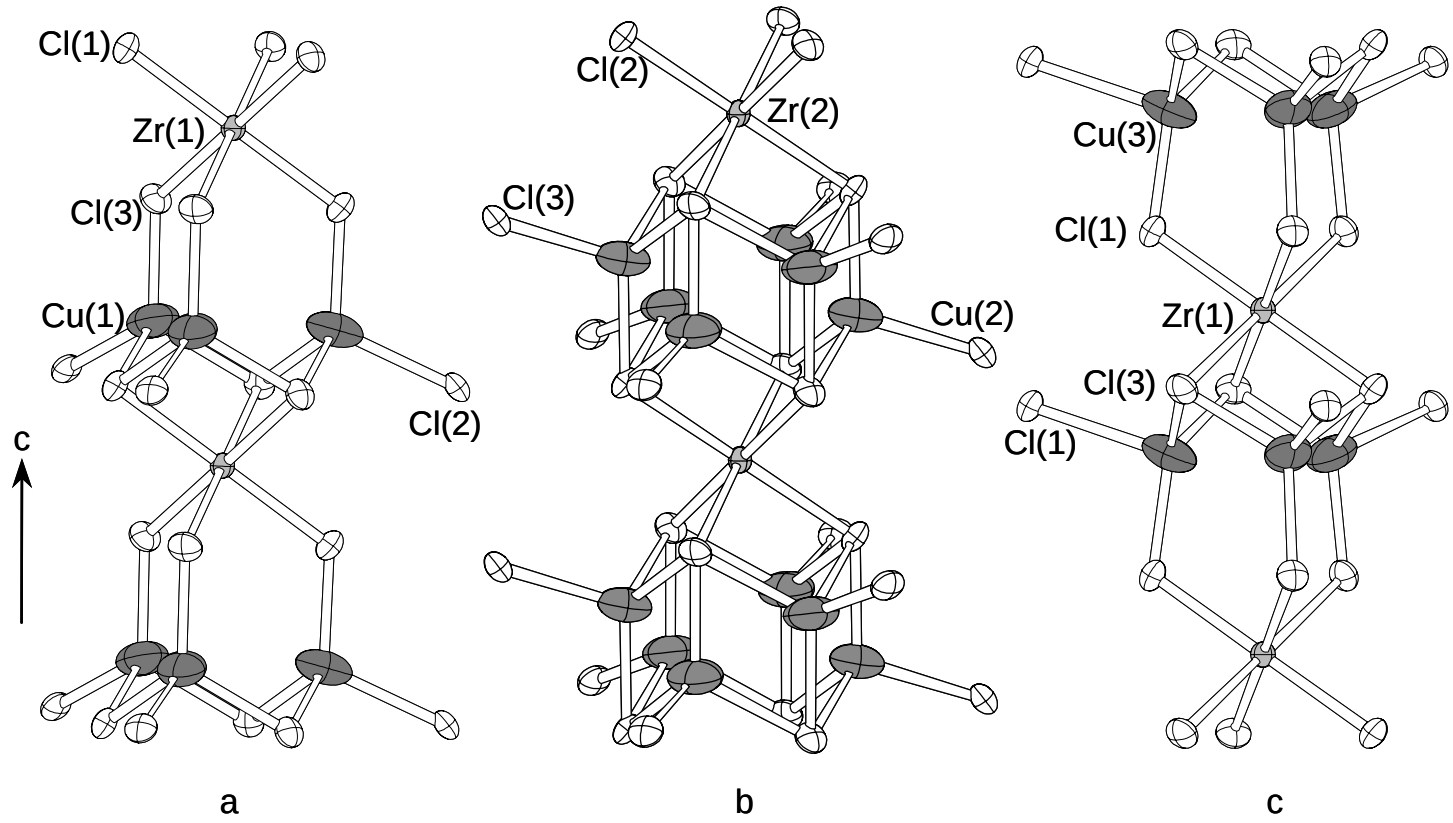

Figure 3.1. ORTEP plot of the chains in Cu_2ZrCl_6, which are constructed from adamantane-type building blocks. Thermal displacement ellipsoids are shown at the 50% confidence level.

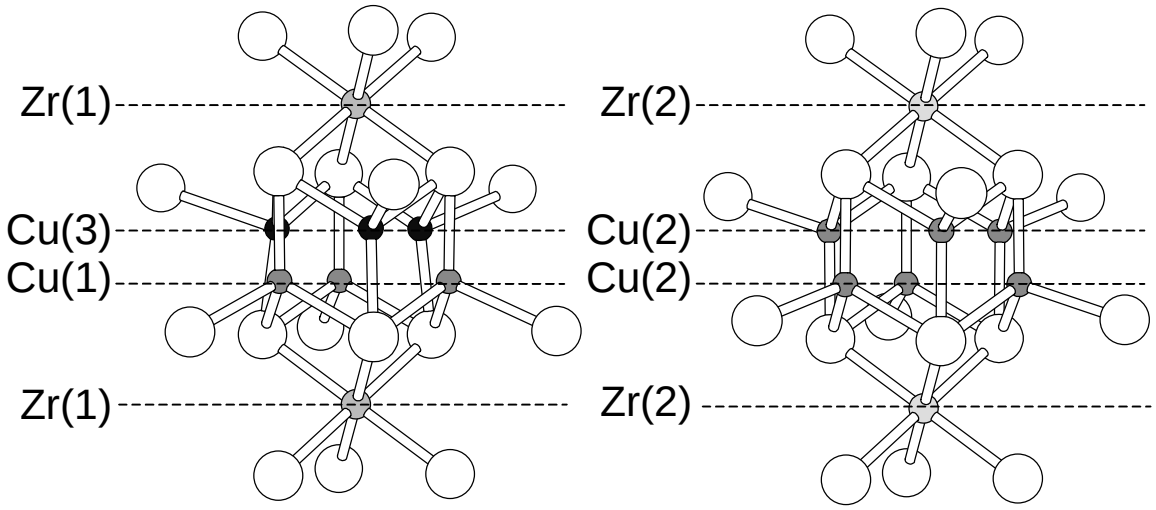

Figure 3.2. Ball and stick drawing of the (a) $Cu(1)Cu(3)Zr(1)Cl_x$ and (b) $Cu(2)Zr(2)Cl_x$ chains in Cu_2ZrCl_6. Unshaded spheres are Cl, darker, medium-sized spheres are Zr(1), while the lighter, medium-sized spheres are Zr(2). Cu atoms are the smallest shaded spheres shown (convention used throughout).

2.71(2) Å, compared to the apical distance at Cu(1), Cu(1)-Cl(3) = 2.511(6) Å. The other three basal Cu-Cl distances of the cuprous chloride coordination sphere are similar with Cu(3)-Cl(3) = 2.226(7) Å × 2 and Cu(3)-Cl(1) = 2.204(9) Å, and Cu(1)-Cl(1) = 2.308(3) × 2 and Cu(1)-Cl(2) = 2.223(4) Å. In contrast, Cu(2) sites surround a $\bar{3}$-site, which generates six equivalent copper sites between every two $Zr(2)Cl_6$ octahedra, as seen in Figures 3.1b and 3.2b. The Cu(2)-Cl bond distance are approximately equivalent with Cu(2)-Cl(2) = 2.340(7) Å × 2 and 2.211(6) Å, Cu(2)-Cl(3) = 2.354(7) Å. Thus, occupancy of the Cu(2) sites results in a $Zr_2Cu_6Cl_{18}$ bicapped trigonal anti-prism with the two $Zr(2)Cl_6$ octahedra capping the Cu_6 trigonal anti-prism.

Full occupancy of any one copper site would result in the formation of one of the three different lattices shown in Figures 3.3a-c each with the same Cu_2ZrCl_6 stoichiometry. In each figure, the zirconium and chloride positions remain unchanged to simplify the comparison between the distinct network constructions. As seen in Figure 3.3a, where the Cu(1) site is fully occupied, the lattice consists of chains of adamantane-like Cu_3ZrCl_6 building blocks (circled) running along the **+c** direction, which are connected laterally along **a** and **b** by chloride bridges to isolated $Zr(2)Cl_6$ octahedra. Each $Zr(2)Cl_6$ octahedra link six different chains through long, apical Cu(1)-Cl(3), 2.511(6) Å, bonds. Full occupancy of the Cu(3) site results in analogous chains that are connected to each other by the bridging Cl(1), which is apical to the adamantine building block of one chain, and inner to the adamantine building block of a neighboring chain, Cl(1)-Zr(1) = 2.481(3) Å and Cl(1)-Cu(1) = 2.308 Å. In this network, the building blocks are pointed in the opposite direction. Adjacent chains are connected $Zr(2)Cl_6$ octahedra are completely isolated in channels from the chains (Figure 3.3c). When the

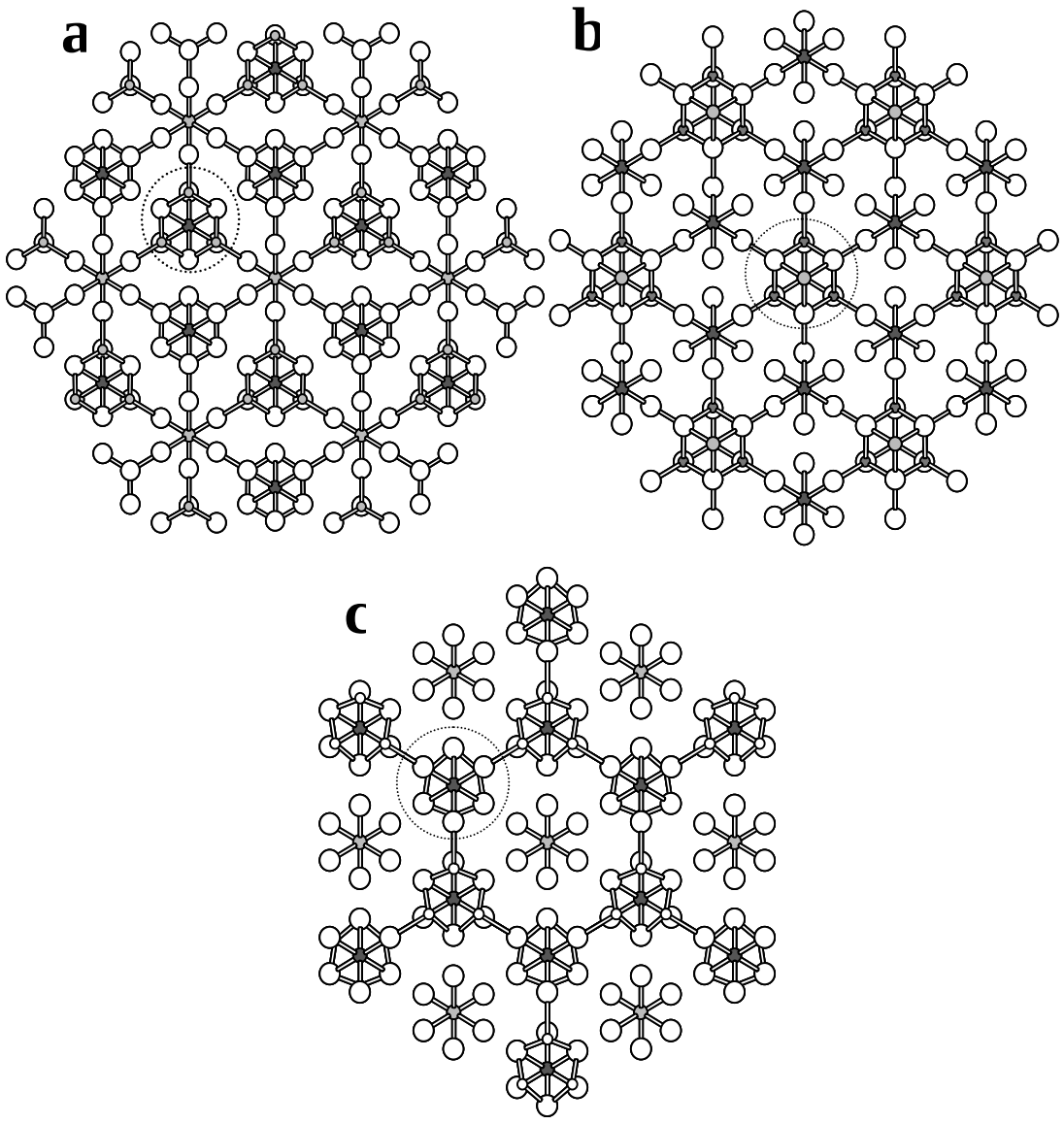

Figure 3.3 **a-c** are **b**all and stick representations viewed down the **c**-direction of the three lattice types that would be obtained occupying only only one copper site, Cu(1), Cu(2), or Cu(3), respectively is occupied in Cu_2ZrCl_6.

Cu(2) sites are fully occupied, as shown in Figure 3.3b, three chains of bicapped trigonal anti-prisms are joined *via* Cu(2)-Cl(3)-Zr(1) bridges. This leaves three terminal Zr(1)-Cl(1) contacts for the network linking the $ZrCl_6$ octahedra.

X-ray powder Data. To further verify that the structure of Cu_2ZrCl_6 is best described by the model presented above with disordered copper sites, and is not a mixture of three distinct phases, X-ray powder patterns were calculated for the structures that would be observed by fully occupying only one of the three copper sites (Figures 3.4a-c), and are given in Figure 3.4a-c, respectively. These are then compared to the experimentally observed powder pattern of Cu_2ZrCl_6 shown in Figure 3.4e. In Figure 3.4d, a powder pattern was calculated in which all three copper positions are partially occupied in accordance with the structural solution presented above. The calculated pattern for the disordered model (Figure 3.4d) is most similar to the observed pattern for Cu_2ZrCl_6. The most notable difference between Figures 3.4a-c and the observed pattern, is the absence of the (100) reflection at 9.3 degrees 2θ. A histogram of the intensity data versus 2θ obtained from the single crystal at 25°C on the CAD-4 diffractometer is shown at the bottom of Figure 3.4. Notice that the (100) reflection was also absent from the single crystal data consistent with the experimentally observed X-ray powder pattern for the bulk material.

Neutron Powder Diffraction data at 25°C. A Reitveld refinement of the neutron powder diffraction data is shown in Figure 3.5. Table 3.5 lists the atomic parameters, as well as crystallographic data obtained from this analysis. Neither the lattice constants nor the atomic positions significantly changed from the starting values, which were taken directly from the single crystal structural model. As was the case for

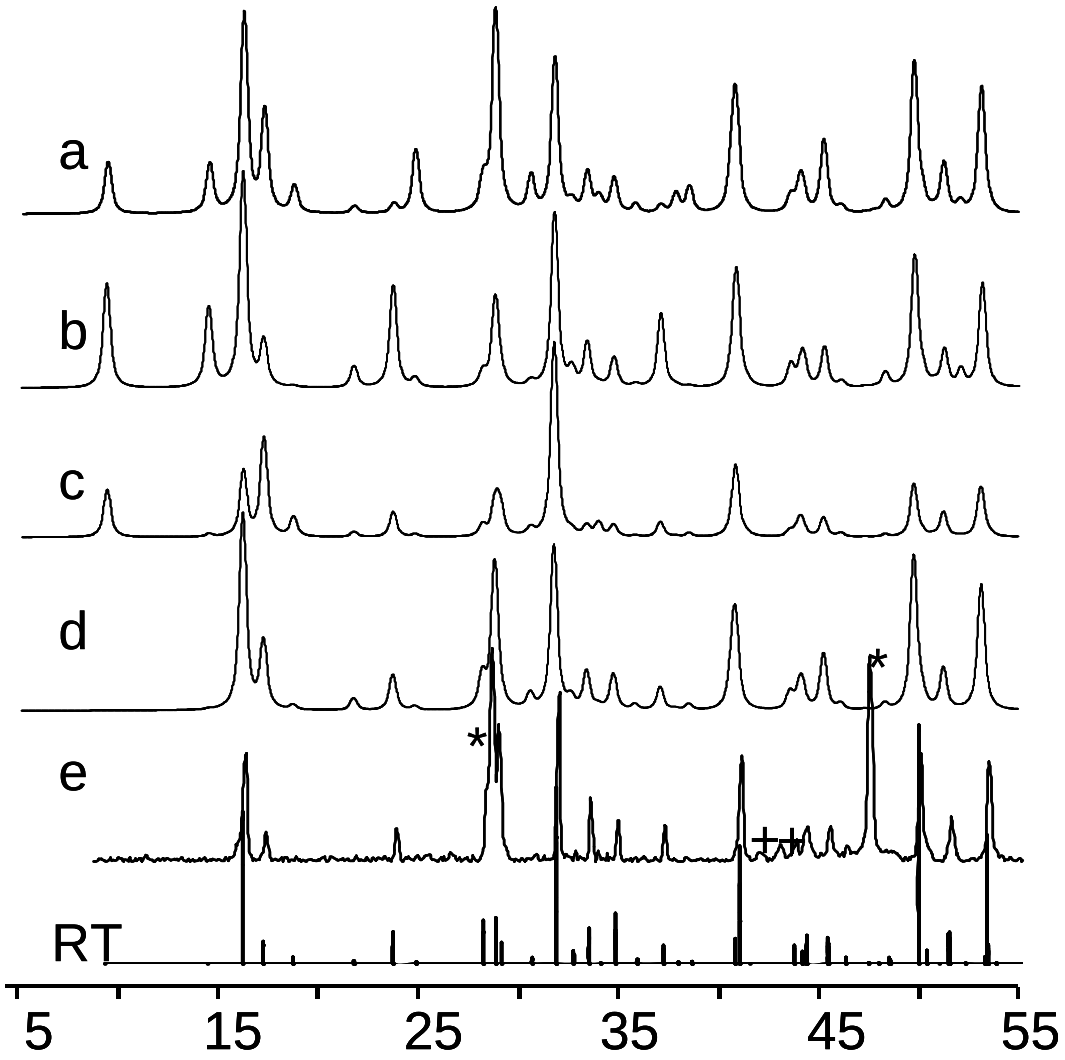

Figure 3.4. a-c are calculated powder patterns corresponding to the lattices shown in Figure 3.3**a-c**, respectively, in which only one copper site is fully occupied. **d** is the calculated XRD pattern for disordered model of the final refinement of Cu_2ZrCl_6 at 25°C, while the experimental XRD pattern for a bulk sample of Cu_2ZrCl_6 is shown in **e**. Figure **3.4f** is a histogram of the intensity data versus two theta collected on the single crystal at 25°C. Reflections marked by ***** are due to the silicon standard, while those markedwith a + are instrumental artifacts.

Table 3.5. Summary of the Reitveld refinement of the room temperature neutron powder diffraction data for Cu_2ZrCl_6.

	occupancy	x	y	z	B_{iso}
Zr(1)	1.0	0.3333	0.6667	0.0241	2.3
Zr(2)	1.0	0.0000	0.0000	0.5000	2.1
Cu(1)	0.628(30)	0.2272	0.7727	0.4348	7.0
Cu(2)	0.226(10)	0.1085	0.8915	0.9118	3.9
Cu(3)	0.146(10)	0.4250	0.5750	0.6092	1.9
Cl(1)	1.0	0.4402	0.5598	0.2549	3.6
Cl(2)	1.0	0.1069	0.8931	0.2408	2.1
Cl(3)	1.0	0.2262	0.7738	0.7953	1.8

Lattice parameters for powder data: *a* (Å) 10.9646(4)
c (Å) 6.1409(3)

R = 0.0739

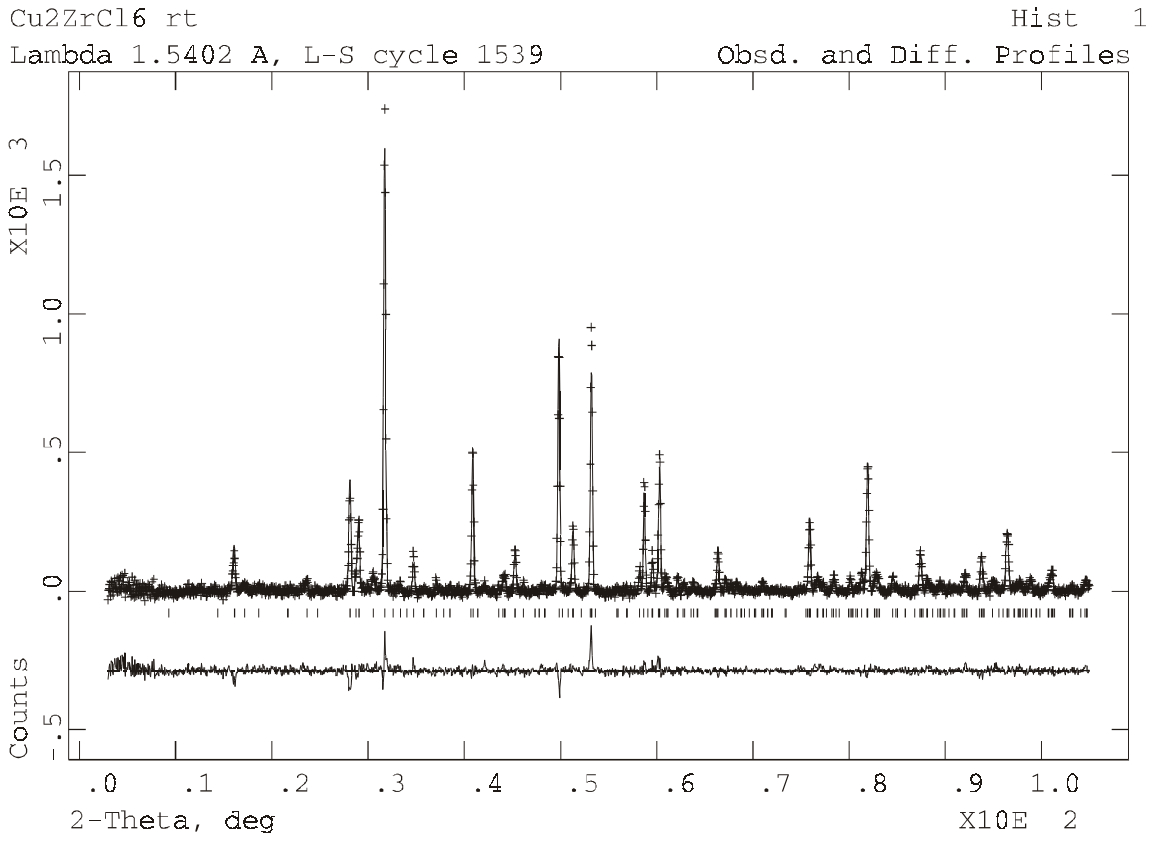

Figure 3.5. Reitveld refinement of the neutron powder diffraction data for Cu_2ZrCl_6 at 25°C.

the structure solution from the single crystal data, partial occupancy of the copper atoms yielded the best refinement of the powder data. The copper atoms, Cu(1), Cu(2), and Cu(3), were refined to have the following occupancy factors, 62(3)%, 23(1)%, 15(1)%, respectively.

X-ray Structure of Cu_2ZrCl_6 at –116 °C. A low temperature data set was collected on the same single crystal used for the room temperature data collection in an attempt to "freeze out" the disorder. At –116 °C the **c**-axis was observed to double, while the **a** and **b**-axes remained essentially unchanged (Table 3.1). Data were then collected on the doubled cell and a structure solution obtained. The low temperature structure solution also exhibited a disordered model of the structure analogous to that described above. The distribution of copper atoms remained essentially identical to the room temperature phase, although there are twice as many copper sites in the unit cell consistent with the doubled **c** axis. The most significant difference between the room temperature and the low temperature phase is observed in the coordination about the site labeled Cu(2) in the room temperature phase, which is split into Cu(2) and Cu(5) in the low temperature structure. The Cu-Cl distances about Cu(5), 2.61(1) Å, Cl(3), 2.143(7) Å, Cl(1), and 2.251(6) Å × 2, Cl(6), are significantly distorted toward a trigonal planar type geometry compared to the Cu-Cl distances about Cu(2) at low temperature, 2.155(8) Å, Cl(3), 2.330(7) Å, Cl(6), and 2.344(5) Å × 2, Cl(6), which are more similar to the Cu(2)-Cl bond distances at room temperature (Table 3.3). This distortion gives rise to the observed doubling of the **c** axis.

Low Temperature (LT) Neutron and X-ray Powder Diffraction data. Neutron and X-ray powder diffraction data of Cu_2ZrCl_6 were collected at –173 °C, which

are shown in Figures 3.6 and 3.7, respectively. In both figures, the room temperature patterns are shown for comparison. In Figure 3.6, a large background between 15 and 25 degrees 2θ is due to the quartz capillary sample holder. Between room temperature and –173 °C, a structural phase transition occurs resulting in a lower symmetry structure with an expanded unit cell. This structural phase transition corresponds to a thermochromic transition from a yellow to a colorless material (described below). Most reflections of the low temperature diffractograms are shifted to lower 2θ values with respect to the room temperature pattern. Several new reflections are also observed in the LT X-ray pattern, for example at 14.24, 19.53, and 20.67 degrees 2θ (Figure 3.6). In addition to new reflections at 31.95° and 39° in the LT neutron pattern, reflections at 50 and 51 degrees 2θ were observed to exhibit sufficient resolution to distinguish them from the apparent single reflections in the RT pattern. It has not yet been possible to unequivocally determine the structure or unit cell of the LT phase from either the neutron or X-ray LT powder data. However, both data sets indicate a lowering of the overall lattice symmetry with the presence of the new diffraction reflections.

Diffuse Reflectance Spectroscopy (DRS). The diffuse reflectance spectrum for Cu_2ZrCl_6 is shown in Figure 3.8. The onset of absorption at approximately 20,000 cm^{-1} is consistent with the yellow color observed for the room temperature material. An increased absorption is observed up to the broad plateau starting at 26,000 cm^{-1}. This absorption spectrum is consistent with a wide band gap semiconductor of ca. 23,400 cm^{-1} (2.9 eV). This is shown in comparison to CuCl, which has a band gap 3.2eV.[26,27] The other starting material, $ZrCl_4$, has a band gap in the vacuum ultraviolet, and is unobservable with our instrumentation.

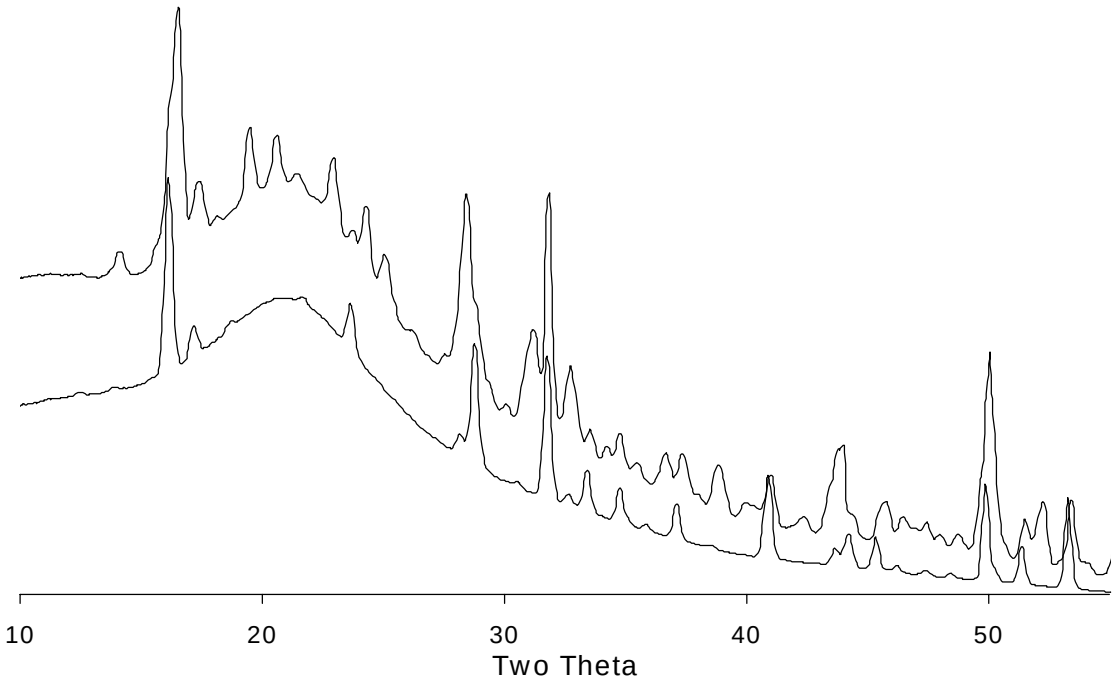

Figure 3.6. X-ray diffraction data for Cu_2ZrCl_6 at (a) 25°C and (b) –173°C.

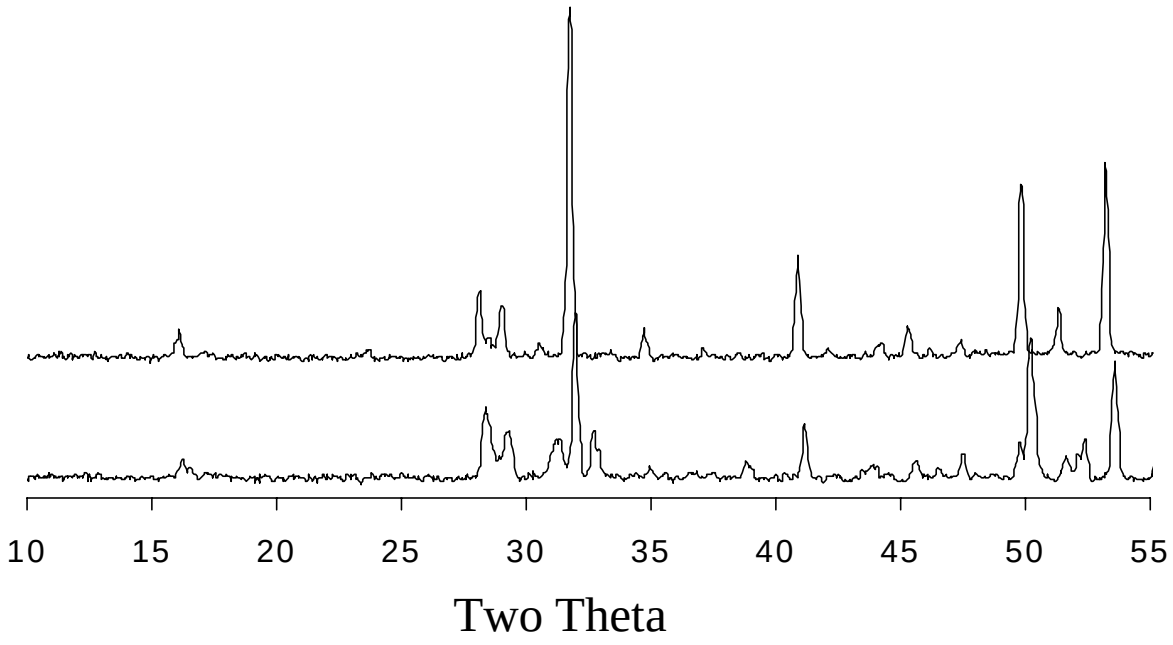

Figure 3.7. Neutron diffraction data for Cu_2ZrCl_6 at (a) 25°C and (b) –173°C.

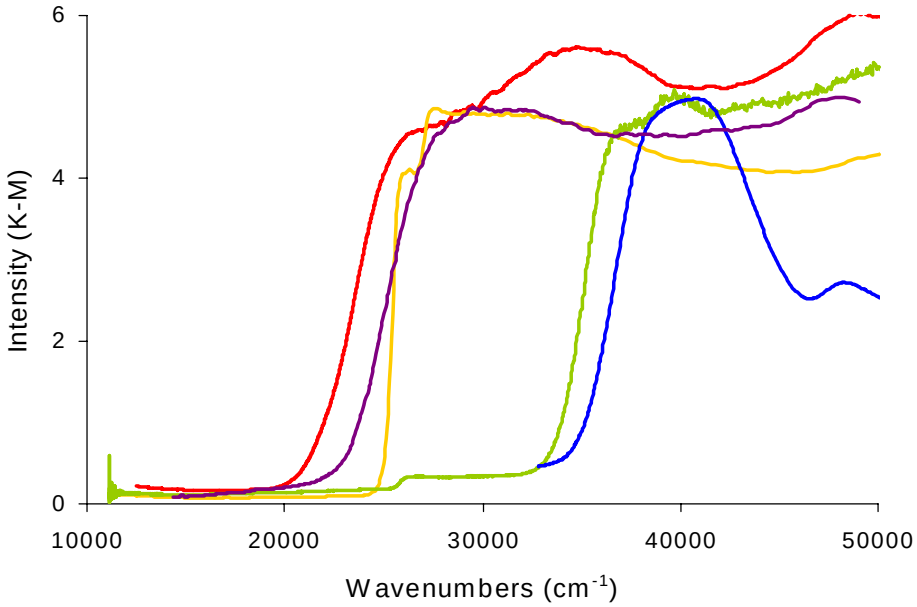

Figure 3.8. Diffuse reflectance data for Cu_2ZrCl_6 (—), $[NMe_2H_2]CuZrCl_6$ (—), CuCl (—), $CuGaCl_4$ (—), and $CuGaCl_4$ (—).

Thermochromic Phase Transitions in Cu_2ZrCl_6. At room temperature Cu_2ZrCl_6 is a yellow color. Upon heating to 400°C a sharp transition from yellow to a burnt red is observed before melting at 462°C. After melting Cu_2ZrCl_6 becomes darker still, and eventually turns almost a reddish-black. Cooling a sample of Cu_2ZrCl_6 to -196°C temperatures results in a yellow to colorless transition. These thermochromic transitions are completely reversible. It has not yet been possible to obtain spectroscopic data for the low and high temperature phases because of instrumental limitations.

The thermochromic and structural phase transitions described above were quantified by differential scanning calorimetry (DSC) measurements as shown in Figure 3.9. Upon heating Cu_2ZrCl_6, a sharp endotherm at 398°C was observed, which corresponds to the high temperature, thermochromic transition. The sample is then observed to melt at 462°C. Upon cooling to room temperature, two exotherms at 440°C and 372°C are observed due to the recrystallization of the solid followed by the solid-state structural transition back to the room temperature phase. DSC measurements taken from room temperature to –180°C are featureless giving no indication of any thermal events associated with the low temperature thermochromic phase transition.

Magnetic Susceptibility. The Van Vleck susceptibility, χ_{VV}, versus temperature is plotted in Figure 3.10 at fields of 0.05 T, 0.5 T, 1.0 T, and 5.0 T, and a plot of χT versus T is shown in Figure 3.11. χ_{VV} is calculated by subtracting the susceptibility of the sample holder and the diamagnetic core (19×10^{-5} emu/mol) of the constituent elements from the molar susceptibility measured by the SQUID. The magnetization versus field at 298 K and 5.0 K is shown in Figure 3.12. Although Cu_2ZrCl_6 has no

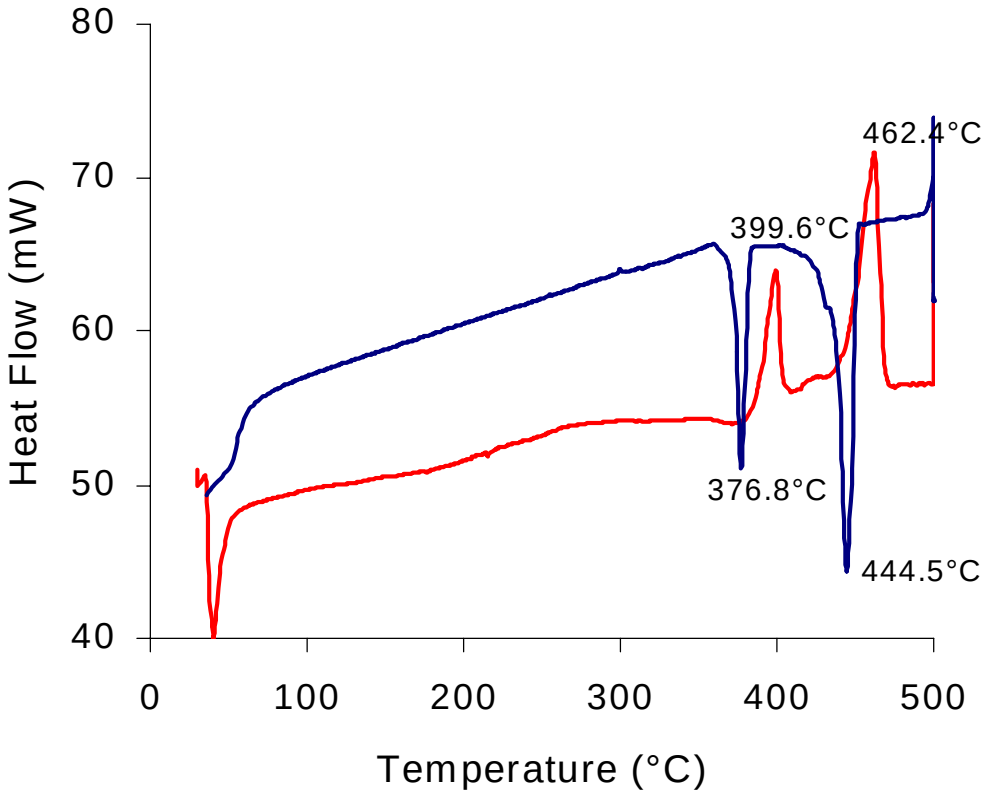

Figure 3.9. DSC obtained upon heating Cu_2ZrCl_6 from 25°C to 500°C (—) and cooling to room temperature(—).

unpaired spins, a weak paramagnetic susceptibility was measured for Cu_2ZrCl_6 at room temperature and applied fields from 0.005 T to 1.0 T. Because of the small susceptibility, careful attention was paid to the sample holder subtraction by measuring the susceptibility of the delrin sample holder with and without sample at all fields. The magnetic susceptibility of Cu_2ZrCl_6 was also measured in a fused silica container, and found to be independent of the sample holder used. This result confirmed that the observed paramagnetism is not a function of the sample holder. A gradual increase in the susceptibility is observed upon lowering the temperature as seen in Figure 3.10. A pronounced inflection in the susceptibility is observed at 120 K, the low temperature phase transition, in the 0.05 T and 0.5 T data. This inflection at the phase transition is reversible as seen upon warming the sample from 5 K to 350 K. At applied fields greater than 1.0 T the magnitude of the response across the phase transition is significantly reduced. Furthermore, as seen in Figure 3.11 χT goes to zero at low temperature consistent with a singlet ground state. At higher temperature χT can be extrapolated toward a field dependent maximum of approximately 0.065 $emu \cdot K \cdot mol^{-1}$ at room temperature and 0.5 T. The field dependence of the magnetization is most clearly seen in Figure 3.12. The magnetization, not corrected for the core diamagnetism, is observed to increase from zero up to a maximum at 0.1 T, then decreases approximately linearly resulting in an observed diamagnetic response at high, applied fields. The maximum is observed at a slightly higher applied field for the low temperature phase at 0.2 T as shown in the inset in Figure 3.12. Similarly a shallower slope to the higher field response is observed.

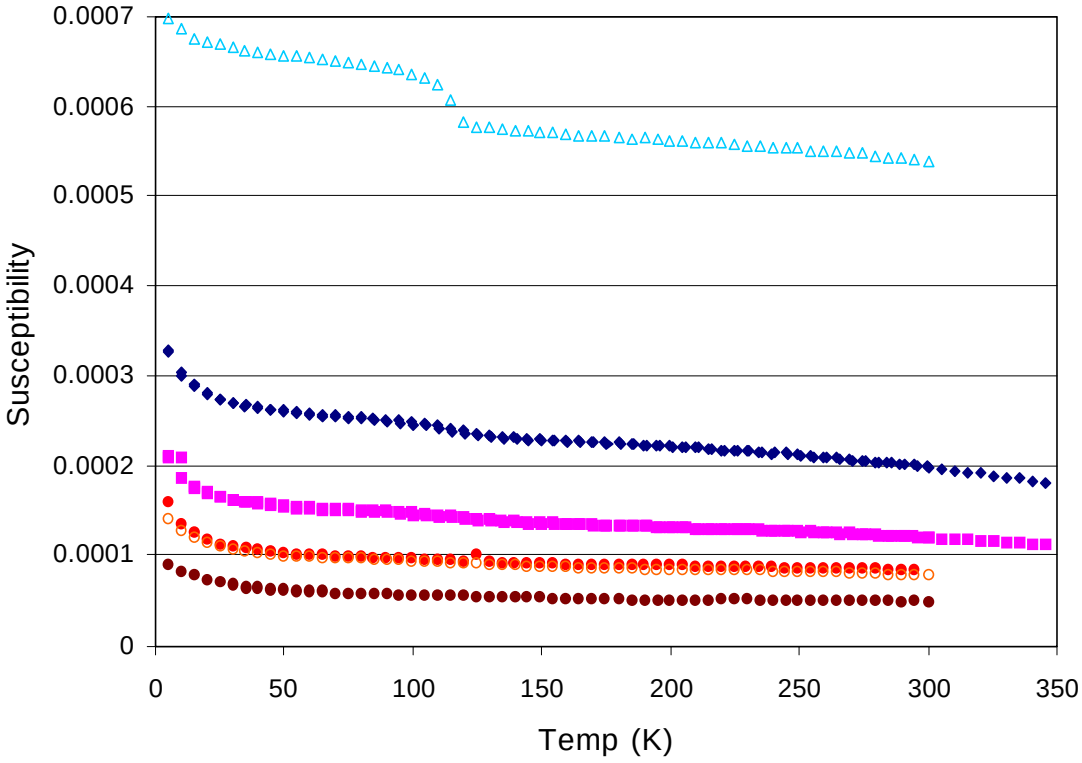

Figure 3.10. χ vs. T (K) at 0.05 T (ρ), 0.5 T (and), 1.0 T (and), 2.0 T (and),and 5.0 T ( ) for Cu_2ZrCl_6. Open and filled shapes correspond to samples run in a fused silica or delrin sample holder, respectively.

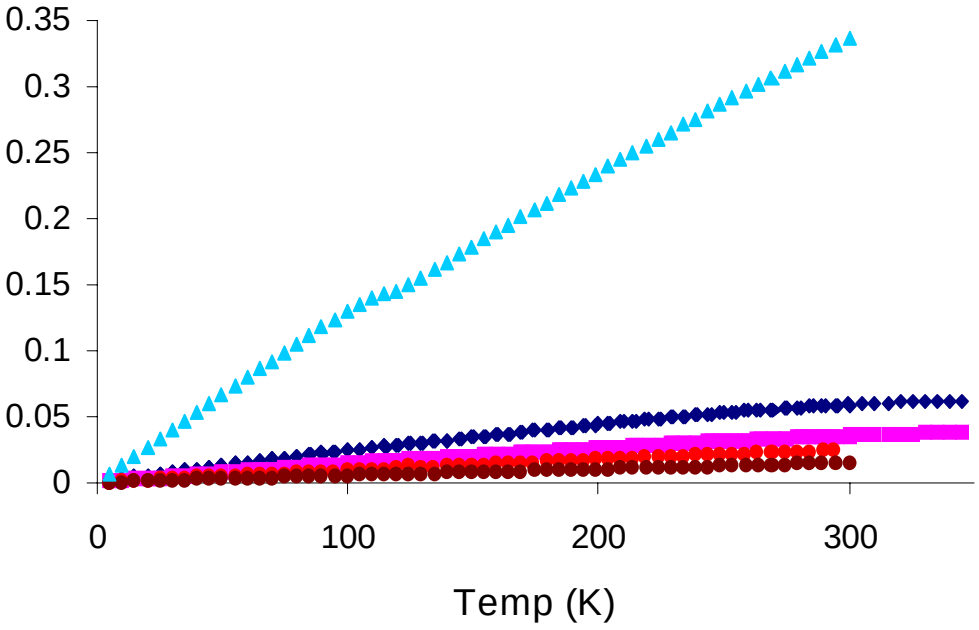

Figure 3.11. χT vs. T (K) at 0.05 T (π), 0.5 T (▬), 1.0 T (▭), 2.0 T(✶), and 5.0 T (✶) for Cu_2ZrCl_6.

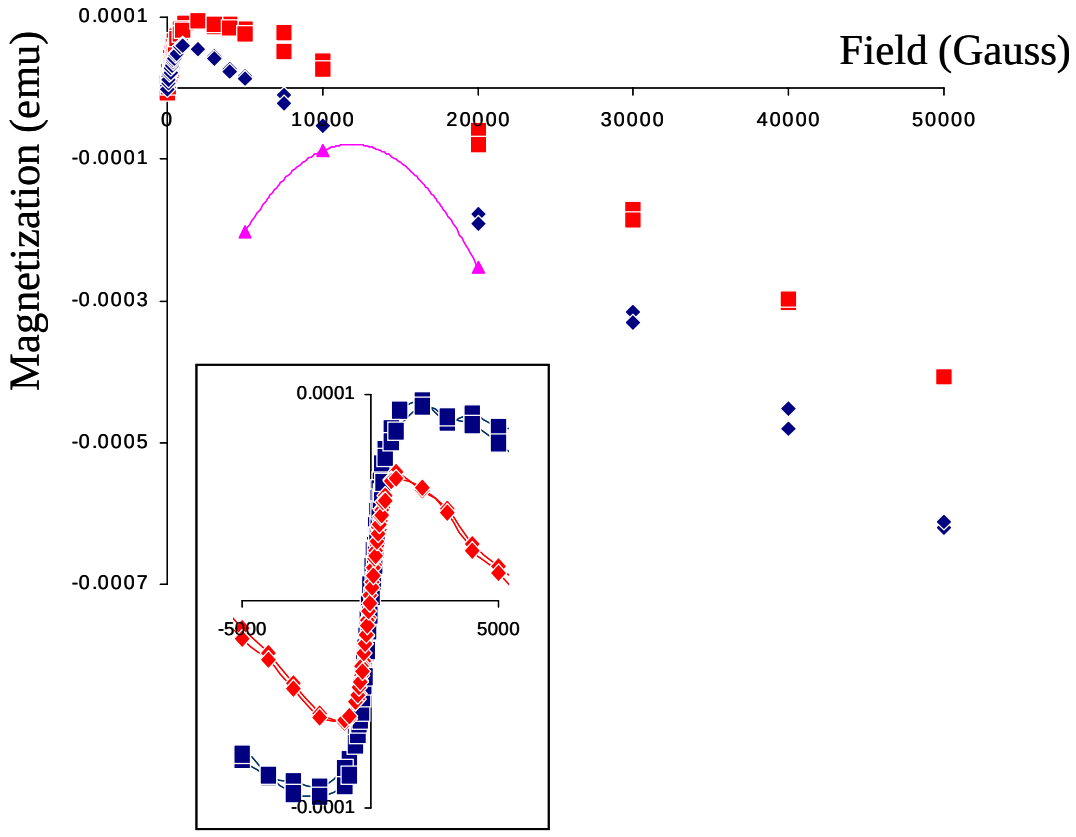

Figure 3.12. Magnetization (M) vs. field (H) for Cu_2ZrCl_6 at 300 K (○) and at 5.0 K (□). Three data points have also been plotted for $[NMe_2H_2]CuZrCl_6$ (π).

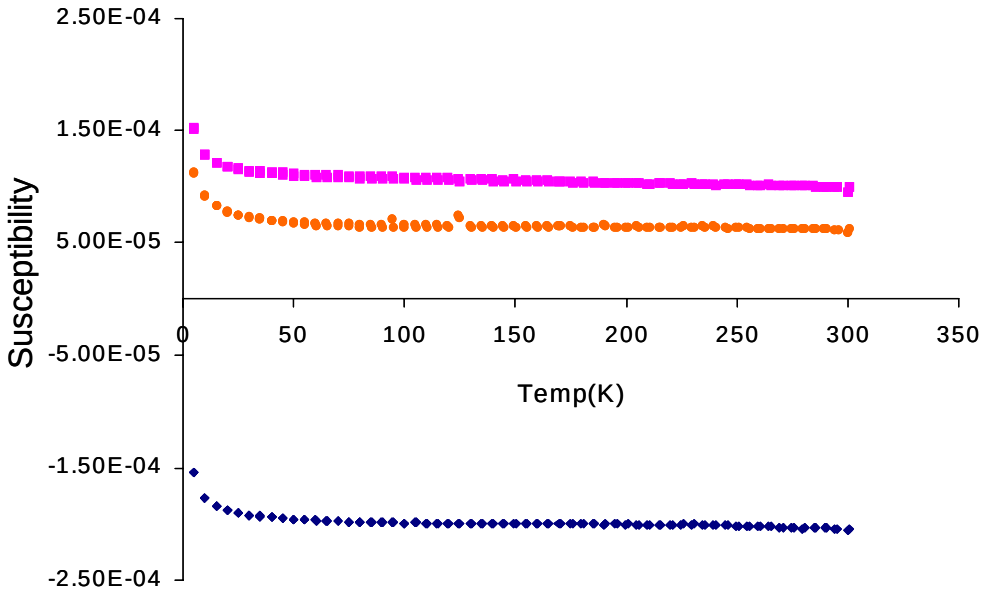

Figure 3.13. χ vs. T (K) at 0.5 T (), 1.0 T (), 2.0 T () in a delrin sample holder for $[NMe_2H_2]CuZrCl_6$.

To further investigate this unusual magnetic response, which may be related to the lower energy charge transfer from d^{10}-Cu(I) to d^0-Zr(IV), the magnetic susceptibility of $[NMe_2H_2]CuZrCl_6$ was measured at 0.5 T, 1.0 T, and 2.0 T as shown in Figure 3.13. This material was prepared from the same starting materials as Cu_2ZrCl_6. The magnetic susceptibility of $[NMe_2H_2]CuZrCl_6$ does not show the same pronounced inflection at 120 K, which confirms that this response in Cu_2ZrCl_6 was due to the low temperature structural phase transition. Furthermore, a diamagnetic response is still observed at an applied field of 0.5 T. A maximum in the paramagnetic response is again observed for $[NMe_2H_2]CuZrCl_6$, however, it occurs at an applied field between 0.5 T and 1.0 T. Further experiments to clarify this M vs. H response are in progress. Nevertheless, three data points for the room temperature magnetization have been added to Figure 3.12.

3.4. Discussion

The solid-state reaction of CuCl and $ZrCl_4$ yields Cu_2ZrCl_6, which is a condensed, three-dimensional solid. The structure of Cu_2ZrCl_6 at room temperature is complicated by an apparent disordering of two copper atoms about three crystallographically different sites labeled Cu(1), Cu(2), and Cu(3) in the unit cell. Refinement of data collected from a twinned crystal could potentially lead to the observed disorder in the copper positions. However, Weissenburg and axial photographs did not show the presence of any spurious reflections, which eliminated the possibility of a non-perfect twinned crystal. To further rule out the possibility of a twinned crystal, X-ray powder patterns were calculated for the solution obtained from the structural refinement, Figure 3.4d, as well as for the structures obtained by occupying only one of the three different copper positions, Figure

3.4a-c. Because powder diffraction data is collected on finely-ground, bulk samples of material, any crystallographic ambiguities that may have been observed from collecting data on a twinned crystal would be eliminated by this data. As seen in Figure 3.4, the experimentally observed powder pattern, Figure 3.4e, matches only the powder pattern calculated using the structural model obtained from the refinement of the single crystal data with the disordered copper atoms, Figure 3.4d. In Figures 3.4a-c, where only one copper site is occupied, the (100) reflection is observed. Furthermore, a Rietveld analysis of the room temperature neutron powder diffraction data shown in Figure 3.5 is also consistent with a structural model for Cu_2ZrCl_6 in which the copper atoms are disordered about three crystallographically different sites in the unit cell. These data indicate that filling only one of the three copper sites does not correctly describe the structure of Cu_2ZrCl_6, but rather the disorder of the copper sites result in a psuedo-symmetry that causes the (100) extinction.

The structure of Cu_2ZrCl_6 is constructed from zirconium octahedra and copper chloride tetrahedra, which are organized into larger structural building blocks. Occupying Cu(1) or Cu(3) results in Cu_3ZrCl_9 adamantane-type building blocks, which are then organized into chains pointed in opposite directions along **c** as seen in Figures 3.1a and 3.1c, respectively. Chloride ligands terminally coordinated to the adamantine-like building blocks of one of the chains form bridges to the zirconium octahedra of a neighboring chain. Such adamantane-like building blocks are regularly seen in metal-sulfide systems. Adamantane-type building blocks, such as $(Ge_4S_{10})^{4-}$, which are then assembled under solvothermal conditions in the preparation of microporous materials.[28-32] Isolated adamantane-like, metal-halide molecular anions, $Cu_4X_6^{-2}$ (X = Br and I), have

also been known for some time;[33-36] however, these adamantane-like units exhibit no terminal ligation and are well separated by large phosphonium and alkyl ammonium counter cations. Occupancy of the Cu(2) sites can be envisioned as the interpenetration of two such adamantine-type chains running in opposite directions. Alternatively, this can be envisioned as chains of Zr_2Cu_6 bicapped trigonal anti-prisms. Two rings of cuprous chloride tetrahedra form the trigonal anti-prism, which is capped on wither three fold face by $Zr(2)Cl_6$ octahedra. Exo-chlorides, Cl(3), bound to Cu(2) form bridges to neighboring Zr(1) octahedra, resulting in a three dimensional network. In this network model the Zr(1)-Cl(1) bonds are terminally ligated and do not participate in the extended network.

The organization of the chains in the crystal lattice of Cu_2ZrCl_6 is reminiscent of the structure of zirconium trichloride, which consists of faced-shared octahedral chains, which are oriented in a hexagonal array shown in Figure 3.14. As seen in Figure 3.15, the face-sharing octahedral chain of $ZrCl_3$ has a 6_3-axis of symmetry. Removing the central octahedral site (Figure 3.15b) or the octahedral sites at the unit cell boundaries (Figure 3.15c) breaks the 6_3-screw axis leaving the zirconium and chloride sublattices with a vacant octahedral interstice that emphasizes the $\bar{3}$ and 3-fold symmetry, respectively. By replacing every other zirconium cation in these $ZrCl_3$-type chains by cuprous cations about the six tetrahedral interstices, which surround the now vacant octahedral interstice, results in the formation of two types of Cu_6ZrCl_6 chains. These are the structural organizations shown in Figure 3.2. An expanded unit cell is required to uniquely describe this "Zr → Cu_6" substitution, with one type of chain residing on the $\bar{3}$-

axis of the unit cell edges and two chains running along the 3-fold axes in the interior of the unit cell as shown in Figure 3.16.

Placing the cuprous cations in the six sites surrounding the $\bar{3}$-site, Cu(2), results in the formation of the bicapped octahedral chains along with Zr(2) as described in Figures 3.1b and 3.2b. Full occupation of these six identical Cu(2) sites results in the formation of a network with a Cu_2ZrCl_6 stoichiometry. By contrast, placing six cuprous cations in to the three Cu(1) and three Cu(3) sites that surround the vacant octahedral interstices along the 3-fold axes would result in the formation of a network with a Cu_4ZrCl_6 stoichiometry. There is no evidence of a significant copper rich non-stoichiometry based on the high yield synthesis and the refinement of copper atom occupancy.[37] However, occupation of only one set of the tetrahedral sites, Cu(1) or Cu(3), would result in the adamantane-type chains as described in Figure 3.1a and 3.1c, respectively. In addition, the face sharing octahedral chains of $ZrCl_3$ are isolated by Van der Walls Cl-Cl contacts, placement of the copper cations in the tetrahedral interstices result in formation of a three-dimensional network in Cu_2ZrCl_6. This structural contrast is highlighted in the views of Cu_2ZrCl_6 and $ZrCl_3$ looking down **c** as shown in Figure 3.16. Furthermore, while occupancy of the tetrahedral sites has expanded the unit cell along the **a**-direction, the **c** lattice constant is equivalent between both materials, **a** = 6.382 Å and **c** = 6.135 Å for $ZrCl_3$,[38] **a** = 10.9892(4)10.382 Å and **c** = 6.1517(2) Å for Cu_2ZrCl_6.

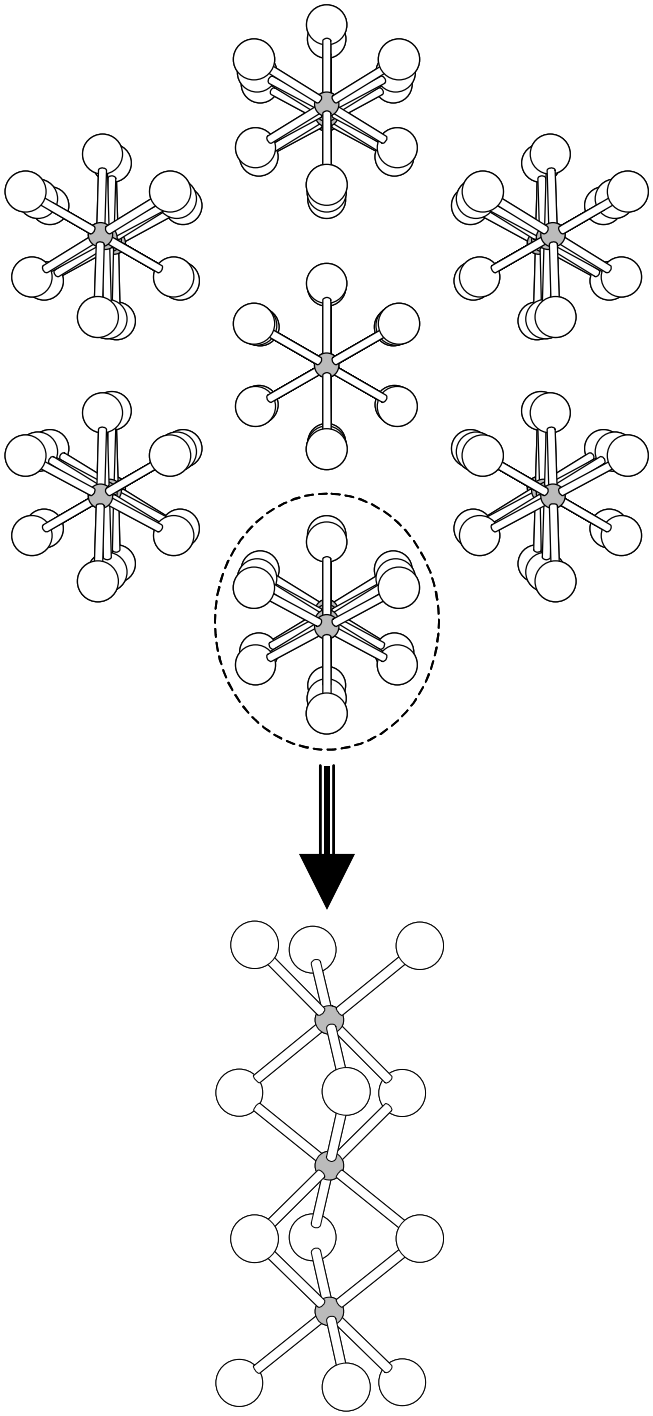

Figure 3.14. Ball and stick drawing of the three dimensional lattice in $ZrCl_3$ constructed from face shared octahedral chains.

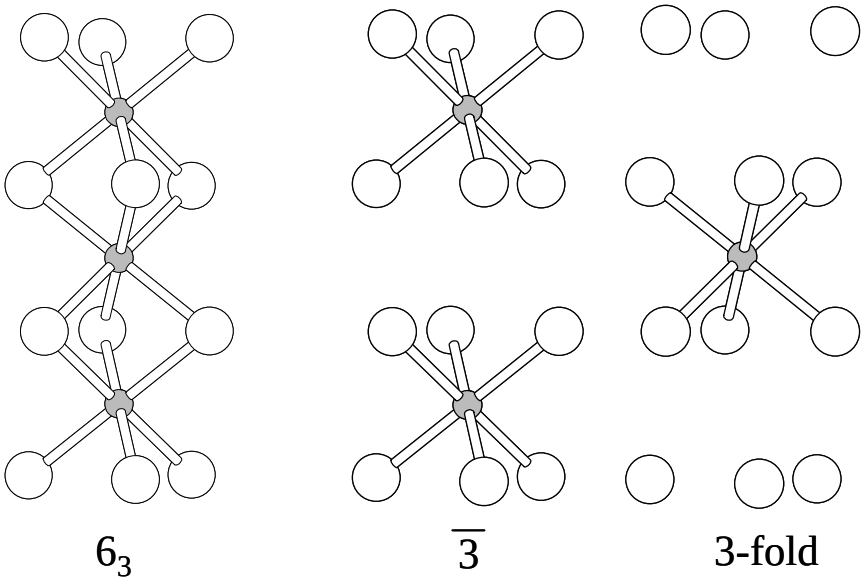

Figure 3.15. (a) A ball and stick drawing of a face shared octahedral chain in $ZrCl_3$ highlighting the 6_3-axis running along the chain. (b) and (c) indicated the resulting $\bar{3}$-fold and 3-axes that are obtained by selectively removing half of the zirconium atoms, respectively.

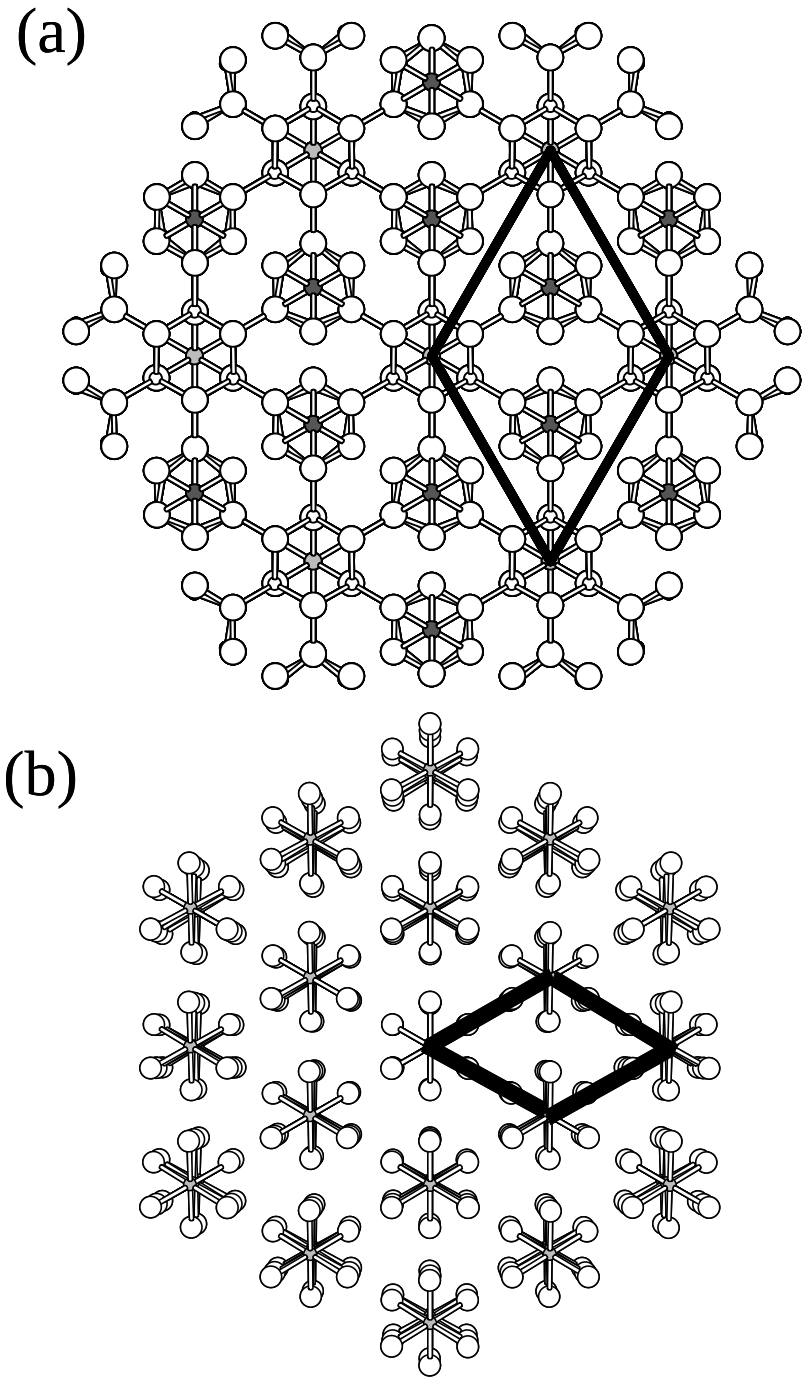

Figure 3.16. Ball and stick drawings viewed down **c** including the unit cell for (a) Cu_2ZrCl_6 and (b) $ZrCl_3$.

Origin of the Room Temperature Color. The pale-yellow color, observed for Cu_2ZrCl_6 at room temperature (and the burnt-red color at high temperature) would not normally be expected for the closed shell electronic configurations of d^{10} and d^0 transition metals with chloride ligands. Rather, color is generally associated with copper containing materials where copper is in its +2 oxidation state suggesting the possibility of a Cu^{2+} impurity. Solid state EPR measurements found Cu_2ZrCl_6 to be EPR silent suggesting any impurity level to be below 1%. The weak room temperature paramagnetic susceptibility, 2.4×10^{-4} emu·mol^{-1}, could be indicative of a Cu^{2+} impurity; however, temperature and field dependence of the susceptibility (Figure 3.10 discussed below) is inconsistent with a paramagnetic Cu^{2+} impurity. The diffuse reflectance spectrum of Cu_2ZrCl_6 also shows no evidence of the $CuCl_2$ absorption feature in the blue-green region, ~19,000 cm^{-1}, of the visible spectrum. Furthermore, synthesis of $[NMe_2H_2]CuZrCl_6$, from the identical starting materials used for the synthesis of Cu_2ZrCl_6, yields a colorless material. Thus, a Cu^{2+} impurity was ruled out as the origin of the coloration.

In order to realize the origin of the room temperature color of Cu_2ZrCl_6, diffuse reflectance data were collected on Cu_2ZrCl_6 as shown in Figure 3.8. Cu_2ZrCl_6 was found to be a semiconductor with a band gap of ca. 23,400 cm^{-1} (2.9 eV). For comparison purposes, the spectra of CuCl and $CuMCl_4$ (M = Al and Ga) are included in Figure 3.8. $ZrCl_4$ has a band gap in the vacuum ultraviolet, which could not be measured with the instrumentation employed for this DRS study. CuCl has a band gap that is relatively close in energy to that of Cu_2ZrCl_6, 3.2 eV. However, both $CuAlCl_4$ and $CuGaCl_4$ exhibit much larger band gaps of 4.0 eV and 4.2 eV, respectively. The lowest energy transition in CuCl is due to an electron transfer originating from a high-lying, filled copper d-band

to a low-lying, empty sp-hybrid band on copper.[39,40] Substitution of strong Lewis acids, like Al^{3+} and Ga^{3+}, into the copper chloride lattice has been shown to substantially shift this transition to higher energy.[5] This likely results from the strong interaction of the Lewis acid with the chloride ligands, which decreases the Cu-Cl interaction and stabilizes the copper d-band. Yet, like CuCl, the lowest energy transition in both $CuAlCl_4$ and $CuGaCl_4$ was identified as a copper-centered $3d^{10}$ to $3d^94s^1$ transition. Chloride-to-copper charge transfer was eliminated as the lowest energy transition in these materials by demonstrating that substitution of bromides for chlorides had no effect on the position of the band edge. Although, both Al^{3+} and Ga^{3+} have unfilled p-orbitals, they are much higher in energy than the LUMO of CuCl, which precludes them from participating in the lowest energy electronic transitions. By contrast, addition of the Lewis acid Zr^{4+} into CuCl provides a set of unfilled d-orbitals that are at a significantly lower energy than the unfilled p-orbitals of Al^{3+} and Ga^{3+}, and fall below the LUMO in CuCl. Therefore, the substitution of Zr^{4+} into the cuprous chloride lattice should insert the unfilled zirconium d-band between the high-lying filled and the low-lying unfilled copper energy bands. As a result, these empty orbitals of intermediate energy decrease the band gap, and change the nature of the lowest energy transition from one that is copper-centered to one that is a transition from a filled CuCl band to an unfilled zirconium band. Halide-to-metal transitions have been proposed for related copper and silver mercury iodide systems. And, there is significant halide character mixed into the copper d-orbitals. But the Cu-Cl σ^* HOMO is best considered a metal based orbitals. Were chloride to zirconium charge transfer dominant, then $ZrCl_4$ and the related A_2ZrCl_6 salts, where A = Cs or Rb, would be expected to exhibit electronic transitions in the visible region. Yet, they are all

colorless materials with absorption bands in the deep UV. The lowest energy excitation in these A_2ZrCl_6 materials must be from filled chloride p-orbitals to unfilled zirconium d-orbitals in all cases, as the empty A^+ orbitals are significantly higher in energy than the zirconium d-orbitals. Because copper has high lying filled d-orbitals, which are not present in either Cs^+ or Rb^+, it is reasonable to suggest that lowest energy transition in Cu_2ZrCl_6 is from these filled copper d-orbitals to the empty zirconium d-orbitals. Thus, this transition is likely the origin of the yellow color at room temperature and burnt-red color at high temperature.

To support this conclusion, the Density of States (DOS) were calculated by the extended Hückel method for the three different structural models shown in Figures 3.3a-c, where only one of the three possible copper sites is fully occupied. These calculations resulted in essentially the same orbital picture regardless of which copper site is occupied as seen in Figure 3.17-3.19. The valence band (ca –11 to –10 eV) is calculated to be a mixture of filled copper and chloride orbitals, while the conduction band (ca. –9 eV) consists mainly of the empty, zirconium d-orbitals, with a small amount of ligand p, as well as copper s and p-character. The empty Zr d-orbitals fall below the empty copper sp-hybrid orbitals (ca. –4 eV). These DOS calculations thus support the description of the lowest energy transition, which gives rise to the room temperature color in Cu_2ZrCl_6, as a metal-to-metal charge transfer from high-lying, filled copper d-orbitals to an unfilled zirconium d-orbitals.

Origin of the Thermochromicity in Cu_2ZrCl_6. Cu_2ZrCl_6 undergoes two reversible thermochromic transitions at –150°C and 398°C, respectively, resulting in a series of transitions from a colorless to a yellow to a burnt red colored material. Two

types of thermochromism are known, which are described as continuous or discontinuous. The distinction between these is the temperature range over which the transition occurs. Continuous thermochromic changes are observed to exhibit a temperature dependence of the spectral line width of an electronic transition, and vary gradually as a function of temperature. Discontinuous thermochromic changes are characterized by a sharp change in color over a small temperature range, and generally result from a first- or second-order structural phase transition. A sharp endotherm is seen in the DSC of Cu_2ZrCl_6 at 398°C before the sample melts at 430°C as shown in Figure 3.9, which occurs at the same temperature as the color change from yellow to red. This data indicates that Cu_2ZrCl_6 undergoes a discontinuous thermochromic phase transition at high temperature, likely the result of a structural phase change. Efforts to characterize the structural phase change at high temperature were hampered by the material subliming out of the X-ray beam in HT diffraction experiments. A structural phase transition was observed to occur at low temperature as seen by X-ray and neutron powder diffraction shown in Figures 3.6 and 3.7, respectively. However, this low temperature phase transition was not observed in low temperature DSC measurements (not shown). Nevertheless, the diffraction and magnetic data (discussed below) give clear indication of structural changes taking place at the temperature thermochromic transition consistent with the observed discontinuous thermochromic transition.

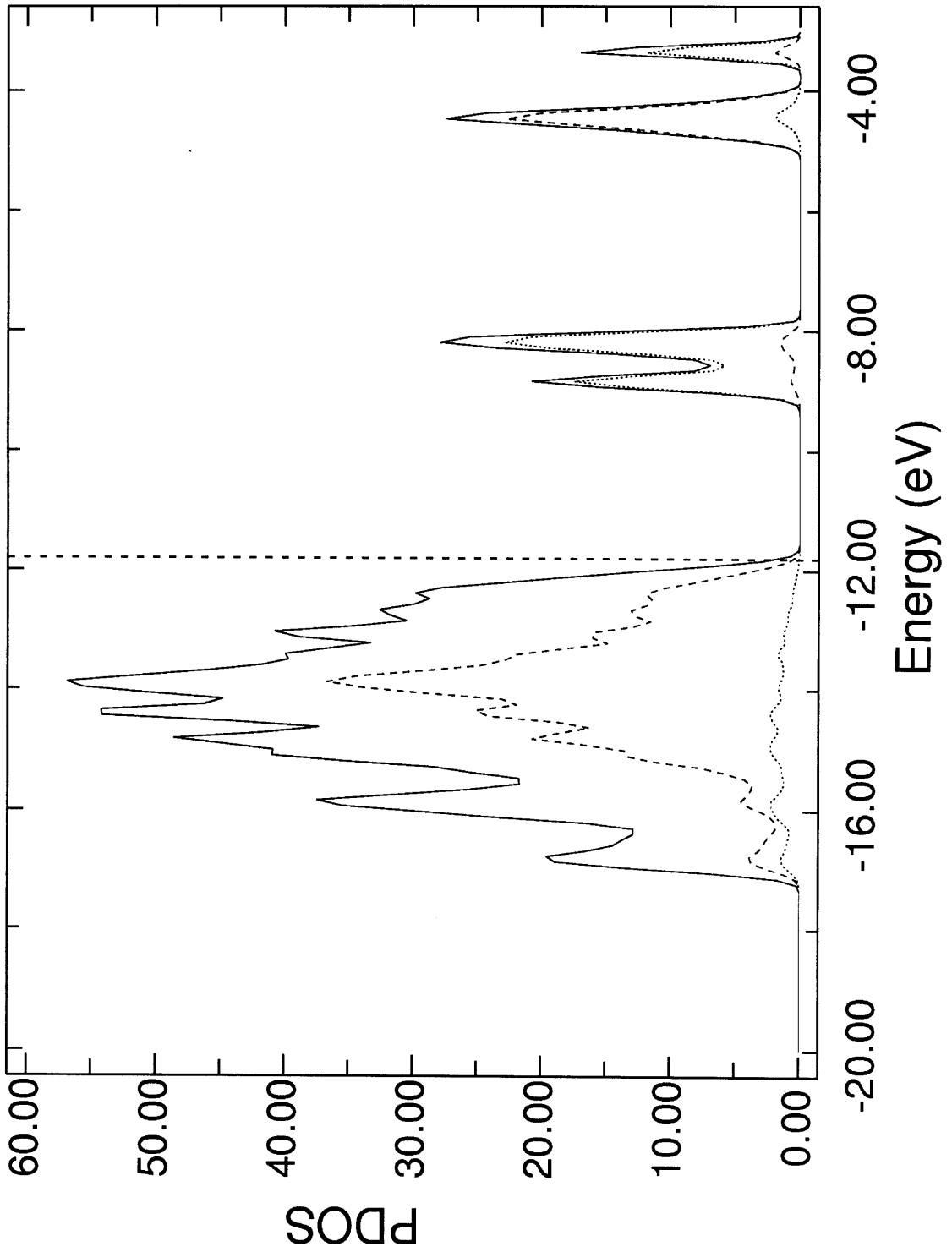

Figure 3.17. Total and Projected Density of States (DOS) calculated for $Cu(1)_2ZrCl_6$. The horizontal line is the Fermi Level. The total DOS is given by a solid line, the copper orbital contribution to each state is given by the dashed (----) line, and the zirconium orbital contribution is given as the dotted line (····). (Convention used throughout.)

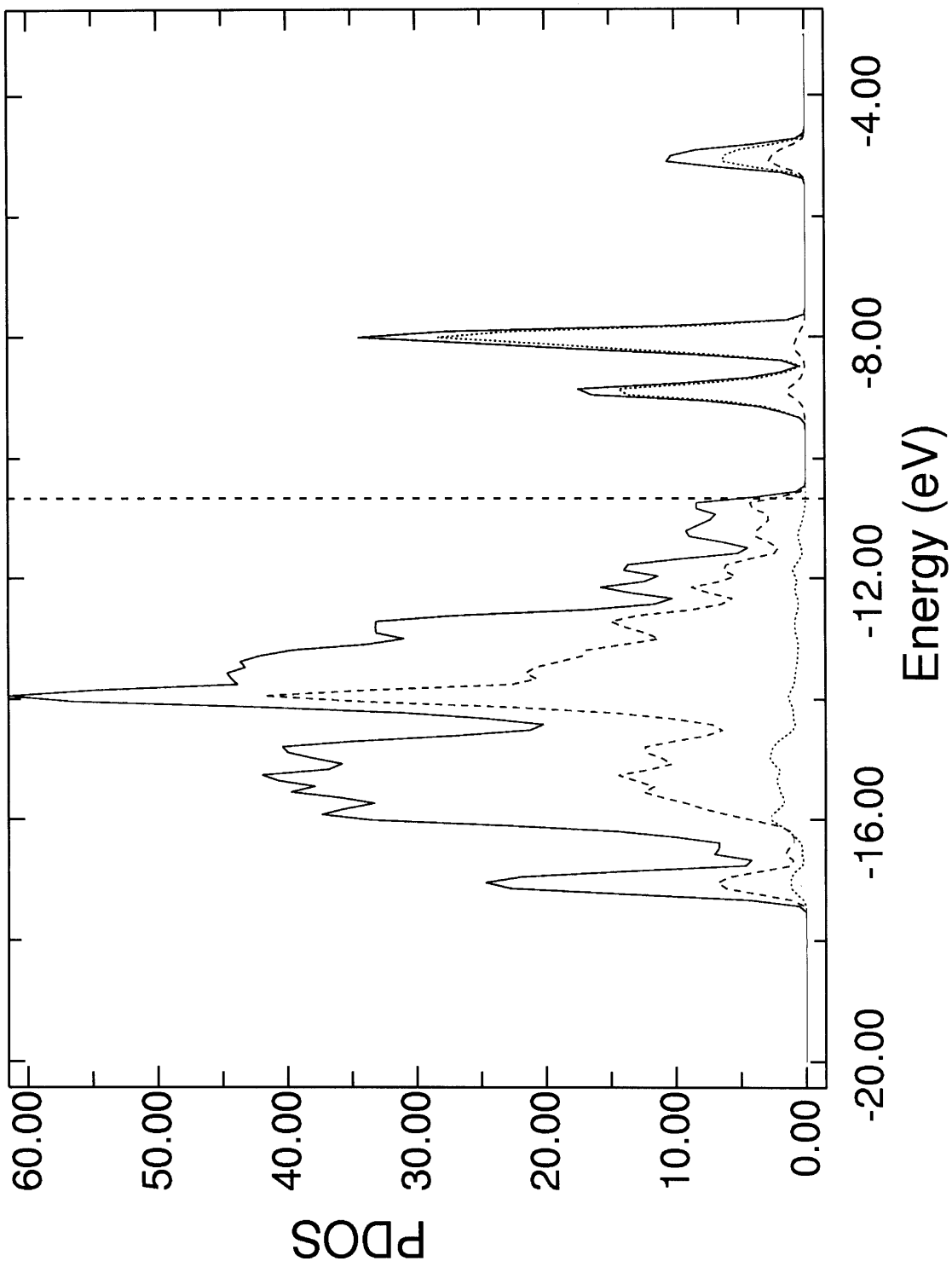

Figure 3.18. Total and Projected Density of States (DOS) calculated for $Cu(2)_2ZrCl_6$.

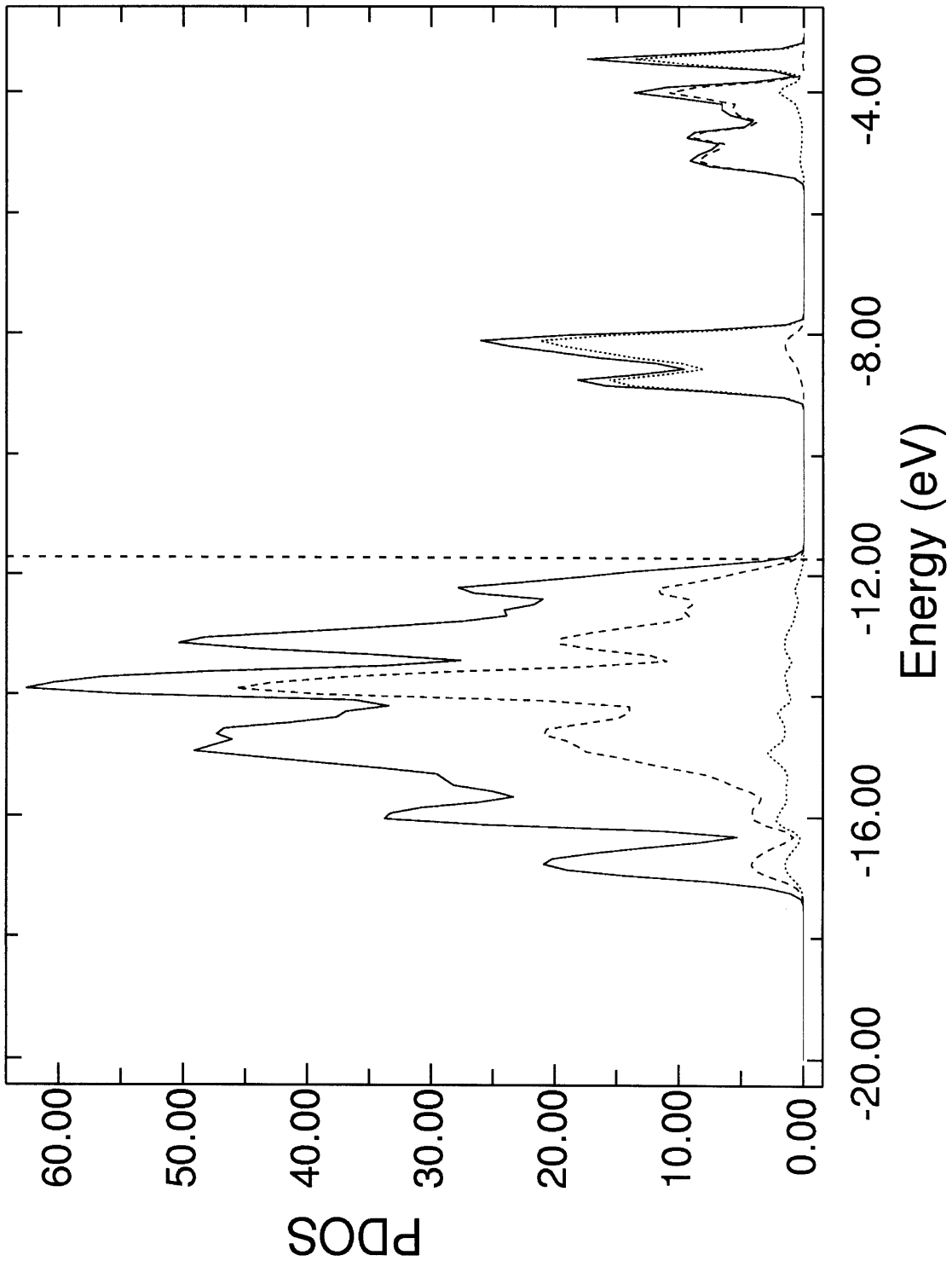

Figure 3.19. Total and Projected Density of States (DOS) calculated for $Cu(3)_2ZrCl_6$.

Although neither the LT nor HT structures has been determined at this time, the structures of two related materials constructed from copper(I) tetrahedra and zirconium(IV) octahedra, $[NMe_2H_2]CuZrCl_6$[8] and $(C_6H_6CuCl_3)_2Zr$,[41] have been solved at low and room temperature. In both instances, these copper-zirconium halide phases were observed to undergo a structural phase transition at low temperature (-60°C and –120°C (temperature of data collection), respectively). At room temperature the copper atoms sit in a trigonal pyramidal site with three basal Cu-Cl contacts of 2.3 Å (or two basal and one benzene ligand in $(C_6H_6CuCl_3)_2Zr$) and one long, apical Cu-Cl contact ca. 2.5 Å. Below the phase transition temperature, the copper atoms reside in a more nearly ideal tetrahedral environment with four Cu-Cl contacts of about 2.3 Å. These distortions are related to the second-order Jahn-Teller mixing of the filled Cu d-orbitals and the low lying Cu s-orbitals. The temperature dependence of this distortion demonstrates a competition between the lattice energy and this second-order orbital mixing, where greater distortion is possible in the less rigid lattice at higher temperatures. Relatively little variation in the Zr-Cl bond distances were observed. This distortion/second-order orbital mixing will undoubtedly result in a variation in the band gap, and, thus, is likely responsible for the observed thermochromism in Cu_2ZrCl_6.

A schematic, orbital diagram of the distortion from a tetrahedral to trigonal pyramidal geometry is shown in Figure 3.20. Copper(I) readily distorts from the tetrahedral geometry to the trigonal pyramidal geometry because of the second order mixing.[2] Two of the t_2 orbitals are lowered due to a decrease in the Cu-Cl antibonding interaction, while the other is raised in energy. This same distortion results in a destabilization of the Cu s-orbitals, while the t_1 Cu p-orbitals exhibit the inverse of the

splitting of the filled d-based t_2 orbitals. Because the LUMO orbitals on zirconium are the t_{2g}-type non-bonding orbitals, these energy levels are essentially immune to any structural distortion. Thus, the band gap decreases in Cu_2ZrCl_6 as copper distorts towards a trigonal pyramidal geometry. At room temperature, there is a mixture of copper coordination geometries with Cu(2) in an almost ideal tetrahedral site, Cu(3) in the most distorted trigonal pyramidal site, while Cu(1) exhibits an intermediate distortion (See Table 4). In the low temperature phase, the more rigid lattice disfavors the distortion due to the second order mixing. As a result, the increased band gap leads to the loss of absorption in the visible region to yield a colorless material. In the high temperature phase the copper atoms likely distort further away from a tetrahedral coordination and towards a trigonal pyramidal environment, which decreases the band gap resulting in the observed color change from yellow to red.

It is useful to compare the thermochromic properties of Cu_2ZrCl_6 two similar inorganic, materials, Ag_2HgI_4 and Cu_2HgI_4. Both of these iodide-based materials also undergo discontinuous, thermochromic phase transitions at high temperatures. Ag_2HgI_4 is yellow at room temperature and orange at 50°C. Cu_2HgI_4, which is a yellow-orange color at room temperature, becomes a dark-maroon at 67°C. Both materials undergo a structural phase transition at the thermochromic transition temperature. At room temperature, the silver(I) or copper(I) cations are ordered in the mercury iodide lattice, but only partially occupy their positions within the unit cell. Upon heating, the +1 cations randomly disorder about all the possible sites in their respective lattice.[42-46] Because all of the A_2HgI_4 (where A = K, Rb, Cs, Cu, Ag) solids are colored at room

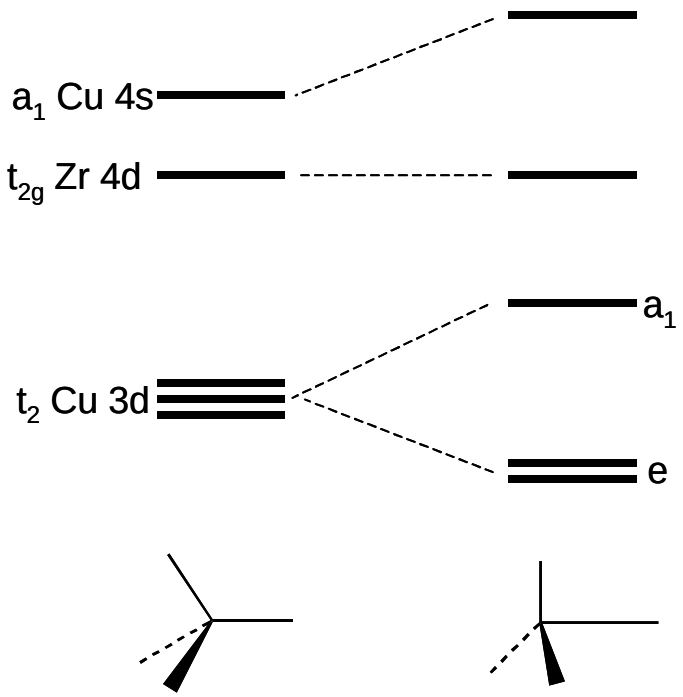

Figure 3.20. Schematic orbital energy diagram of a tetrahedral to a trigonal pyramidal distortion.

temperature, the lowest energy transition was determined to occur between the filled iodide p-orbitals and the unfilled mercury p-orbitals regardless of the cation present.[47] Extended Hückel calculations on the copper and silver salt indicate that as the copper or silver cations randomly distribute about all possible positions, they interact with all of the iodide ligands to a greater extent. This increased interaction was shown to broaden the p-band resulting in a lower LMCT transition, and hence, the observed color change.

Although the thermochromic properties for Cu_2HgI_4 and Ag_2HgI_4 are similar to that observed for Cu_2ZrCl_6, the explanation of the thermochromicity in Cu_2ZrCl_6 differs due to the different halide present. As the halide changes from iodide to chloride the electronegativity of the ligand increases, which lowers the energy of the ligand p-orbitals. This changes the character of the valence band from almost entirely a ligand dominated band in the copper and silver mercury iodides to one that consists of a mixture of ligand p- and copper d-orbital character. And, as described above, the electronic transitions in Cu_2ZrCl_6 that gives rise to the room temperature color occur between the filled copper d-orbitals and empty zirconium d-orbitals. Thus, the thermochromic transition in Cu_2ZrCl_6 is similar to the mercury-iodides in that both systems exhibit phase changes that accompany the color changes. However, they differ in the nature of the lowest energy transition, which is LMCT in the mercury iodides and MMCT in Cu_2ZrCl_6, which results from the increased electronegativity of the chloride ligands compared to the iodides.

Magnetic Data. The magnetic response of Cu_2ZrCl_6 is unusual (and the subject of our continuing investigation) given the closed shell electronic configuration of the d^{10} and d^0 metal centers (Figures χ vs T, χT vs T and M vs. H). Nevertheless, correspondence of the thermochromic and structural phase transitions with the observed

magnetic response indicates that the observed response is not simply an artifact. Furthermore, the second-order Jahn-Teller distortion brought about by the close proximity of the filled copper d-orbitals and empty copper s orbital, as well as, the low lying empty zirconium d-orbitals inserted into the band gap of CuCl in Cu_2ZrCl_6, which are responsible for the Cu→ Zr charge transfer induced thermochromism, led us to suspect that this observed magnetic response is a result of a field induced mixing of a singlet ground state with a low lying triplet excited state.

Small and anomalous magnetic effects are frequently dismissed as being a result of some magnetic impurity. Because Cu(I) can readily be oxidized to Cu(II) extensive efforts were made to verify that impurities can be excluded as an explanation for the magnetic response. The EPR spectrum of Cu_2ZrCl_6 is silent giving a likely upper limit of a Cu(II) impurity to be 1%. The measurement of the field dependent response to the magnetization provides the most sensitive probe for impurity phases. A paramagnetic impurity would be anticipated to give a field independent response; a linear slope in an M vs. H plot (Figure 3.21a) up to the saturation magnetization. A ferromagnetic impurity would be expected to exhibit magnetic saturation at low field, as seen as a flat line in the M vs. H plot (Figure 3.21b). By contrast, the field dependence of the magnetic response of Cu_2ZrCl_6 (Figure 3.12) increases to a maximum at low field and then linearly decreases to yield a diamagnetic response at high fields. Although a conclusive explanation of the field dependence has not yet been determined, no magnetic impurities are known to exhibit this observed response. Furthermore, we have synthesized the material $[[NMe_2H_2]CuZrCl_6$ (described in Chapter 2) from the identical starting materials as were used for the synthesis of Cu_2ZrCl_6, and examined its magnetic response. This

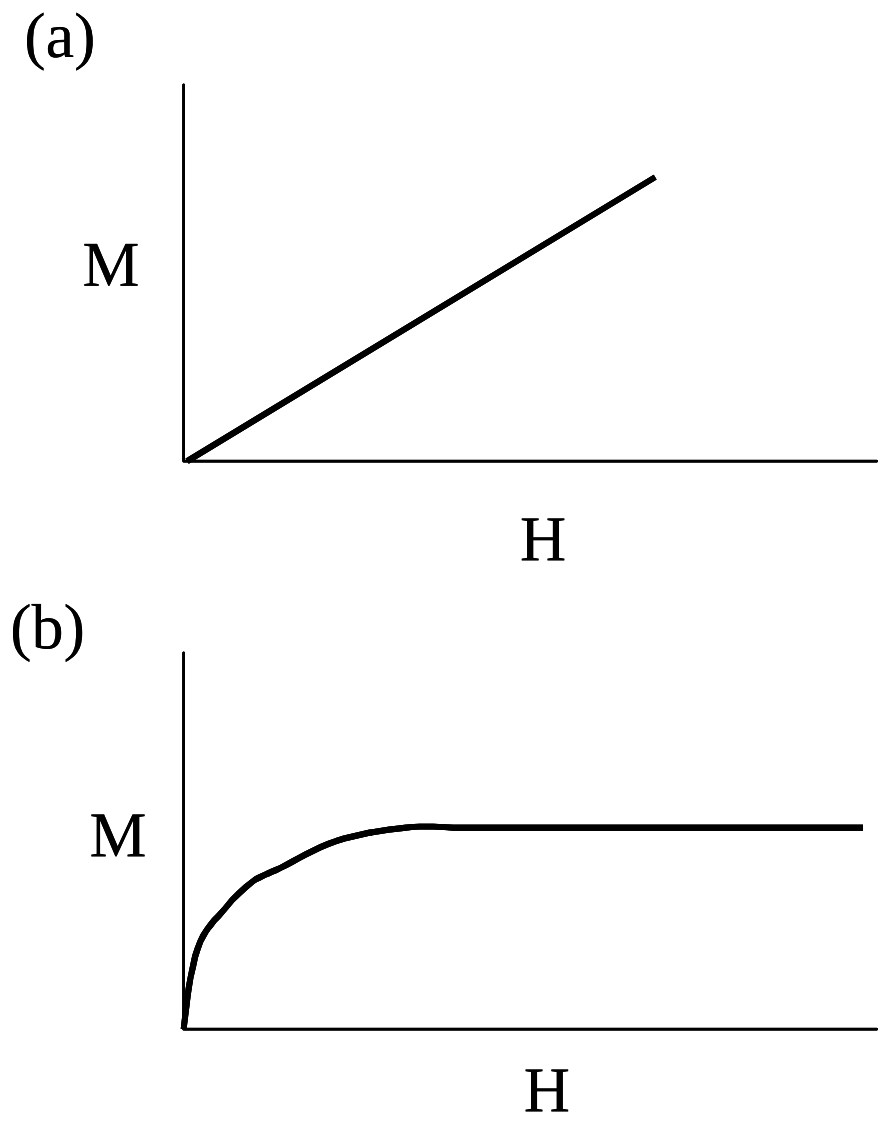

Figure 3.21. Magnetization (M) as a function of field (H) for (a) a paramagnetic and (b) a ferromagnetic material.

material is colorless at room temperature and preliminary magnetic measurements exhibit a diamagnetic response at fields of 0.5 T, 1.0 T and 2.0 T (Figure 3.12 (M vs H). Nevertheless, the diamagnetic response of $[NMe_2H_2]CuZrCl_6$ is less than the magnitude of the diamagnetic core correction, and it exhibits a similar maxima in the magnetization as a function of field, albeit at significantly higher applied fields. These data conclusively argue that the observed paramagnetic response of Cu_2ZrCl_6 is attributable to the electronic structure of this material and is not an impurity.

Materials that would normally be considered diamagnetic based on their closed shell electronic configuration may exhibit paramagnetism when placed in an applied magnetic field if a virtual excited state wave function can mix with the ground state function. Such magnetic behavior was originally proposed by Van Vleck and is generally referred to as Van Vleck or temperature independent (TIP) paramagnetism.[3,48] Van Vleck described this phenomenon quantum mechanically according to equation (**1**) where $\mathbf{m}^0(0;n)$ is the matrix element of the orbital angular momentum operator for an electron that is promoted from the ground state into the *n*th excited state. E(0;n) is the corresponding excitation energy and N_A is Avogadro's number.

$$\chi = \frac{2}{3} N_A \sum_{n \neq 0} \frac{\left|\mathbf{m}^0(0;n)\right|^2}{E(0;n)} \qquad (\mathbf{1})$$

Mixing of wave functions can only occur if there exists a nonzero orbital angular momentum**.** This occurs when there is orbital overlap in the excited state between the donating and accepting species. Van Vleck paramagnetism has been observed, and the orbital picture described by semi-empirical calculations, for a number of $[MO_4]^-$ salts

(where M = Mn, Cr, V, Ti, etc),[49-52] where the virtual excited state consists of both the oxygen p- and the low lying d-orbtials of the transition metal. The molar susceptibility of $[MnO_4]^-$ = 40 × 10^{-6} emu/mol, $[CrO_4]^-$ = 30 × 10^{-6} emu/mol, and $[VO_3]^-$ ≈ 25 × 10^{-6} emu/mol, for example are attributed to Van Vleck paramagnetism.[51-52] Such Van Vleck paramagnetism is normally considered to be temperature independent, which generally holds for isolated molecules. However, Van Vleck notes that in the solid-state conditions are more complicated because the density (and thus the number of atoms per unit volume) is not temperature independent.[3] Thus, minor structural modifications as a function of temperature may significantly influence the magnetic response in the Van Vleck model.

Recently, an indirect Van Vleck paramagnetism was described for In_2ZrBr_6,[53] which is closely related to the magnetic behavior we observe for Cu_2ZrCl_6. Because there is no direct orbital overlap between the In^+ and Zr^{4+} ions, the interaction was described as indirect, occurring through the bridging bromide ligands. Calculation of the DOS for In_2ZrBr_6 demonstrated that there is some In 5s (valence band) contribution to the zirconium d-band (conduction band) as a result of the indium-bromide interaction. Similarly, the projected DOS for the different lattices that would be obtained from independently occupying each of the three unique copper sites in Cu_2ZrCl_6, shown in Figures 3.17-3.19, indicate the presence of some Cu contribution in the lowest-lying, unfilled band, which is largely Zr-d in character. Thus, mixing between the ground and excited state wave functions is possible for Cu_2ZrCl_6, which can give rise to the observed Van Vleck paramagnetism.

The description of the Van Vleck-type paramagnetism in In_2ZrCl_6 was subsequently criticized sharply, and it was suggested that the observed response was simply a result of a paramagnetic impurity. In this critical paper, the authors indicate that the magnetic susceptibility was measured under applied fields of 1.0, 3.0 and 5.0 T, but only the 1.0 T data was presented, and no comment was made as to the field dependence of the measurement. Upon careful examination, the only significant difference between the data originally presented by Dronkowski and that in criticism by Jansen was whether or not a diamagnetic core correction was included in the reported magnetic susceptibility. When the figure presented by Jansen is scanned as a digital image and expanded, the features reported by Dronkowski could be observed. Furthermore, when a diamagnetic core correction is added to the data published by Jansen, then these two reports are in complete agreement. Nevertheless, this highlights the need to consider the effect of the diamagnetic core in the consideration of the measured susceptibility.

In the absence of spin angular momentum, for materials with a closed shell electronic configuration, the measured magnetic susceptibility, χ_m, is a result of the sum of the core diamagnetism, χ_d, and any Van Vleck paramagnetism, χ_{vv}. The field-induced electron circulation of paired electrons generates a field that is opposed to the applied magnetic field resulting in a negative value for the susceptibility. The diamagnetism is field independent, and can generally be determined by the sum of the contributions of the respective elements of a material; standard values have been tabulated as Pascal's constants. Van Vleck paramagnetism, then is observed when the measured susceptibility is significantly more positive than that of the core diamagnetism. Such a subtraction of the diamagnetic core correction of 19×10^{-5} emu/mol from the susceptibility data for

Cu_2ZrCl_6 (Figure 3.11) results in the observation of a significant Van Vleck paramagnetism at all fields measured. By contrast, a similar analysis of the magnetic susceptibility data for $[H_2NMe_2]CuZrCl_6$ shows this material to be diamagnetic below applied fields of about 0.5 T, but paramagnetic above 1.0 T, indicating that significant Van Vleck paramagnetism is observed (Figure 3.13).

Based on the magnetization versus field data, it suggested here that the maximum in the Van Vleck susceptibility seen as a function of field is dependent upon the band gap of a given material. As described above, the maximum magnetization for Cu_2ZrCl_6 increases at low temperature to 0.02 T at 5.0 K from 0.01 T at 300 K. Further, the ability for the virtual excited state to mix with the ground state is proportional to the energy gap between the valence and conduction bands. That is, as the energy gap decreases virtual transitions into the excited state more readily occur. Thus, in order to maximize the magnetization at lower temperature greater applied fields are needed, which is consistent with an increased band gap between 300 and 5 K. Such an explanation of the data is also consistent with the larger fields needed to maximize the Van Vleck susceptibility observed for $[NMe_2H_2]CuZrCl_6$, which has a band gap of 3.1 eV compared to 2.9 eV measured for Cu_2ZrCl_6 (Figure 3.8). Based on this data, it is anticipated that CuCl, with a band gap of 3.2 eV, would exhibit a field dependence similar to $[NMe_2H_2]CuZrCl_6$. However, more data will be required to substantiate these initial findings in order to determine if a field dependence on the magnetization is common for semiconducting materials is a general phenomenon.

3.5. Conclusion

The structure of Cu_2ZrCl_6, which is a three-dimensional framework material constructed from adamantane-like and bicapped trigonal ant-prism building blocks, has been described. Both the single crystal and neutron powder data are consistent with a structure that has two copper atoms distributed about three crystallographically different sites in the unit cell. Cu_2ZrCl_6 also undergoes thermochromic transitions at both –173°C and 398°C, which are accompanied by structural phase changes as observed by DSC or powder X-ray and neutron diffraction. The thermochromicity is related to the ability of copper to undergo a second order Jhan-Teller distortion, which enables it to distort from a tetrahedral to a trigonal pyramidal coordination geometry. As copper distorts to the trigonal pyramidal geometry the band gap decreases giving rise to the observed yellow to red thermochromic transition. At low temperature, the copper atoms settle into idealized tetrahedral geometries, which lead to an increase in the band gap resulting in the yellow to colorless transition. Perhaps more interesting is the magnetic data reported here for Cu_2ZrCl_6, which indicates that it is paramagnetic at low field and diamagnetic at higher fields. The paramagnetic behavior can be understood by an indirect Van Vleck paramagnetism, which occurs through the chloride bridges. Based the materials discussed here, the maximization of the Van Vleck paramagnetism is shown to be related to the size of the band gap, i.e. as the band gap increases greater applied fields are needed to maximize this term. This may be a general trend for wide band gap semiconductors, although more data is necessary to substantiate such a generalization. .

Acknowledgements

I would like to especially thank Paul Ryan for collecting the magnetic susceptibility data, and Paul Boyle for collecting the crystallographic data. I would also like to thank Barbara Reisner, Brian Toby, and Roger Sullivan for collecting and analyzing the neutron powder diffraction.

3.6. References

(1) Martin, J. D.; Dattelbaum, A. M.; Sullivan, R. M.; Thornton, T. A.; Wang, J.; Peachey, M. T. *Chem. Mater.* **1998**, *10*, 2699.

(2) Burdett, J. K.; Eisenstein, O. *Inorg. Chem.* **1992**, *31*, 1758.

(3) Van Vleck, J. H. *The Theory of Electric and Magnetic Susceptibilities*; Oxford University Press: Oxford, 1932.

(4) Martin, J. D.; Leafblad, B. R.; Sullivan, R. M.; Boyle, P. D. *Inorg. Chem.* **1998**, *37*, 1341.

(5) Sullivan, R. M.; Martin, J. D. *J. Am. Chem. Soc.* **2000**, *43*, 10092.

(6) Martin, J. D.; Greenwood, K. B. *Angew. Chem. Int. Ed. Eng.* **1995**, *34*, 233.

(7) Dattelbaum, A. M.; Martin, J. D. *Inorg. Chem.* **1999**, *38*, 2369.

(8) Dattelbaum, A. M.; Martin, J. D. *Inorg. Chem.* **1999**, *38*, 6200.

(9) Day, R. *Chem. Rev.* **1968**, *68*, 649.

(10) Yang, J. M.; Seeney, D. W. *Applied Optics* **1979**, *18*, 2398.

(11) Kauffman, G. B.; Fang, L. Y. *Inorg. Syn.* **1983**, *22*, 101.

(12) Developed at the U.S. National Institutes of Health and available on the Internet at http://rsb.info.nih.gov/nih-image/.

(13) Kiarus, W.; Molze, G. *POWDERCELL for Windows*; Federal Institute for Materials Research and Testing: Berlin, Germany, 1997. (http://www.bam.de/a_v/v_1/powder/e_cell.html)

(14) Wendlandt, W. W.; Hecht, H. G. *Reflectance Spectroscopy*; Interscience: New York, 1966; Chapter 3.

(15) Guloy, A. M.; Corbett, J. D. *Inorg. Chem.* **1996**, *35*, 4669.

(16) X-ray Research GmbH **1999**. Imaging-Plate Detector System (345 mm diameter). X-ray Research GmbH, Segeberger Chaussee 34. 22850 Norderstedt, Germany.

(17) Gabe, E. J.; Le Page, Y.; Charland, J.-P.; Lee, F. L.; White, P. S. *J. Appl. Crystallogr*. **1989**, *22*, 384.

(18) Altomare, A.; Burla, M. C.; Camulli, G.; Cascarano, G.; Giacovazzo, C.; Guagliardi, A.; Polidori, G. *J. Appl. Cryst.* **1994**, *27*, 435.

(19) Reitveld, H. M. *J. Appl. Crystallogr.* **1969**, *2*, 65.

(20) Young, R. A. *The Reitveld Methos: IUCr Monographs on Crystallogrophy*; Oxford University Press: New york, 1993.

(21) Larson, A. C.; Von Dreele, R. B. *GSAS: General Structure Analysis System Manual*; Los Alamos Report LAUR 86-748; Los Alamos National Laboratory: Los Alamos, NM, 1986.

(22) Flack, H. D. *Acta Cryst.* **1987**, *A43*, 564.

(23) Le Page, Y.; Donnay, J. D. H.; Donnay, G. *Acta Cryst.* **1984**, *A40*, 679.

(24) Herbst-Irmer, R.; Sheldrick, G. M. *Acta Cryst.* **1998**, *B54*, 443.

(25) The full structure report for the low temperature refinement is available in the Supporting Information.

(26) Garro, N.; Cantarero, A.; Cardona. M.; Ruf, T.; Göbel, A.; Lin, C.; Reimann, K.; Rübenacke, S.; Stuebe, M. *Sol. State Comm.* **1996**, *98*, 27.

(27) Ferhat, M.; Zaoui, A.; Certier, M.; Khelifa, B. *Phys. Lett. A* **1996**, *216*, 187.

(28) Li, H.; Laine, A.; Yaghi, O. *Science* **1999**, *283*, 1145.

(29) Bowes, C. L.; Ozin, G. A. *Adv. Mater.* **1996**, *8*, 13, and references therein.

(30) Jiang, T.; Lough, A. J.; Ozin, G. A.; Young, D.; Bedard , R. L. *Chem. Mater.* **1995**, *7*, 245.

(31) Ko, Y.; Tan, K.; Nellis, D. U.; Kock, S.; Parise, J. B. *J. Solid State Chem.* **1995**, *114*, 506.

(32) Nellis, D.M.; Ko, Y.; Tan, K; Koch, S.; Parise, J. B. *J. Chem. Soc., Chem. Commun.* **1995**, 541.

(33) Asplund, M.; Jagner, S. *Acta Chem. Scand.* **1984**, A38, 725.

(34) Andersson, S.; Jagner, S. *Acta Chem. Scand.* **1986**, A40, 210.

(35) Bowmaker, G. A.; Clark, G. R.; Yuen, D. K. P. *J. Chem. Soc., Dalton Trans.* **1976**, 2329.

(36) Rath, N. P.; Holt, E. M. *J. Chem. Soc., Chem. Comm.* **1985**, 665.

(37) Occupancies of 46.35%, 29.19%, and 15.65% were found for Cu(1), Cu(2), and Cu(3), respectively, when the thermal parameters were fixed at $B_{iso} = 0.08$.

(38) Larsen, E. M.; Wrazel, J. S.; Hoard, L. G. *Inorg. Chem.* **1982**, *21*, 2619.

(39) Garro, N.; Cantarero, A.; Cardona. M.; Ruf, T.; Göbel, A.; Lin, C.; Reimann, K.; Rübenacke, S.; Stuebe, M. *Sol. State Comm.* **1996**, *98*, 27.

(40) Ferhat, M.; Zaoui, A.; Certier, M.; Khelifa, B. *Phys. Lett. A* **1996**, *216*, 187.

(41) Dattelbaum, A. M.; Euliss, L. E.; Martin, J. D. Unpublished results.

(42) Ketelaar, J. A. A. T*rans. Faraday Soc.* **1938**, *34*, 874.

(43) Ketelaar, J. A. A. *Z. Phys. Chem., Abt. B* **1934**, *26B*, 327.

(44) Ketelaar, J. A. A. *Z. Phys. Chem., Abt. B* **1935**, *30B*, 53.

(45) Ketelaar, J. A. A. *Z. Kristalloga., Kristallgeom., Kristallphys., Kristallchem.* **1931**, *80*, 190.

(46) Ketelaar, J. A. A. *Z. Kristalloga., Kristallgeom., Kristallphys., Kristallchem.* **1934**, *87*, 436.

(47) Jaw, H.-R. C.; Mooney, M.. A.; Novinson, T.; Kaska, W. C.; Zink, J. I. *Inorg. Chem.* **1987**, *26*, 1387.

(48) Mulay, L. N.; Boudreaux, E. A. *Theory and Applications of Molecular Diamagnetism*, John Wiley & Sons: New York, 1976.

(49) Raychaudhuri, D. P., Sengupta, P. N. *Indian J. Phys.* **1936**, *10*, 245.

(50) Raychaudhuri, D. P., Sengupta, P. N. *Indian J. Phys.* **1936**, *10*, 253.

(51) Fowler, P. W.; Steiner, E. *J. Chem. Phys.* **1992**, *97*, 4215.

(52) Fowler, P. W.; Steiner, E. *J. Chem. Soc. Faraday Trans.* **1993**, *89*, 1915.

(53) Dronskowski, R. *J. Am. Chem. Soc.* **1995**, *117*, 1991.

(54) Asmussen, R. W.; Andersen, P. *Acta Chem. Scand.* **1958**, *12*, 939.

(55) Jansen, M.; Wagner, N.; Becker, M.; Wedig, U. *J. Am. Chem. Soc.* **2000**, *122*, 808.

(56) Oledzka, M.; Ramanugachary, K. V.; Greenblatt, M. *Chem. Mater.* **1998**, *10*, 322.

Chapter Four:

Benzene-Copper(I) Coordination in a Bimetallic Chain Complex

Andrew M. Dattelbaum and James D. Martin*

Department of Chemistry, North Carolina State University, Raleigh, NC 27695-8204.

(As published in *Inorg. Chem.* **1999**, *38*, 6200)

Abstract

The solvothermal reaction of CuCl and $ZrCl_6$ in benzene yields $((bz)CuCl_3)_2Zr$ (**1**) (bz = η^2-benzene), which has been characterized by single crystal X-ray diffraction with **a** = 6.1206(4), **b** = 11.1242(4), **c** = 13.6222(6), β = 93.675(3)° in the monoclinic space group $P2_1/m$, Z = 2. **1** adopts a one-dimensional chain structure constructed from zirconium chloride octahedra and $[(bz)CuCl_3]^{2-}$ tetrahedra. The $[(bz)CuCl_3]^{2-}$ units are shown to be metal-halide analogs of the phosphonate unit $[RPO_3]^{2-}$. Inter-chain interactions link chains of **1** along the crystallographic **c** direction *via* an edge-to-face π-stacking of the coordinated benzene molecules. The crystal packing forces influence dramatic second-order Jahn-Teller distortions making each of the two $((bz)CuCl_3)^{2-}$ units distinct. These interactions further result in ligand-to-metal and metal-to-ligand charge transfer that cause an activation of the benzene ligands.

4.1. Introduction

The synthesis and characterization of metalorganic solids, in which organic ligands link metal centers, has received considerable attention as a means of designing specific supramolecular assemblies. Amine, cyanide or organic-acid ligands frequently serve as part of the scaffold for such frameworks. In our effort to develop open-framework metal halides, we are interested in developing the organometallic (as opposed to metall-organic) solid-state chemistry by incorporating extra-framework organic ligands that can serve as active sites for catalysis. This model is patterned after the role of metal-alkyls in Ziegler-Natta catalysis.[1,2] Based on our recently described strategy for preparing metal-halide analogs of metal-oxide structure types,[3] we have considered the preparation of metal-halide analogs of the prolific class of metal phosphonates as a structural prototype for such organometallic solids. Both structurally and electronically, phosphonates $(RPO_3)^{2-}$ can be related to $(LCuCl_3)^{2-}$ where L is a neutral ligand such as an olefin, aromatic, carbonyl, etc. Such organometallic solid-state chemistry finds structural precedence in $(bz)CuAlCl_4$[4] (bz = η^2-benzene), which was not described in relation to this phosphonate analogy. In that material, benzene is bound to copper in an η^2-fashion. Each copper is bridged through chlorides to aluminum forming a layered clay-type structure with the benzene ligands coordinated in the inter-layer region. The benzene is readily lost from this layered structure to form α-$CuAlCl_4$.[5,6,7] Interestingly, $CuAlCl_4$ is reported to catalyze the polymerization of benzene in the presence of oxygen.[8] And the insertion of CO into aromatic C-H bonds is reported to be catalyzed by CuCl and a strong Lewis acid such as $AlCl_3$.[9] A related chemistry could also be described for $(bz)AgAlCl_4$

where the benzene is coordinated to a square pyramidal $AgCl_4$ unit of the $AgAlCl_4$ layers.[10] However, the silver to benzene interaction is reportedly weaker than the corresponding copper-benzene interaction.

Given the literature precedence for Cu(I) to reversibly bind unsaturated ligands, as well as its use as a co-catalyst with Lewis acids, [6,7,11,12] it seemed of interest to pursue the preparation of such phosphonate-type metal-halide materials with copper chloride and other Lewis acidic metal halides. In this report, we describe the preparation and characterization of $((bz)CuCl_3)_2Zr$ (**1**), a one-dimensional chain structure constructed from zirconium octahedra and copper tetrahedra. Chains of **1** are linked along the crystallographic **c** direction *via* an edge-to-face π-stacking of the coordinated benzene molecules. These crystal packing forces are shown to influence dramatic second-order Jahn-Teller distortions making each of the two $((bz)CuCl_3)^{2-}$ units distinct. The distortions of the distinct $((bz)CuCl_3)^{2-}$ units emphasize the unique donor and acceptor properties of the Cu(I) ion, which in turn result in differential activation of the aromatic ligands.

4.2. Experimental

General Procedures. All reactions were performed under an inert atmosphere of dry N_2 in a glove box or using Schlenk line techniques. $ZrCl_4$ (99.99%) was used as received from Aldrich. The CuCl was prepared from Cu metal and $CuCl_2$ (Aldrich) according to literature methods and further purified by sublimation.[13] Benzene (99.9%, Fisher) was distilled from Na/benzophenone, then stored under nitrogen and over

molecular sieves. All powder X-ray diffraction measurements were obtained using an Enraf-Nonius Guinier camera and were indexed with respect to a silicon standard.

Preparation of Cu_2ZrCl_6, (2). A sample of 0.200 g of $ZrCl_4$ (0.858 mmols) and 0.140 g of CuCl (1.72 mmols) were ground together in a mortar and pestle, then transferred to a fused silica tube (6mm I.D. × 8 cm). The reaction vessel was evacuated and sealed with a torch. The reaction was heated to 450°C (above the melting point of CuCl) in a box furnace for 1 day, followed by cooling at 1.0°C/min. A small temperature gradient in the furnace caused crystalline Cu_2ZrCl_6 to sublime to the cool end of the tube in greater than 90% yield. Solution of the single crystal X-ray structure is complicated by disorder and/or twinning and, thus, will be the subject of a subsequent report.[14]

Preparation of $((bz)CuCl_3)_2Zr$ (1). A powdered sample of Cu_2ZrCl_6 (0.15 mg, 0.0348 mmols) was placed in a thick walled fused silica tube (10mm O.D. × 6mm I.D). On a Schlenk line, 1.0 ml of benzene was added to the reaction vessel. The reaction mixture was frozen with liquid N_2 and sealed using a torch such that the fused silica vessel was filled to 25% volume. The reaction mixture was heated to 150°C for one week then slow cooled at a rate of 0.1°C/min to yield a pale yellow crystalline solid (50% yield) from which a single crystal was isolated for an X-ray structure determination. (*Note of Caution: upon heating the sealed reaction vessel significant pressures are generated which can lead to vessel rupture. Appropriate shielding should be utilized such as placing the reaction vessels in a capped iron pipe during heating.)* After the crystalline material is removed from the benzene solvent it gradually looses the coordinated benzene such that elemental analyses routinely exhibit a 20-25% loss of

benzene for any given sample. Elemental analysis observed for $C_{12}H_{12}Cl_6Cu_2Zr$, 1) C: 17.20% and H: 1.85% 2) C: 18.11%, and H: 1.60%, calculated, C: 24.04% and H 2.04%.

X-ray structure determination of $((bz)CuCl_3)_2Zr$ (1). A single crystal (0.28 x 0.20 x 0.14 mm) was mounted in a Pyrex capillary under a N_2 atmosphere covered in silicone grease to decrease the loss of solvent. Single crystal X-ray data were collected on an Enraf-Nonius CAD4 diffractometer at 298 K using Mo K_α radiation (λ = 0.71073 Å). Final cell constants were determined by a symmetry constrained fit of 24 well centered reflections ($35° < 2\theta < 40°$) and their Friedel pairs. A hemisphere of data, ±h, ±k, l, with 2108 unique reflections was collected by the $\theta/2\theta$ scan mode out to $\theta < 27$. Data was scaled to the intensity check reflections using a five point smoothing curve fitting routine. An empirical absorption correction was applied using psi scan data.

Systematic absences were found to be consistent with the space group $P2_1/m$ which was confirmed in the subsequent refinement. The structure was refined using the NRCVAX suit of programs.[15] All non-hydrogen atoms were located by direct methods using the SIR92 program[16] and refined anisotropically in the final refinement. Hydrogen atoms bound to the benzene rings were then added in calculated positions and assigned fixed temperature factors. A full matrix least squares calculation using the 1456 unique reflections ($I > 1.0\ \sigma(I)$) gave a final refinement with R factors of R = 0.044 and R_w = 0.054. The final difference map was flat with the largest peak (1.5 $e^-/Å^3$) located 0.968 Å from Cu(2).

Extended Hückel Calculations[17] were performed on $((bz)CuCl_3)^{2-}$ fragments idealized from the crystal structure of **1**. Atomic and orbital parameters used were those

from previously published works.[18,19,20] The Cu-Cl bond lengths were idealized to 2.3 Å, while the Cl-Cu-Cl angles were taken directly from the crystalline structure. Idealized benzene rings with C-C = 1.39 Å were made to interact with the $(CuCl_3)^{2-}$ fragment using the two orientations and copper to benzene distances found in the crystal structure for Cu(1) and Cu(2), respectively.

4.3. Results

A summary of crystallographic data for $((bz)CuCl_3)_2Zr$ (**1**) is given in Table 4.1, and selected bond distances and angles in Table 4.2. An ORTEP drawing of the 1-D chain structure of **1** is shown in Figure 4.1 and a view of the unit cell looking down **a** is given in Figure 4.2. The structure of **1** consists of chains running along **a** in which the phosphonate-like tetrahedral units, $((bz)CuCl_3)^{2-}$, are linked by Zr^{+4} cations. The chains lie across the mirror plane such that two pairs of chloride ligands (Cl(2) and Cl(2'), and, Cl(4) and Cl(4')) bridge the copper tetrahedra and zirconium octahedra resulting in common edges of the polyhedra. The additional chloride ligands bridge vertices of the copper tetrahedra and zirconium octahedra. The two $(bz)CuCl_3$ units are notably distinct, moved away from being related through an approximate center of inversion by inter-chain edge-to-face π-stacking of the benzene ligands (discussed below).

The benzene molecules are bound to the copper sites by an η^2-mode of coordination. Lying across the mirror plane, the benzene ligands are coordinated symmetrically to the copper atoms, with Cu-C distances of 2.306(7)Å and 2.200(6) Å for Cu(1) and Cu(2), respectively. The distance to the midpoint of the C-C bond (X) is

Table 4.1. Crystallographic data for $((bz)CuCl_3)_2Zr$ (**1**).

formula	$((C_6H_6)CuCl_3)_2Zr$
formula weight(g/mol)	587.25
space group (No.)	P 2_1/m (11)
color	yellow
a (Å)	6.1206(4)
b (Å)	11.1242(4)
c (Å)	13.6222(6)
β, °	93.675(3)
V (Å^3)	925.58(8)
temp. (°C)	25
Z	2
ρ_{calcd} (mg cm^{-3})	2.107
λ(Mo K_α), Å	0.71073
μ (cm^{-1})	36.9
R^a	0.044
$R_w{}^b$	0.053
GOF^c	1.56

$^aR_f = (\Sigma(F_0 - F_c)/F_0)$. $^bR_w = [\Sigma(w(F_0 - F_c)^2)/ wF_0{}^2)]^{½}$.
^{c}GOF = $[\Sigma(w(F_0 - F_c)^2)/$(No. of reflns. - No. of parameters)$]^{½}$

Table 4.2. Selected Bond Distances (Å) and Bond Angles (deg.) for $((bz)CuCl_3)_2Zr$.

Zr-Cu(1)	3.328(1)	Cu(1)-C(1)	2.306(7)
Zr-Cu(2)	3.222(2)	Cu(1)-X(1)*	2.205
		Cu(2)-C(4)	2.200(6)
Zr-Cl(1)	2.483(2)	Cu(2)-X(2)*	2.087
Zr-Cl(2) × 2	2.467(2)		
Zr-Cl(3)	2.436(2)	C(1)-C(1')	1.35(2)
Zr-Cl(4) × 2	2.485(2)	C(1)-C(2)	1.39(1)
		C(2)-C(3)	1.37(1)
Cu(2)-Cl(3)	2.664(3)	C(3)-C(3')	1.35(2)
Cu(2)-Cl(4)	2.335(2)		
Cu(2)-Cl(4)	2.335(2)	C(4)-C(4')	1.39(1)
		C(4)-C(5)	1.40(1)
Cu(1)-Cl(1)	2.325(2)	C(5)-C(6)	1.35(1)
Cu(1)-Cl(2)	2.403(2)	C(6)-C(6')	1.39(2)
Cu(1)-Cl(2)	2.403(2)		

Cl(1)-Zr-Cl(2)	89.06(5)	Cl(1)-Cu(1)-Cl(2)	110.99(6)
Cl(1)-Zr-Cl(2)	89.06(5)	Cl(2)-Cu(1)-Cl(2)	94.24(6)
Cl(1)-Zr-Cl(3)	179.65(8)	Cl(3)-Cu(2)-Cl(4)	101.10(6)
Cl(1)-Zr-Cl(4)	90.43(5)	Cl(4)-Cu(2)-Cl(4)	96.38(7)
Cl(1)-Zr-Cl(4)	90.43(5)		
Cl(2)-Zr-Cl(3)	91.18(5)	Cl(1)-Cu(1)-C(1)	113.2(2)
Cl(2)-Zr-Cl(4)	178.79(6)	Cl(2)-Cu(1)-C(1)	98.5(2)
Cl(3)-Zr-Cl(4)	89.32(6)	Cl(3)-Cu(2)-C(4)	90.6(2)
		Cl(4)-Cu(2)-C(4)	111.6(2)
Zr-Cl(1)-Cu(1)	130.5(1)		
Zr-Cl(2)-Cu(1)	86.23(5)	C(1)-C(1')-C(2)	119.5(7)
Zr-Cl(3)-Cu(2)	132.7(1)	C(1)-C(2)-C(3)	120.5(8)
Zr-Cl(4)-Cu(2)	83.81(6)	C(2)-C(3)-C(3')	120.0(7)
Cu(1)-Zr-Cu(2)	174.92(4)	C(4)-C(4')-C(5)	119.8(6)
		C(4)-C(5)-C(6)	119.4(7)
		C(5)-C(6)-C(6')	120.8(6)

*X = midpoint of the C-C bond bound to its respective copper atom.

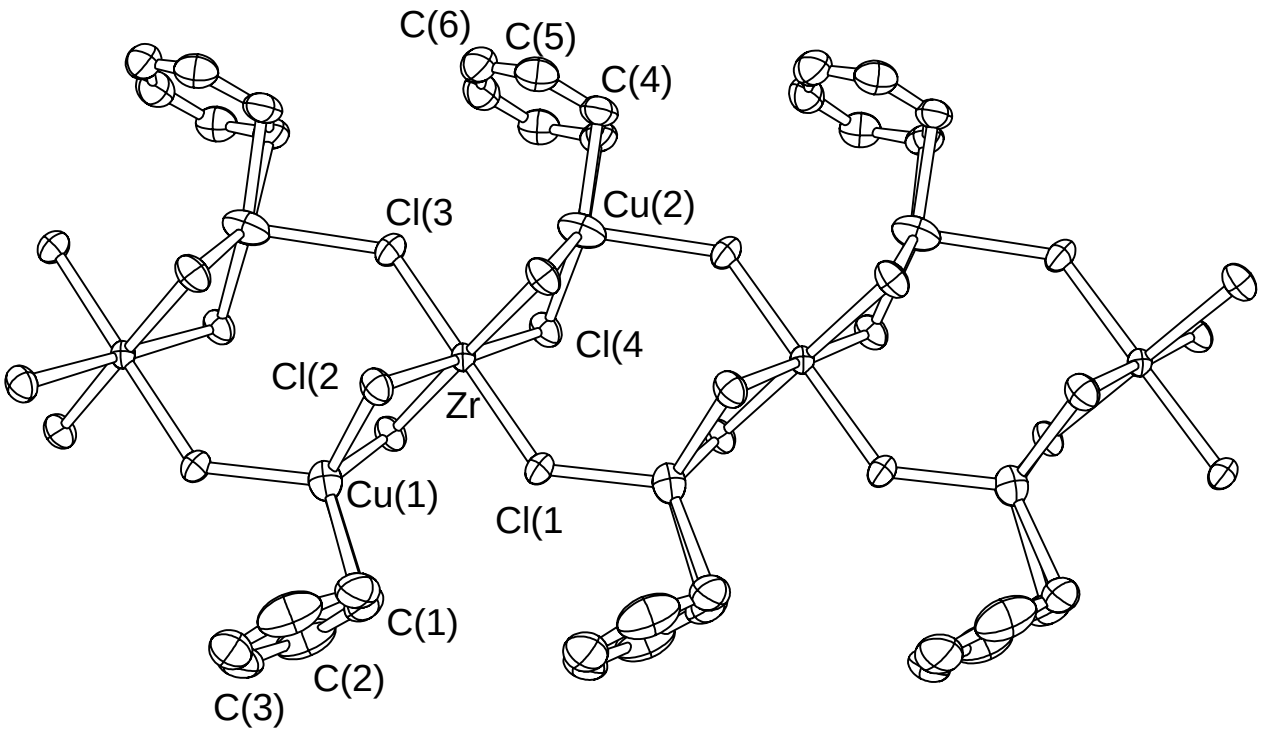

Figure 4.1. ORTEP drawing of the chains in $((bz)CuCl_3)_2Zr$(**1)** running along **a**. Thermal displacement ellipsoids are drawn at 50%.

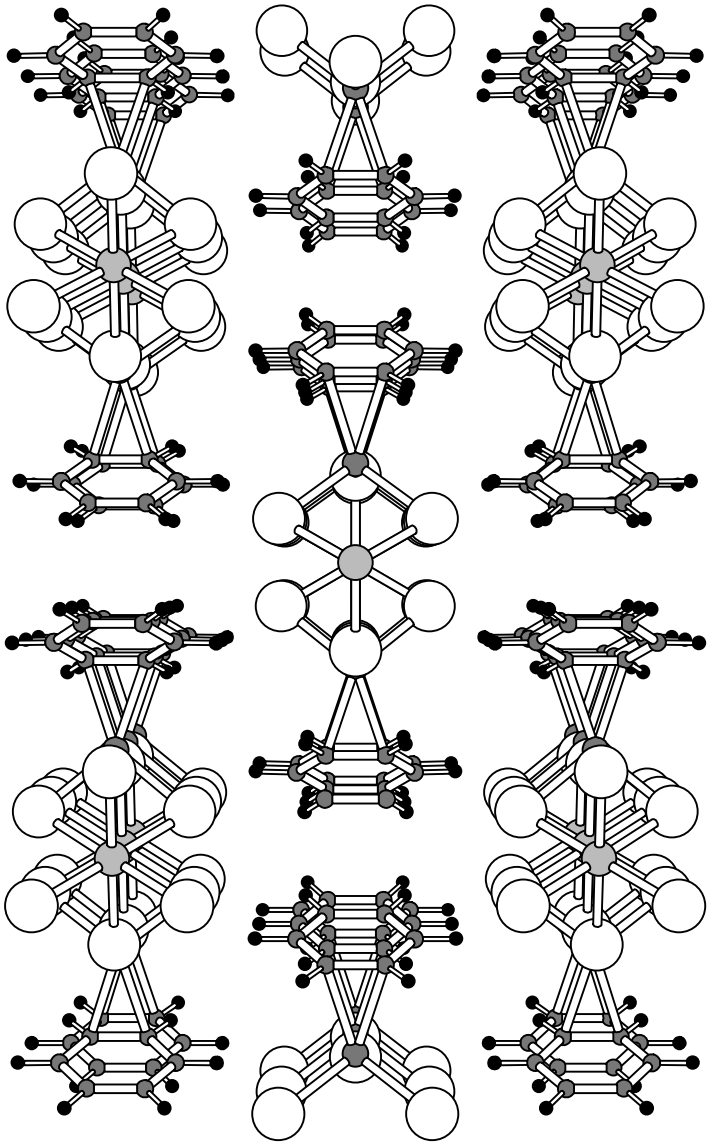

Figure 4.2. Ball and stick drawing of $((bz)CuCl_3)_2Zr$(**1**) viewed down the **a** direction.

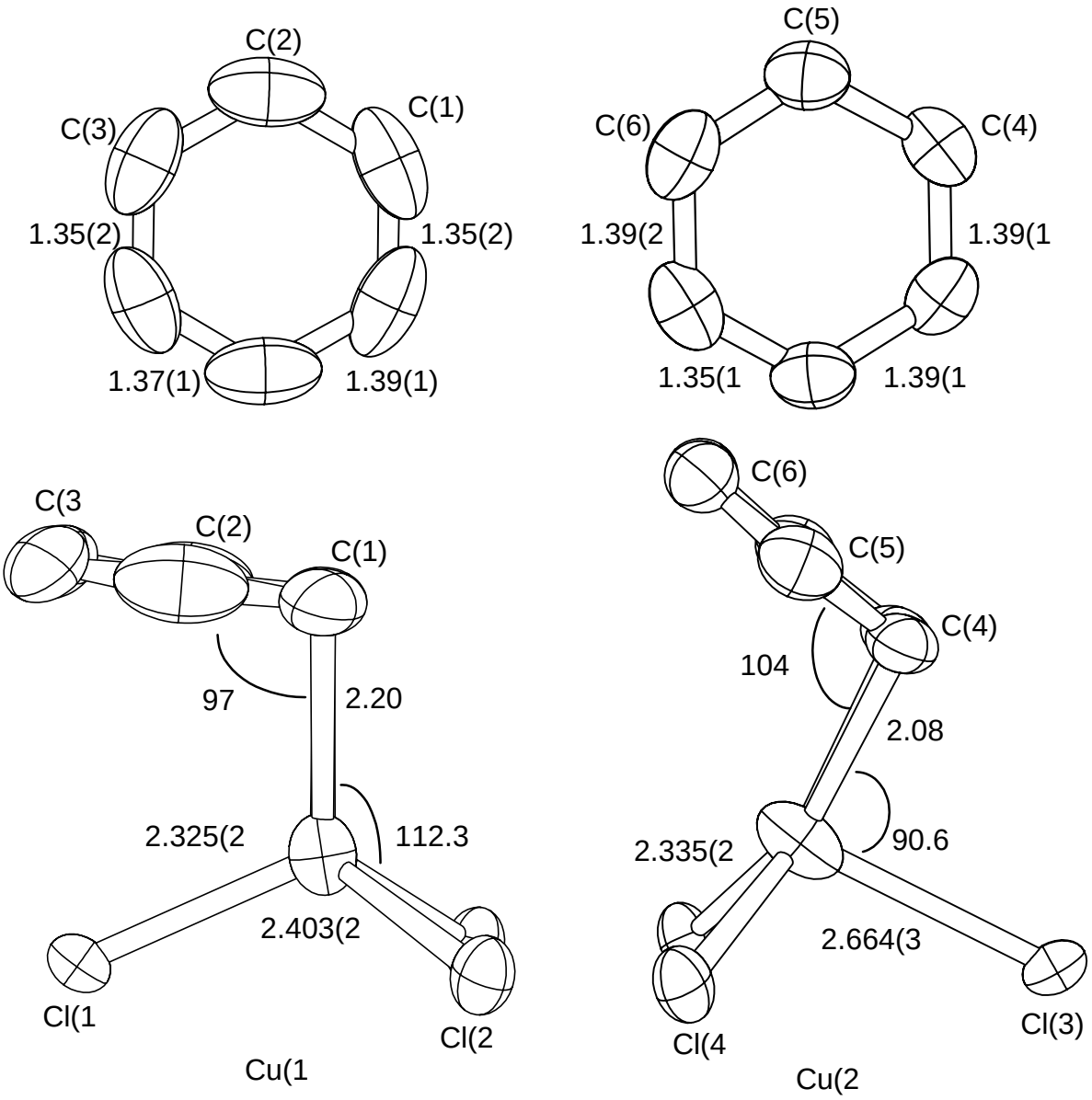

Figure 4.3. ORTEP drawings of the two distorted copper phosphonate-like building blocks in $((bz)CuCl_3)_2Zr$(**1**).

Cu(1)-X(1) = 2.205 Å and Cu(2)-X(2) = 2.087 Å. In addition to the notable variation in bond distances to the respective benzene ligands, a distinct coordination geometry is also observed at Cu(1) and Cu(2) as seen in Figure 4.3. The benzene coordinated to Cu(1) forms a tetrahedron (based on the midpoint of the coordinated C-C bond) with the angles Cl(2)-Cu(1)-X(1) = 112.3 ° and Cl(1)-Cu(1)-X(1) = 114.3° and is oriented such that the ring lies over one of the three Cu-Cl bonds. By contrast, the coordination at Cu(2) is distorted toward a trigonal prismatic or nearly trigonal planar geometry with Cl(3)-Cu(2)-X(2) = 90.6° and Cl(4)-Cu(2)-X(2) = 129.5°. Here, the benzene is coordinated such that the ring lies over two of the three Cu-Cl bonds. The coordination to copper has apparently disrupted the aromaticity of both benzene ligands, although the errors in the C-C bond distances are too great to draw definitive conclusions. There is a qualitative difference in the C-C bond lengths of the benzene ligands coordinated to each copper (see Table 4.2 and Figure 4.3) which were consistently observed in the structural solution of the single crystal X-ray diffraction data for two different crystals. The C(1)-C(1') bond, 1.35(2) Å, bound to Cu(1) is significantly shorter than the corresponding C(4)-C(4') bond, 1.39(1) Å, which is bound to Cu(2).

The zirconium octahedra are relatively idealized with six approximately equal Zr-Cl distances, avg. Zr-Cl = 2.47 Å (Table 4.2). However, the significant differences between Cu(1) and Cu(2) are also seen in the dramatic variation in the copper-chloride bond distances (Figure 4.3). A 0.07Å bond elongation of the two Cu(1)-Cl(2) bonds (2.403(2) Å), with respect to the Cu(1)-Cl(1) bond length of 2.325(2) Å, is observed at the Cu(1). (An average $Cu^{(I)}$-Cl single bond distance is ca. 2.3Å based on the sum of

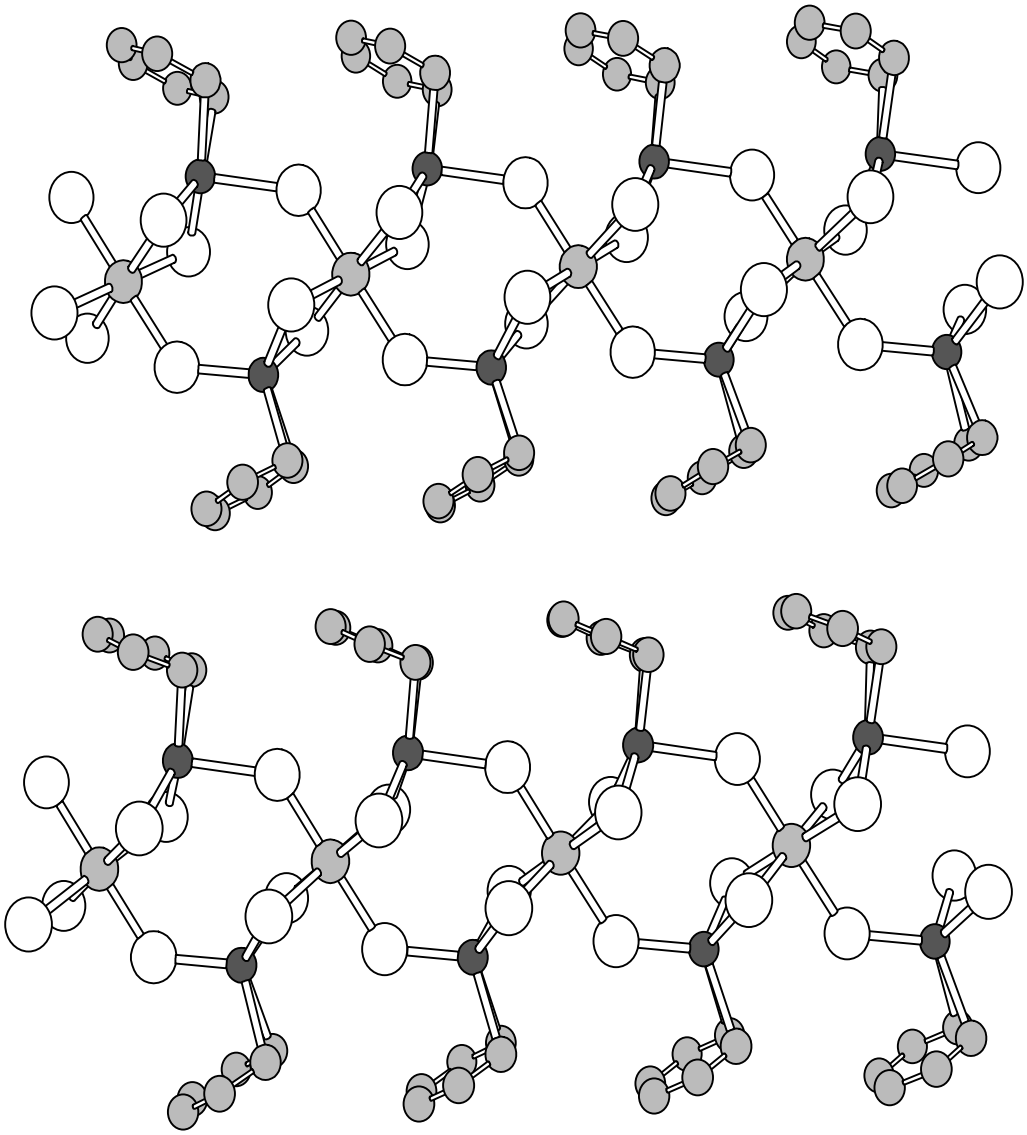

Figure 4.4. Ball and stick drawing of the chains in $((bz)CuCl_3)_2Zr$(**1**) stacked along the **c** direction to indicate the edge-to-face π-interactions between chains. Chlorides are the unshaded, larger balls. Zirconium atoms are the larger, gray balls, while carbon atoms are the smaller gray balls. Copper atoms are the darkest spheres shown.

their crystal radii.)[21] By contrast, the Cu(2)-Cl(3) bond (2.664(3) Å) is elongated by 0.3Å with respect to the two Cu(2)-Cl(4) bonds at 2.335(2)Å, where the elongated distance forms an axial-type coordination above a trigonal ligand plane.

The primary inter-chain interactions are observed by the stacking of the chains along **c** as shown in Figure 4.4. The edge of the benzene coordinated to Cu(1) is directed toward the face of the benzene ligand bound to Cu(2), and visa versa, such that short inter-chain contacts are observed, similar to that observed in the crystal structure of benzene itself.[22,23] The shortest inter-chain contacts are between the face of the benzene attached to Cu(2) and the edge of the benzene bound to Cu(1). (The face center to midpoint of C(3)-C(3') is ca. 3.71 Å.) The corresponding distance between the center of the face of the benzene attached to Cu(1) to the midpoint of the C(6)-C(6') bond is ca. 3.94 Å. Interestingly, there are no short contacts between the protons on the benzene ligands and the chloride ligands of neighboring chains. The shortest H---Cl distances are the intra-chain contacts H(4)-Cl(3) = 2.92(2) Å, H(1)-Cl(2) = 3.14(2) Å and H(1)-Cl(1) = 3.35(2) Å. The shortest inter-chain H---Cl contacts are H(6)-Cl(4) = 3.001(2) Å and H(3)-Cl(2) = 3.03(1) Å which only provide a weak link between chains along **b**.

4.4. Discussion

Synthesis: 1 is readily synthesized in high yield from the solvothermal reaction of Cu_2ZrCl_6 in benzene. It is also possible to synthesize **1** directly from CuCl and $ZrCl_4$ in superheated benzene. However, reactions starting with the binary halides normally result in a product with unreacted CuCl. Cuprous chloride is a very persistent species in

both solvothermal and melt reactions, often requiring reactions to be heated to near its melting point to ensure complete reaction. Once the ternary Cu_2ZrCl_6 is formed from the melt of the two binary components, it is very amenable to further reaction in superheated benzene.

A Metal-Phosphonate Analog: In a recent report, we described the analogy between $[CuCl_4]^{3-}$ and the thiophosphate $[PS_4]^{3-}$, where we demonstrated the structural relationship between $[(ZrCl_2)CuCl_4]^-$ [24]and $[MPS_4]^-$ (M = Ni[25], Pd[26]). Based on this same halide for chalcogenide charge matching scheme, $[(bz)CuCl_3]^{2-}$ can be viewed as isoelectronic and isostructural to the phosphonate tetrahedral building blocks, $[RPO_3]^{2-}$ (R = alkyl or aryl). A search of the Cambridge Structural Database[27] finds no 1-D phosphonate for which **1** is a direct analog. However, a close structural match is found for the 1-D phosphonate $((\mathbf{R}PO_3H)_2ZrF_2)^-$ (**R** = $CH_2NH(CH_2CO_2)_2$) which was reported by Clearfield and coworkers and is shown in Scheme 1.[28] A figurative loss of HF would allow for the condensation to an edge-bridge phosphonate, which would then be a direct structural analog to **1**. The absence of a direct phosphonate analog to **1** is again understood because of the difference between the metal-oxygen and metal-chloride bond lengths.[3] The shorter M-O bond distance normally precludes the edge-shared type connectivity for octahedral and tetrahedral building blocks in the absence of metal-metal bonding. Though uncommon, edge-bridged connectivity between octahedral divalent metals and a phosphonate is observed for the 1-D chain structure of $M^{II}(HO_3P(C_6H_5))\bullet H_2O$ (where M = Ca, Mg, Mn,[29] Zn[30]).

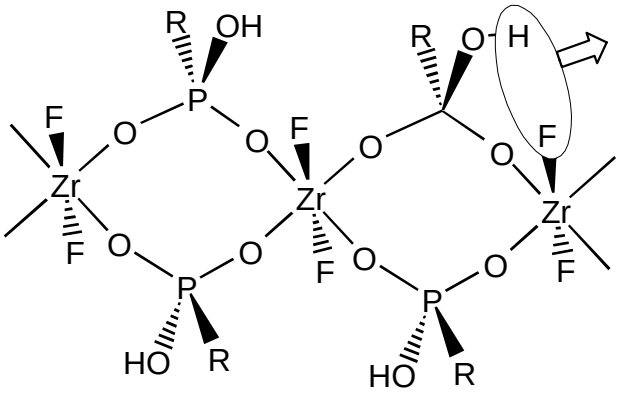

Scheme 1

Understanding the Structural Distortion of the Copper Tetrahedra. Bonding interactions to copper (I) are known to be quite complex and varied.[31] The occupied $3d^{10}$-orbitals are of sufficient size and energy that π-backbonding can be observed.[4] The empty 4s and 4p orbitals are rather low in energy which allows copper (I) to act as an acceptor,[32] as well as facilitating distortions due to a second-order Jahn-Teller mixing into the occupied d levels.[33] The η^2-arene can also function as both a Lewis base or a Lewis acid, making use of its π and π* orbitals, respectively.[34] Given the bonding interactions observed in the crystal structure of **1** with longer Cu(1)-C(1) and a shorter C(1)-C(1') bonds as compared to the shorter Cu(2)-C(4) and longer C(4)-C(4'), one might suspect that each copper site exhibits a different bonding limit (ligand-to-metal or metal-to-ligand charge transfer). These bonding limits are readily articulated by a consideration of the frontier orbitals of the respective fragments.

The bonding distortions around Cu(2) are most pronounced, and similar to those frequently observed for olefins coordinated to copper halides.[35,36] A second-order mixing

of the higher-lying empty 4s and 4p orbitals into the occupied 3d orbitals on Cu drives a rehybridization that maximizes the possibility for π-back bonding into the unsaturated ligand. Overlap for π-back bonding is not well supported by a d^{10}-configuration in a tetrahedral geometry. However, distortion to the nearly trigonal-planar geometry observed around Cu(2) provides excellent overlap between the new π-type orbital on copper and a π*-orbital of benzene shown in **A**. The formation of strong back-bonding into a π*-orbital accounts both for the shortened Cu(2)-C(4) distance, as well as the lengthened C(4)-C(4') distance. The rehybridization on going to the near trigonal-planar geometry also serves to mix significant antibonding character into the Cu(2)-Cl(3) bond as seen in the decreased overlap population listed in Table 4.3. The empty 4s and 4p molecular orbitals on copper have significant Cu-Cl σ* character, which when mixed into the former "t_2"-type d-orbital of copper yields the molecular orbital **B**. Here, the second-order mixing has maximized antibonding to Cl(3), but is effectively non-bonding with

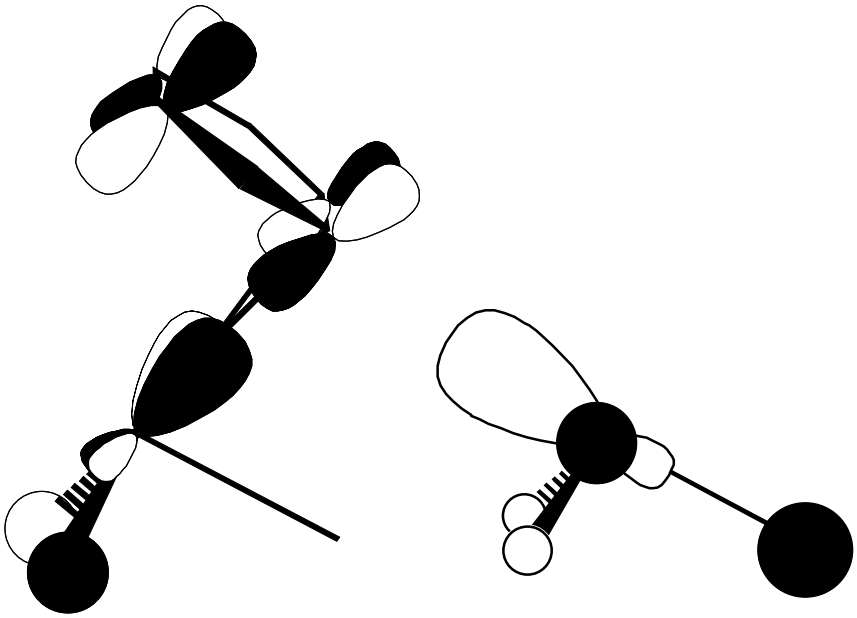

A **B**

Table 4.3. Overlap populations calculated from idealized $((bz)CuCl_3)^{2-}$ fragments.

	Cu(1)		Cu(2)
Cl(1)	0.3766	Cl(3)	0.334
Cl(2)	0.3529 × 2	Cl(4)	0.3522 × 2
C(1)-C(1')	1.0420	C(4)-C(4')	1.0356
C(1)-C(2)	1.0659	C(4)-C(5)	1.0598
C(2)-C(3)	1.0902	C(5)-C(6)	1.0915
C(3)-C(3')	1.0702	C(6)-C(6')	1.0683
Total Charge on Cu	11.0677		11.0317

respect to Cl(4). Hence, the rehybridization to maximize π-back bonding to benzene comes at the expense of only one elongated copper-chloride bond.

A clearly different bonding motif is observed for Cu(1) which exhibits a more nearly ideal tetrahedral geometry, and longer copper to benzene bonds. The larger thermal ellipsoids observed for this benzene ligand, though increasing the errors for the C-C distances, are also consistent with the weaker binding of this ligand. The C(1)-C(1') bond of the benzene ligand lies directly across one vertex of a tetrahedron with the plane of the ring essentially parallel to the three chloride ligands which make up its base. To a first approximation, the bonding of benzene to Cu(1) can be viewed as a result of the mixing of an empty sp-hybrid on copper with an occupied π-orbital of benzene and the filled dz^2 orbital on copper of the same symmetry (shown in **C**). The electron density transferred out of this π-bond is not sufficient to cause a significant lengthening of the C(1)-C(1') bond. But this analysis alone does not provide explanation for the elongation of two of the three Cu-Cl bonds by nearly 0.1Å, or the dearomatization of the coordinated benzene. To understand this distortion, we first note that unlike the distortion observed around Cu(2), this type of distortion does not have precedence in copper-chloride olefin complexes. Unlike a simple olefin, benzene has several occupied π-type orbitals that may become involved in interacting with the metal center. While the primary σ-interaction with Cu(1) is formed with one π-orbital (shown in **C**), another of benzene's π-type orbitals is oriented so as to provide reasonable π-type overlap with one of the "t_2"-type orbitals of the copper fragment shown in **D**. This metal-based orbital is σ-anti-bonding with respect to the two Cu(1)-Cl(2) bonds. Thus, this filled-filled interaction is stabilized

by mixing with the empty Cu 4p-orbital. The strong Cu-Cl antibonding character of the Cu 4p orbital that is mixed into this occupied molecular orbital results in the elongation of two of the three Cu-Cl bonds (also seen in the overlap population listed in Table 4.3). This interaction also results in the decrease in the bonding angle of the plane of the benzene ring to the copper from 104° at Cu(2) to 97° at Cu(1) which appears to indicate a move towards a slightly greater hapticity ($\eta^2 \rightarrow \eta^4$). Such a distortion cannot be observed for olefin complexes since olefins do not possess multiple occupied π-type orbitals. Furthermore, removing electron density from this "e_g"-type π orbital of benzene (shown in **D**) is consistent with the observed dearomatization with longer adjacent C(1)-C(2) = 1.39(1)Å and C(2)-C(3) = 1.37(1)Å bonds and shorter C(1)-C(1') = 1.35(2)Å and C(3)-C(3') = 1.35(2)Å bonds.

The distinct coordination environments of the two copper sites in **1** reaffirm the precedent that the coordination sphere of copper (I) is quite flexible. The two bonding motifs seem clearly to be a result of ligand-to-metal charge transfer (for Cu(1)) and metal-to-ligand charge transfer (for Cu(2)). But why should these two distinct chemistries be present in this one structure? Looking beyond the bonding within the isolated chains, strong inter-chain interactions in the form of edge-to-face π-stacking of the benzene rings are apparent (Figure 4.4) that provide a significant influence in directing the charge transfer between metal and ligands. The partial negative charge on the face of an aromatic ring is frequently associated with the partial positive charge on the edge of a neighboring ring giving rise to substantial crystal packing forces. As noted above, and in Figure 4.4, the closest contact between the edge of the benzene ligand bound to Cu(1) and

the center of the face of the benzene ligand bound to Cu(2) is 3.71Å, which is slightly shorter than the distance of 3.75Å found in the crystal structure of benzene itself. This interaction is favored by the respective charge transfer to and from the copper centers.[22,23] The ligand-to-metal charge transfer at Cu(1) depletes the electron density in the ring making a slightly more positively charged edge. By contrast, the metal-to-ligand charge transfer at Cu(2) increases the electron density, and thus the negative charge on the face of this ring.

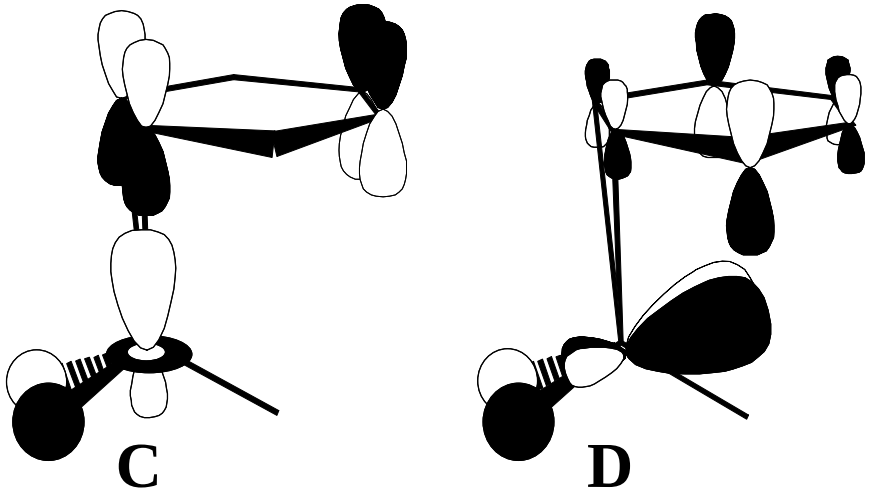

C **D**

4.5. Conclusions

In summary, benzene is demonstrated to be a useful solvent for the solvothermal synthesis of metal-halide materials, such as $((bz)CuCl_3)_2Zr$ (**1**). The benzene coordinates to copper (I) forming the tetrahedral building block $[(bz)CuCl_3]^{2-}$, which is recognized as an isostructural and isoelectronic metal-halide analog of the metal-phosphonate unit

$[RPO_3]^{2-}$. The chains formed in the crystal structure of **1** are oriented so as to exhibit edge-to-face π-stacking of the benzene rings, which promotes ligand-to-metal and metal-to-ligand charge transfer at Cu(1) and Cu(2), respectively. The ability for such inter-chain forces to direct the charge transfer between copper and the arene ligands bound to it imply that copper (I) can reasonably serve as an "electron buffer." The dearomatization on coordination *via* metal-to-ligand charge transfer may make the aromatic ligand susceptible to electrophilic attack similar to that described for the η^2-arene complexes of osmium and ruthenium.[34] By contrast, the ligand-to-metal charge transfer should make the ligand subject to nucleophilic attack as observed for the η^6-arene complexes of earlier transition metals.[37]

Acknowledgments

We would like to thank Ann E. Bunner for the contributions she made on this project as part of a summer high school research program and Dr. Paul Boyle for collecting the crystallographic data. This work was supported by the National Science Foundation CAREER award, (DMR-9501370) and instrumentation grant (CHE-9509532). J. D. Martin is a Cottrell Scholar of the Research Corporation.

Supporting Information Available: An X-ray crystallographic file in CIF format for the structure determination of $((bz)CuCl_3)_2Zr$ (**1**). This material is available free of charge via the Internet at http://pubs.acs.org.

4.6. References

(1) Ziegler, K.; Holzkamp, E.; Breil, H. *Angew. Chem.* **1955**, *67*, 541.

(2) Natta, G. *Macromol. Chem.* **1955**, *16*, 213.

(3) Martin, J. D.; Dattelbaum,A. M.; Sullivan, R. M.; Thornton, T. A.; Wang, J.; Peachey, M. T. *Chem. Mater.* **1998**, *10*, 2699.

(4) Turner R. W.; Amma, E. L. *J. Am. Chem. Soc.* **1966**, *88*, 1877.

(5) Martin, J. D.; Leafblad, B. R.; Sullivan, R. M.; Boyle, P. D. *Inorg. Chem.* **1998**, *37*, 1341.

(6) "Luminescent Materials" Ed. J. McKittrick; *Proc. Mat. Res. Soc.* **1999**, *560*, in press.

(7) Sullivan, R. M.; Martin J. D. *J. Am. Chem. Soc.*, in press.

(8) Toshima, N.; Kanaka, K.; Koshirai, A.; Hirai, H. *Bull. Chem. Soc. Jpn.* **1988**, *61*, 2551.

(9) Gatterman, L.; Koch, H. *Chem. Ber*. **1897**, *30*, 1622.

(10) Turner R. W.; Amma, E. L. *J. Am. Chem. Soc.* **1966**, *88*, 3243.

(11) B. J. Hathaway *Comprehensive Coordination Chemistry*; Wilkinson, G.; Gillard, R. D.; McCleverty, J. A., Eds.; Pergamon: London, 1987; vol. 5, ch 53.3.2.11, pp. 568-571.

(12) Karlin, K. D.; Gultneh, Y. *Prog. Inorg. Chem.* **1987**, *35*, 219.

(13) Kauffman, G. B.; Fang, L. Y. *Inorg. Syn*. **1983**, *22*, 101.

(14) Dattelbaum, A. M.; Martin, J. D. To be published.

(15) Gabe, E. J.; Le Page, Y.; Charland, J.-P.; Lee, F. L.; White, P. S. *J. Appl. Crystallogr*. **1989**, *22*, 384.

(16) Altomare, A.; Burla, M. C.; Camulli, G.; Cascarano, G.; Giacovazzo, C.; Guagliardi, A.; Polidori, G. *J. Appl. Cryst.* **1994**, *27*, 435.

(17) Hoffman, R. D. *J. Chem. Phys.* **1963**, *39*, 1397.

(18) Ammeter, J. H.; Bürgu, H.-B.; Thibeault, J. C.; Hoffman, R. J. *J. Am. Chem. Soc.* **1978**, *100*, 3686.
(19) Hay, P. J.; Thibeault, J. C.; Hoffman, R. J. *J. Am. Chem. Soc.* **1975**, *97*, 4884.

(20) Summerville, R. H. Hoffman, R. J. *J. Am. Chem. Soc.* **1976**, *98*, 7240.

(21) Shannon, R. D. *Acta Cryst.* **1976**, *A32*, 751.

(22) Cox, E. G.; Cruickshank, W. J.; Smith, J. A. *Proc. R. Soc. London, Ser. A* **1958**, *247*, 1.

(23) Bacon, G. E.; Curry, N. A.; Wilson, S. A. *Proc. R.. Soc. London, Ser. A* **1964**, *279*, 98.

(24) Dattelbaum, A. M.; Martin, J. D. *Inorg. Chem.* **1999**, *38*, 2369.

(25) Chondoudis, K.; Kanatzidis, G.; Sayettat, J.; Jobic, S.; Brec, R. *Inorg. Chem*. **1997**, *36*, 5859.

(26) Elder, S. H.; Van der Lee, A.; Brec, R.; Canadell, E. *J. Solid State Chem*. **1995**, *116*, 107.

(27) 3D Search and REsearch Using the Cambridge Structural Database. Allen, F. H.; Kennard, O. *Chemical Design Automation News* **1993**, *8*, 1 & 31.

(28) Zhang, L.; Poojary, D. M.; Clearfield, A. *Inorg. Chem.* **1998**, *37*, 249.

(29) Cao, G.; Lee, H.; Lynch, V. M. ; Mallouk, T. E. *Inorg. Chem*. **1988**, *27*, 2781.

(30) Martin, K. J.; Squattrito, P. J.; Clearfield, A. *Inorg. Chimica Acta* **1989**, *155*, 7.

(31) Subramanian, L.; Hoffmann, R. *Inorg. Chem.* **1992**, *31*, 1021.

(32) Didziulis, S. V.; Cohen, S. L.; Butcher, K. D.; Solomon, E. I. *Inorg. Chem.* **1988**, *27*, 2238.

(33) Burdett, J. K.; Eisenstein, O. *Inorg. Chem.* **1992**, *31*, 1758.

(34) Harman, W. D. *Chem. Rev.*, **1997**, *97*, 1953.

(35) Hakansson, M.; Jagner, S.; Walter, D. *Organometallics* **1991**, *10*, 1317.

(36) Hakansson, M.; Jagner, S.; Clot, E.; Eisenstein, O. *Inorg. Chem.* **1992**, *31*, 5389.

(37) Semmelhack, M. F. *Comprehensive Organic Synthesis*; Trost, B. M., Ed.; Pergamon Press: Oxford, 1990; vol. 4, p. 517.

Chapter 5:

Reactivity Studies on the Aromatic and Olefin Binding by Copper(I)-Ziconium(IV) Chloride Materials

Abstract

The solvothermal reaction of Cu_2ZrCl_6 and $ZrCl_4$ in benzene is shown to yield the molecular species $((bz)_2Cu)_2Zr_2Cl_{10}$•bz (**1**), which is characterized by single crystal X-ray diffraction with **a** = 21.144(2) Å, **b** = 7.4987(5) Å, **c** = 24.170(2) Å, and β = 90.365(6)° in the monoclinic space group I2/a (no. 15). The benzene is lost from this material in a stepwise fashion resulting in what are described to be a chain, $((bz)Cu)_2Zr_2Cl_{10}$ (**2**), and a layered clay-type material, $Cu_2Zr_2Cl_{10}$ (**3**). The desolvated material, **2**, is also luminescent and both **2** and **3** exhibit reversible binding of ethylene, which is characterized by *in situ* time-resolved X-ray diffraction and diffuse reflectance measurements. The reversible ethylene binding in these metal-halide complexes is reminiscent of clay-type behavior, and is shown to be dependent upon the Lewis acid strength of the metal bound to Cu(I), where the strongest Lewis acid yields the greatest ethylene binding.

5.1. Introduction

The reactivity and coordination flexibility of Cu^{I} has led us to initiate studies in which $(CuCl_4)^{3-}$ tetrahedra are constructed along with other Lewis acidic metals into open-framework, metal-halide materials.[1] The coordination of Lewis acids is anticipated to increase the reactivity of the active copper site. And, the coordinative flexibility of Cu^{I} should favor binding/activation/release of substrates as necessary in a catalytic cycle. To access the reactivity of such metal-halide solids, open framework metal-halides materials have recently been synthesized based on an analogy to silicates,[2] whereby halides are substituted for chalcogenides.[1] For example, the structures of α- and β-$CuAlCl_4$ exhibit a three-dimensional network of corner sharing tetrahedra that can be described as the charged matched analogs of the aluminophosphate $AlPO_4$.[4,5] The combination of Lewis acids, like Al^{3+}, with $[CuCl_4]^{3-}$ tetrahedra has a dramatic effect on the reactivity of copper(I) halides. CuCl by itself binds ethylene only at low temperature (0°C) and high pressures (>60 atm C_2H_4).[3] Studies performed in our laboratory have shown that copper (I) in the presence of Al^{3+} in $CuAlCl_4$ can reversibly bind and/or form stable complexes with ethylene[4,5] at room temperature under low pressures (ca. 100 torr) of ethylene. This chemical reactivity is a function of the Lewis acidic metal-halide building blocks, as well as a remarkable framework flexibility. In a similar example, Cu^{+} in the presence of $[BF_4]^{-}$ has been incorporated into a polymer, and used in the separation of olefin/paraffin gas mixtures,[6] which is an important process in the petrochemical industry.[7]

Although crystalline $CuAlCl_4$ reversibly binds ethylene, its parent structure exhibits a condensed network that requires a significant distortion of the framework and the breakage of covalent bonds to accommodate ethylene. In order to prepare new metal-

halide materials with an enhanced sorption capability greater than that observed for $CuAlCl_4$, I have sought to prepare materials that have a more open structure, such as metal-halide analogs of silicate-based clays. Silicate-based clays, such as kaolinite and montmorillonite, are constructed from a two-dimensional covalent network of octahedral and tetrahedral building blocks of silicate and/or aluminate. The reaction space between these layers gives clay-type materials very high surface areas making them powerful sorbants and active catalysts. Upon sorption/desorption of small molecules this interlayer space can expand or contract without disrupting the covalent network. To prepare metal-halide materials with clay-type architectures, I have incorporated Lewis acidic cations that prefer an octahedral coordination of halides, such as zirconium (IV), along with the tetrahedral cuprous chloride. In the previous chapter, I showed the utility of copper(I)-zirconium(IV) materials for binding aromatic molecules, like benzene, with the preparation of $((bz)CuCl_3)_2Zr$ from the solvothermal reaction of Cu_2ZrCl_6 in benzene. In this chapter, I describe the addition of $ZrCl_4$ to the solvothermal reaction of Cu_2ZrCl_6 in benzene to yield the molecular species $((bz)_2Cu)_2Zr_2Cl_{10}$•bz (**1**). The benzene is lost from this material in a stepwise fashion resulting in what I argue is a chain, $((bz)Cu)_2Zr_2Cl_{10}$ (**2**), and a layered clay-type material, $Cu_2Zr_2Cl_{10}$ (**3**). The desolvated material, **2**, is also luminescent and both **2** and **3** exhibit reversible binding of ethylene, which is characterized by *in situ* time-resolved X-ray diffraction and diffuse reflectance measurements. The ethylene binding of the copper-zirconium materials is compared to that observed for the $CuMCl_4$ materials (where M = Al or Ga), as well as other copper(I)-amine materials that are known to form stable ethylene adducts.

5.2. Experimental

General Procedures. All reactions were performed under an inert atmosphere of dry N_2 in a glove box or using Schlenk line techniques. $ZrCl_4$ (99.99%) was used as received from Aldrich. The CuCl was prepared from Cu metal and $CuCl_2$ (Aldrich) according to literature methods and further purified by sublimation.[8] The syntheses of $CuMCl_4$ (M = Ga, Al) and Cu_2ZrCl_6 are reported elsewhere.[4,9] Benzene (99.9%, Fisher) was distilled from Na/benzophenone, then stored under nitrogen over molecular sieves (4Å). Elemental analyses were performed by Atlantic Microlab, Inc.

Preparation of $((C_6H_6)_2Cu)_2Zr_2Cl_{10}\cdot C_6H_6$ (1). Cu_2ZrCl_6 (0.100 g, 0.232 mmols) and $ZrCl_4$ (0.0540 g, 0.232 mmols) were weighed out, ground together in a mortar and pestle, and transferred to a thick walled fused silica tube (10mm O.D. × 6mm I.D). On a Schlenk line, 1.0 ml of benzene was added to the reaction vessel. The reaction mixture was frozen with liquid N_2 and sealed using a torch such that the fused silica vessel was filled to 25% volume. The reaction mixture was heated to 125°C for one week then slow cooled at a rate of 0.05°C/min. (*Note of Caution: upon heating the sealed reaction vessel significant pressures are generated which can lead to vessel rupture. Appropriate shielding should be utilized such as placing the reaction vessels in a capped iron pipe during heating.)* Upon standing at room temperature colorless crystals of **1** grew over the next two days from which a single crystal was isolated for an X-ray structure determination. The crystalline material rapidly looses solvent when removed from the benzene yielding a pale, yellow powder, $((C_6H_6)Cu)_2Zr_2Cl_{10}$ (**2**).

Preparation of $((C_6H_6)Cu)_2Zr_2Cl_{10}$ (2). Bulk quantities of $((C_6H_6)Cu)_2Zr_2Cl_{10}$ (**2**) were prepared by transferring a ground sample of Cu_2ZrCl_6 (1.00 g, 2.32 mmols),

$ZrCl_4$ (0.541 g, 2.32 mmols), and magnetic stir bar to a 100ml Schlenk flask (14/20), which was fitted with a rubber septum. Benzene (30 ml) was then added to the reaction mixture, which was then heated to reflux with stirring under a passive flow of N_2 for 15 hours. An unknown phase and unreacted starting material, approximately 50%, did not dissolve and were separated from the colorless solution of **1** using a medium porosity glass frit. The benzene of the supernatant was then removed *in vacuo* to give **2**. The overall yield was optimized to ~50% (based on an initial loading) by stimulating the crystallization of **1** from the supernatant by shock exposure to liquid N_2 or a dry ice acetone bath prior to removal of the benzene solvent. The product, **1**, was quantitatively converted to **2** by the *in vacuo* removal of the solvent. An elemental analyses of the resulting solid was consistent with the formula $((C_6H_6)Cu)_2Zr_2Cl_{10}$ (**2**). Elemental analysis observed for $((C_6H_6)Cu)_2Zr_2Cl_{10}$, C: 16.96% and H: 1.70%; calculated, C: 17.56% and H 1.48%. The remaining benzene is lost slowly under a nitrogen atmosphere over a period of weeks or it can be removed under reduced pressure for several hours yielding a yellow solid, $Cu_2Zr_2Cl_{10}$(**3**). However, **2** can be stored in a capped vial, which significantly reduces the amount of benzene loss.

$((C_2H_4)Cu)_2Zr_2Cl_{10}$. A sample of **2** (300 mg) was placed in a Pyrex holder affixed to a gas line. The reaction tube was evacuated to ca. 10 mtorr then exposed to 1500 torr of ethylene for 3 hours. Elemental analysis of the product is consistent with the displacement of the benzene by ethylene to give the formula $((C_2H_4)Cu)_2Zr_2Cl_{10}$(**4**). Elemental analysis observed for $((C_2H_4)Cu)_2Zr_2Cl_{10}$ found: C = 6.04% and H = 1.51%, calculated C = 6.66% and H = 1.11%. As was the case for the benzene-coordinated

material, the ethylene is slowly lost over the period of weeks. However, desorption can be almost negated by placing the sample in a capped vial.

X-ray structure determination of $((C_6H_6)_2Cu)_2Zr_2Cl_{10}\cdot C_6H_6$ (1). Under a flow of argon a single crystal (0.3 x 0.2 x 0.14 mm) covered in silicone grease was mounted on the end of a glass fiber, and immediately transferred to the diffractometer where it was cooled to -116°C under a stream of dry nitrogen. Data were then collected on an Enraf-Nonius CAD4-Mach diffractometer with monochromated Mo(Kα) radiation. Lattice constants were determined by a symmetry-constrained fit of 24 well centered reflections between $32°<2\theta<36°$ and their Friedel pairs. A unique quadrant, h, ±k, l, was collected with 4144 independent reflections by ω-scans with $0°<2\theta<54°$. The data were scaled to three intensity check reflections using a five point smoothing routine. An empirical absorption correction was applied using psi scan data.

Systematic absences were found to be consistent with the space group I 2/a, which was confirmed in the subsequent refinement. The structure was refined using the NRCVAX suite of programs. [10] All non-hydrogen atoms were located by direct methods using the SIR92 program[11] and refined anisotropically in the final refinement. Hydrogen atoms bound to the benzene rings were then added in calculated positions (idealized to C-H=0.96 Å) and assigned fixed temperature factors. A full matrix least squares calculation using the 2989 unique reflections ($I > 1.0\ \sigma(I)$) gave a final refinement with R factors of $R = 0.058$ and $R_w = 0.060$.

Volumetric Gas Sorption Measurements. A stainless steel volumetric gas line was constructed using ¼" tubing and Swage Lok© connectors. Manual Nupro valves (model SS-4B8) were used to control the atmosphere of the line, either under vacuum,

N_2, or C_2H_4. The pressure of the system was measured with a Varian WV-100-2 pressure gauge that employed a pirani sensor (1 mtorr to 2 torr) and a diaphragm manometer (1 torr to 1500 torr, +/- 1%). Powdered samples were dispersed across the 7.1 cm^2 base of a ~16.0 mL Pyrex sample holder, which was closed by a threaded chlorotrifluorethylene (CTFE) stop-cock. The dead-volume of the sample holder was calculated before each experiment using N_2 based on the volume of the gas line and the ideal gas law. The sample holder was connected to the gas line by o-ring joints (#7) and a screw clamp. Before sorption measurements were conducted, the entire system was opened to vacuum (10 mtorr). The calibrated section of the gas line and sample holder was then separately closed to vacuum. The calibrated section was filled with a predetermined dosing pressure, then the valve to the sample holder was opened to introduce the dosing gas to the sample.

In a typical sorption experiment ($((C_6H_6)Cu)_2Zr_2Cl_{10}$ (**2**) (0.0263 g, 0.0320 mmols) was weighed out in the sample holder, which was just enough to cover the sample holder base. The sample was exposed to ethylene in 100 torr increments from 0 to 1500 torr. Equilibration times of one hour were used before final pressure readings were recorded. The amount of gas sorbed was determined using the difference in the pressure before and after exposing the sample to ethylene and the ideal gas law. Greater than 99.9% of the gas was sorbed within the first five minutes after exposure. Therefore, subsequent experiments, including the spectroscopic investigations described below, were performed with ten-minute equilibration times. Similar ethylene sorption experiments were performed with $CuAlCl_4$ and $CuGaCl_4$, as well.

Spectroscopy. *In situ* Diffuse Reflectance Spectra (DRS) were taken using a Cary 3e UV-vis spectrometer equipped with an integrating sphere. Spectra were measured with respect to a pressed polytetrafluoroethylene (Teflon) powder standard. Reflectance spectra were collected as $R_\infty = R_{sample}/R_{reference}$, then plotted as the remission function, $F(R_\infty) = (1 - R_\infty)^2/2\ R_\infty$, based on the Kubelka-Munk theory of diffuse reflectance.[12] A quartz diffuse reflectance cell ($1.0 \times 10 \times 40$ mm) was fused to a quartz-to-Pyrex connector, which was attached to a 90°-high vacuum valve (chemglass) fitted with a glass o-ring joint (#7) on the side arm and closed off by a threaded CTFE stop cock (ethylene propylene o-ring). Gas was introduced to the sample *via* a line constructed from ¼" stainless-steel tubing and valves (Nupro 4-BK series), which were connected by VCR fittings and gaskets. A piece of CAJON stainless-steel, flexible tubing (¼") with two metal/glass ends was modified with a glass o-ring joint to connect to the sample holder, and a glass/metal transition tube to connect to the gas line. The gas pressure was monitored from 1×10^{-3} to 760 torr using a Varian Ba2C SenTorr Gauge Controller and a ConvecTorr vacuum tube gauge transducer. Pressures greater than 760 torr were controlled using the regulator attached directly to the gas tank. The sample holder was connected to the gas line by o-ring joints (#7) and a screw clamp. Before the sample was exposed to the dosing gas, the entire system was evacuated to 1 mtorr. The gas line and sample holder were then separately closed to vacuum. The line was filled with a predetermined pressure of dosing gas, then the valve to the sample holder opened to expose the dosing gas to the sample.

In a typical experiment $((C_6H_6)Cu)_2Zr_2Cl_{10}$ (**2**) (0.200 g, 0.243 mmols) was diluted into 2.0 g of fused silica (ground and passed through 60 mesh (0.1mm) sieve and dried at 160°C for at least 24 hrs.) and ground together in a mortar and pestle. A portion of that mixture was then used to completely fill the quartz sample holder. The sample was dosed with ethylene, and diffuse reflectance spectra were recorded at 100 torr intervals up to 1500 torr. Spectra were recorded after approximately ten minutes of equilibration at each pressure. The sample was then exposed to vacuum and the ethylene was removed under reduced pressure. Spectra were recorded periodically during the first hour of desorption. Sorption and desorption experiments were also performed with $Cu_2Zr_2Cl_{10}$ (**3**) diluted in ground quartz. In this case the sample was exposed to 1500 – 1800 torr of ethylene and the sorption monitored periodically by DRS.

Steady-state fluorescence spectra were measured with an ISS PC-1 fluorometer equipped with a Xenon arc lamp using a front face detection geometry to orient the sample face at an angle of 22.5° with respect to the incident beam. A low band-pass UG-11 filter was placed after the excitation monochromator. Excitation spectra were correct with respect to a standard quinine sulfate solution and the NIST spectrum. Emission spectra were plotted using the relative emitted energy per constant interval ($\Phi_E = \Phi_\lambda \lambda^2/hc$).[13]

Time Resolved Powder X-ray Diffraction (TRXRD). TRXRD experiments were performed at the X7B beamline of the National Synchrotron Light Source at Brookhaven National Laboratories. This beamline was equipped with the MAR345-camera and an image plate detector.[41] The wavelength (λ = 0.9388), sample to detector distance, tilting angle of the IP and zero shift position of the IP for the data collection

were determined using full Debeye-Scherrer rings of LaB_6. Data reduction of the full rings was done using Fit2d.[14,15] Samples were held in 0.7 mm fused silica capillaries, mounted on a goniometer head for positioning in the beam. A Swagelok© T was mounted on the goniometer head and the sample capillary (opened at one end) was secured with a ferrule and screw cap arrangement. The gas line/vacuum was similarly secured to the side of the T.[16] A sample of **2** was exposed to ethylene in 100 torr increments up to 1500 torr C_2H_4 at room temperature. Ten minutes elapsed from the time of the exposure before a diffractogram was taken.

Another ethylene sorption experiment at X7B utilized a translating image plate (TIP) camera mounted on a four circle Huber diffractometer in a Debeye-Scherrer collection geometry.[17] Image plates (20x40 cm Fuji type IP) were scanned using a Fuji BAS2000 scanner.[18] The wavelength (λ = 0.937005), sample to detector distance, tilting angle of the IP and zero shift position of the IP for the data collection were again determined using full Debeye-Scherrer rings of LaB_6. Data reduction for the TIP plates was done using software written by Paul Norby for X7B.[17] The sample was rotated 60° about an axis perpendicular to the beam at a rate of approximately 1° per second during which time the image plate was stepped across the beam from behind a slit to yield a time resolved diffraction pattern. In this experiment, the precipitate from the initial reaction mixture for the preparation of **1,** containing a mixture of an as yet unidentified CuZrCl material and excess CuCl, were exposed to ethylene.

Table 5.1. Crystallographic data for $((C_6H_6)_2Cu)_2Zr_2Cl_{10}\cdot C_6H_6$(**1**) at –116°C.

Formula	$((C_6H_6)_2Cu)_2Zr_2Cl_{10}\cdot C_6H_6$
Formula weight(g/mol)	1054.62
Crystal dimensions (mm)	0.3 x 0.2 x 0.14
Crystal class	Monoclinic
Space Group (No.)	I2/a (15)
a (Å)	21.144(2)
b (Å)	7.4987(5)
c (Å)	24.170(2)
β, °	90.365(6)
V (Å^3)	3832.3(5)
Number of Reflection for final unit cell	24
Min and Max 2theta values for final cell	32°, 36°
Z	4
F(000)	2057.44
ρ_{calcd} (mg cm^{-3})	1.828
λ(Mo K_α), Å	0.71073
μ (cm^{-1})	23.4
temp. (°C)	-116
Diffractometer	Enraf-Nonius CAD4 Mach
Data Collection	omega scan
Max 2θ	54.0
Number of Reflections measured	4145
Unique Reflections measured	4144
R-merge	0.007
min and max transmission	0.7285, 0.9968
Number of reflection in refinement	2989
Cut off Threshold	Inet > 1.0σ(I)
Structure refined using full matrix least squares	
Structure refined with weights based on counting statistics	
Weighting Scheme modifier, k	0.0005
Number of parameters in least-Squares	200
R[a]	0.058
R_w[b]	0.060
GOF[c]	1.56
Maximum shift/error	0.00
min and max peak heights on final DF map (e$^-$/Å^3)	-2.00, 1.42

[a]$R_f = (\Sigma(F_0 - F_c)/F_0)$. [b]$R_w = [\Sigma(w(F_0 - F_c)^2)/ wF_0^2)]^{½}$.
[c]$GOF = [\Sigma(w(F_0 - F_c)^2)/(\text{No. of reflns. - No. of parameters})]^{½}$

Table 5.2. Atomic positions for $((C_6H_6)_2Cu)_2Zr_2Cl_{10}\cdot C_6H_6$(**1**) at –116°C.

	x	y	z	B_{iso}
Zr(1)	0.3227(1)	0.19465(9)	0.9473(1)	0.87(2)
Cu	0.3663(1)	0.1032(1)	0.1191(1)	1.95(4)
Cl(1)	¼	0.4170(3)	1	1.09(9)
Cl(2)	¼	0.9774(3)	1	0.97(8)
Cl(3)	0.3930(1)	0.2010(3)	0.0289(1)	1.29(6)
Cl(4)	0.2418(1)	0.2038(3)	0.8728(1)	1.40(6)
Cl(5)	0.3800(1)	0.4317(3)	0.9063(1)	1.53(6)
Cl(6)	0.3739(1)	0.9443(3)	0.9090(1)	1.62(7)
C(1)	0.0909(6)	0.346(1)	0.8290(5)	3.9(5)
C(2)	0.1087(4)	0.276(1)	0.7779(5)	4.1(5)
C(3)	0.0625(5)	0.192(1)	0.7452(3)	3.2(4)
C(4)	0.0029(5)	0.180(1)	0.7639(4)	2.9(4)
C(5)	0.9866(4)	0.249(1)	0.8137(4)	3.0(4)
C(6)	0.0307(6)	0.333(1)	0.8458(3)	3.6(5)
C(7)	0.4221(4)	0.864(1)	0.1457(3)	1.8(3)
C(8)	0.3581(3)	0.814(1)	0.1400(3)	1.4(3)
C(9)	0.3394(3)	0.731(1)	0.0909(3)	1.5(3)
C(10)	0.3818(4)	0.700(1)	0.0499(3)	1.9(3)
C(11)	0.4441(4)	0.747(1)	0.0554(4)	2.2(3)
C(12)	0.4642(4)	0.833(1)	0.1039(4)	2.4(4)
C(13)	0.2929(3)	0.812(1)	0.2894(3)	1.8(3)
C(14)	0.2513(4)	0.929(1)	0.2631(3)	1.7(3)
C(15)	0.2918(3)	0.633(1)	0.2767(3)	1.6(3)

Table 5.3. Selected bond distances(Å) and angles(°) for $((C_6H_6)_2Cu)_2Zr_2Cl_{10}\cdot C_6H_6$(**1**) at –116°C.

Zr(1)-Zr(1)	4.007(1)	C(1)-C(2)	1.39(2)
Zr(1)-Cl(1)	2.607(2)	C(1)-C(6)	1.34(2)
Zr(1)-Cl(2)	2.582(2)	C(2)-C(3)	1.40(2)
Zr(1)-Cl(3)	2.463(2)	C(3)-C(4)	1.35(2)
Zr(1)-Cl(4)	2.475(2)	C(4)-C(5)	1.35(1)
Zr(1)-Cl(5)	2.371(2)	C(5)-C(6)	1.37(2)
Zr(1)-Cl(6)	2.358(2)		
		C(7)-C(8)	1.41(1)
Cu-Cl(3)	2.372(2)	C(7)-C(12)	1.37(1)
Cu-Cl(4)	2.417(2)	C(8)-C(9)	1.40(1)
		C(9)-C(10)	1.36(1)
Cu-C(1)	2.385(8)	C(10)-C(11)	1.37(1)
Cu-C(2)	2.85(1)	C(11)-C(12)	1.40(1)
Cu-C(7)	2.237(7)	C(13)-C(14)	1.39(1)
Cu-C(8)	2.235(8)	C(13)-C(15)	1.38(1)
		C(14)-C(15)	1.40(1)
		C(15)-C(14)	1.40(1)
Cl(1)-Zr(1)-Cl(2)	78.89(6)	Zr(1)-Cl(3)-Cu	125.79(7)
Cl(1)-Zr(1)-Cl(3)	87.16(5)	Zr(1)-Cl(4)-Cu	125.61(7)
Cl(1)-Zr(1)-Cl(4)	86.04(5)	C(2)-C(1)-C(6)	120.2(8)
Cl(1)-Zr(1)-Cl(5)	91.68(7)	C(1)-C(2)-C(3)	118.5(8)
Cl(1)-Zr(1)-Cl(6)	167.01(7)	C(2)-C(3)-C(4)	119.5(8)
Cl(2)-Zr(1)-Cl(3)	88.54(4)	C(3)-C(4)-C(5)	121.2(8)
Cl(2)-Zr(1)-Cl(4)	88.03(5)	C(4)-C(5)-C(6)	120.2(8)
Cl(2)-Zr(1)-Cl(5)	170.57(7)	C(1)-C(6)-C(5)	120.4(8)
Cl(2)-Zr(1)-Cl(6)	88.13(7)	C(8)-C(7)-C(12)	120.7(7)
Cl(3)-Zr(1)-Cl(4)	172.87(6)	C(7)-C(8)-C(9)	117.9(6)
Cl(3)-Zr(1)-Cl(5)	90.74(6)	C(8)-C(9)-C(10)	120.7(7)
Cl(3)-Zr(1)-Cl(6)	93.05(7)	C(9)-C(10)-C(11)	121.6(7)
Cl(4)-Zr(1)-Cl(5)	91.62(6)	C(10)-C(11)-C(12)	119.1(7)
Cl(4)-Zr(1)-Cl(6)	93.08(7)	C(7)-C(12)-C(11)	119.9(7)
Cl(5)-Zr(1)-Cl(6)	101.30(7)	C(14)-C(13)-C(15)	120.3(7)
Cl(3)-Cu-Cl(4)	102.01(7)	C(13)-C(14)-C(15)	120.6(7)
Zr(1)-Cl(1)-Zr(1)	100.45(8)	C(13)-C(15)-C(14)	119.1(7)
Zr(1)-Cl(2)-Zr(1)	101.77(9)		

5.3. Results

Structure of $((bz)_2Cu)_2Zr_2Cl_{10}\cdot(bz)$ (1). A summary of crystallographic data for $((bz)_2Cu)_2Zr_2Cl_{10}\cdot(bz)$ (**1**) is given in Table 5.1, positional parameters are listed in Table 5.2, and selected bond distances and angles are reported in Table 5.3. An ORTEP drawing of the $((bz)_2Cu)_2Zr_2Cl_{10}$ molecule, **1**, is shown in Figure 5.1 and a crystal packing view of the unit cell looking down **b** is given in Figure 5.2. This molecule consists of an edged-shared zirconium bioctahedron with two chloride bridges between zirconium atoms, Zr(1)-Cl(1) = 2.607(2) Å and Zr(1)-Cl(2) = 2.582(2) Å, and four terminal Zr-Cl bonds, Zr(1)-Cl(5) = 2.371(2) Å × 2 and Zr(1)-Cl(6) = 2.358(2) Å × 2, in the equatorial plane. The axial chlorides, Cl(3) and Cl(4), on each side of the bioctahedron, Zr(1)-Cl(3) = 2.463(2) Å and Zr(1)-Cl(4) 2.475(2) Å, form bridges to a Cu(I) cation, Cu-Cl(3) 2.372(2) Å and Cu-Cl(4) = 2.417(2) Å, such that a boat-like geometry is observed for the $Cu_2Zr_2Cl_4$ tetrameric ring. The boat-like configuration, highlighted in Figure 5.1, is observed with the two copper atoms coordinated in a *cis*-conformation with respect to the axial plane of the bioctahedron. The Cl(3)-Cu-Cl(4) plane is bent ca. 31° out of the Cl(3)-Zr'-Cl(4)'-Cl(3)'-Zr-Cl(4) molecular plane resulting in a Cu-Cu separation of 7.55 Å. The coordination sphere of the copper cations is completed with two equivalents of benzene. Each copper atom is bound to one benzene molecule in an η^2-fashion, Cu-C(7) = 2.237(7) Å and Cu-C(8) = 2.235(8) Å, while a second benzene molecule is weakly coordinated in an η^1-fashion with a Cu-C(1) = 2.385(8) Å. The next nearest carbon atoms are C(2), 2.85(1), and C(6), 2.90(1) Å. The coordination to Cu(I) does not dramatically distort the C-C bond distances in the benzene

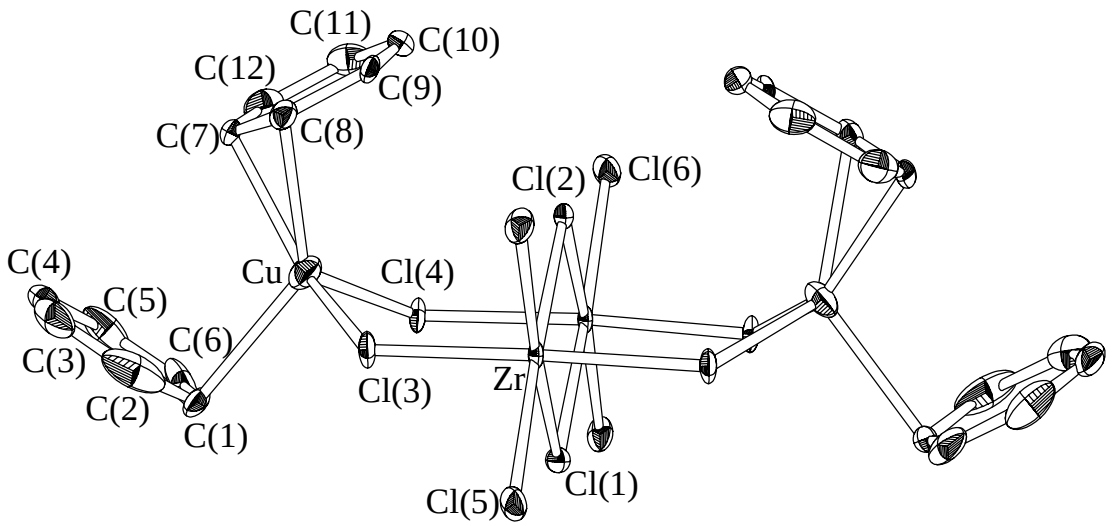

Figure 5.1. ORTEP drawing of the molecules in $((bz)_2Cu)_2Zr_2Cl_{10}\cdot(bz)$ (**1**). Thermal ellipsoids are shown at the 50% confidence level.

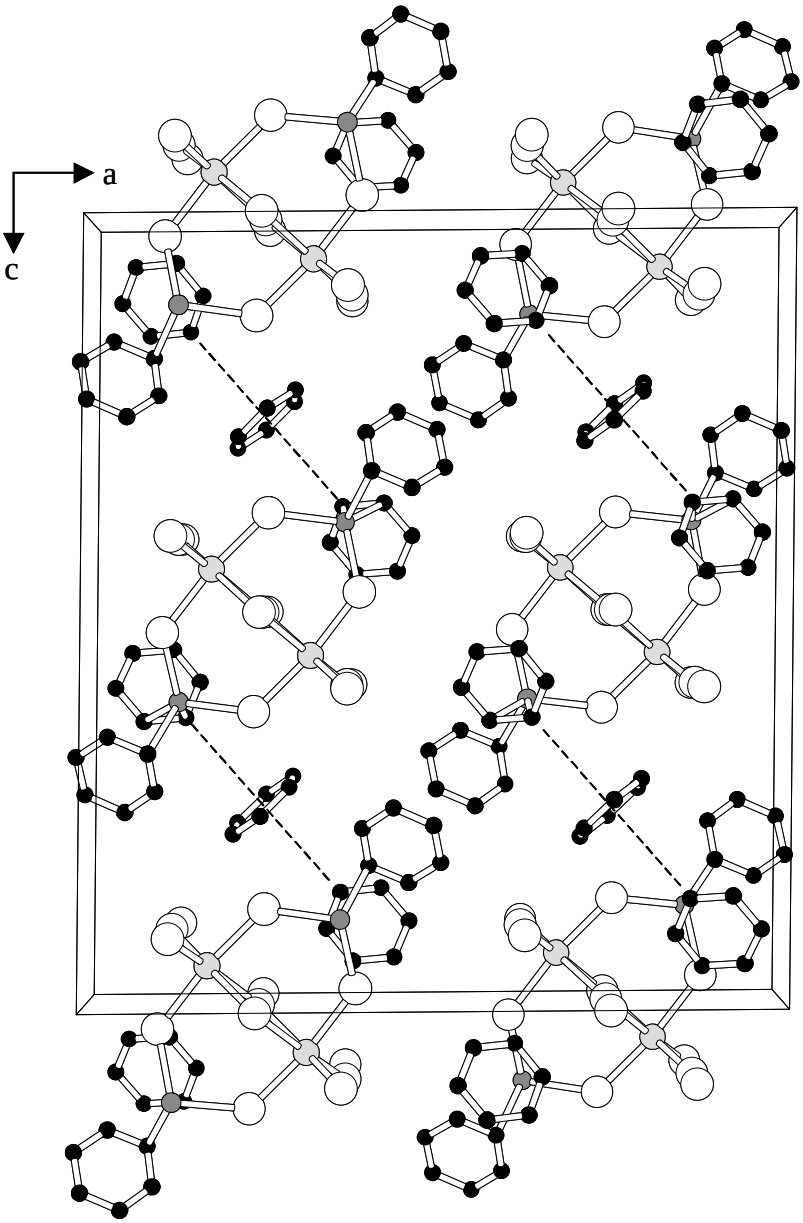

Figure 5.2. Ball and stick drawing of the molecules filling the unit cell in $((bz)_2Cu)_2Zr_2Cl_{10}\cdot(bz)$ (**1**) viewed down the **b**-axis. Unfilled spheres are Cl, smaller, gray spheres are Cu, larger, gray spheres are Zr, and black ball represent carbon. Dashed lines indicate the shortest edge-face π-stacking contacts between the coordinated and solvated benzene molecules.

ligands. However, the longest C-C contact is observed for the C(7)-C(8) bond, 1.41(1) Å, which also corresponds to the site of the η^2-coordination. Greater variation between C-C bond distances is observed for both types of coordinated benzene ligands, 1.35(1) to 1.41(1) Å (Δ = 0.06 Å), compared to the lattice solvated molecule, 1.38(1) to 1.40(1) Å (Δ = 0.02 Å); presumably a result of charge transfer upon coordination to the Cu^+. Furthermore, the thermal parameters are notably larger for the carbon atoms of the η^1-bound benzene ligand consistent with its weaker coordination as opposed to the η^2-coordination and the strong hydrogen bonding of the solvated benzene molecules.

The unusual boat-like geometry for this tetrameric complex is a result of strong π-stacking interactions with the coordinated benzene ligands and hydrogen bonding between the terminal halides and the edge of the coordinated and lattice solvated benzene rings. These contacts are described in Table 5.4. The solvated benzene forms edge-to-face π-stacking with the η^2-bound benzene ligands, which connect adjacent molecules along the **a**-direction. The distances from the midpoint of the face of the solvated benzene, B_s, to the edge of the η^2-bound benzene, 3.55 Å to C(8), 4.52 Å to C(7) and 4.30 Å to C(9), are similar to the edge-to-face π-interactions observed in the crystal structure of benzene, 3.6 Å.[19,20] Both of the coordinated benzene molecules are also involved in intermolecular edge-to-face π-type interactions along the **b** and **c**-directions yielding a three-dimensional π-stacked lattice. Significant intramolecular edge-to-face π-interactions are observed from the midpoint of the η^1-bound benzene, B_1, to the edge of the η^2-bound benzene, 3.36 Å to C(7), 4.21 Å to C(8), and 4.03 Å to C(12). And, intermolecular interactions are found between the η^1-bound benzene ligands of adjacent

Table 5.4. Hydrogen bonded and edge-to-face π-interactions in $((C_6H_6)_2Cu)_2Zr_2Cl_{10}\cdot C_6H_6$(**1**) at –116°C.

	B_s	B_1	B_2	Cl(2)	Cl(3)	Cl(4)	Cl(5)	Cl(6)
η^1-bz								
C(1)			3.67			3.52		
C(3)		4.09						
C(4)		3.61	4.51					
C(5)		4.55					3.99	
C(6)			3.86				3.93	4.21
η^2-bz								
C(7)	4.52	3.36 4.55						3.63
C(8)	3.55	4.21		4.25		3.62		
C(9)	4.30			3.43		4.04		
C(10)				3.67			3.89	
C(11)					3.63		4.10	
C(12)		4.03			3.63	3.66	3.85	3.82
bz-solvate								
C(13)							3.88	3.86
C(14)					3.88			
C(15								3.68

molecules, 3.61 Å to C(4), and 4.09 Å to C(3). Only a few, relatively long, intermolecular interactions are found from the midpoint of the η^2-bound benzene, B_2, to neighboring benzene molecules, C(1), 3.67 Å, C(6), 3.86 Å, and C(4), 4.51 Å.

In addition to the edge-to-face π-type interactions that hold the molecules together, significant hydrogen bonding between the chloride ligands and the edges of the coordinated benzene ligands also contribute to the lattice stabilization, as well as the unusual geometry of the molecule. Hydrogen bonding interactions are found between the edges of the benzene solvate and the terminal chlorides, C(13) – Cl(5) = 3.88, Cl(13) – Cl(6) = 3.86, and C(15) – Cl(6) = 3.68, which help to stabilize the overall lattice. In addition, intramolecular hydrogen bonding contacts between chlorides and carbons of coordinated benzene ligands, Cl(2)-C(9) = 3.43 Å, Cl(2)-C(10), 3.67 Å, Cl(6)-C(10), 3.89 Å, and Cl(6)-C(11) = 4.10 Å, appear to pull the benzene ligands towards the equatorial plane of the zirconium bioctahedron. Intermolecular chloride-benzene hydrogen bonded contacts between tetramers are also present to both the η^2-bound benzene, C(12)-Cl(6) = 3.82 Å, Cl(12)-Cl(5) = 3.85 Å, C(7)-Cl(6) = 3.63 Å, and to the η^1-bound benzene, C(6)-Cl(5) = 3.93 Å and C(5)-Cl(5) = 3.99 Å, which help to stabilize the overall packing of molecules in the lattice. No close contacts between chlorides and the solvated benzene are observed.

Excitation and Emission Spectroscopy. The partially desolvated material $((bz)Cu)_2Zr_2Cl_{10}$ (**2**) exhibits a brilliant yellow photoluminesence under UV excitation. The excitation and emission maxima for **2**, shown in Figure 5.3, were observed at 26,110 cm^{-1} (383 nm) and 17,390 cm^{-1} (575 nm), respectively. The yellow emission was also readily observed under the long wavelength excitation of a hand held mercury lamp (350

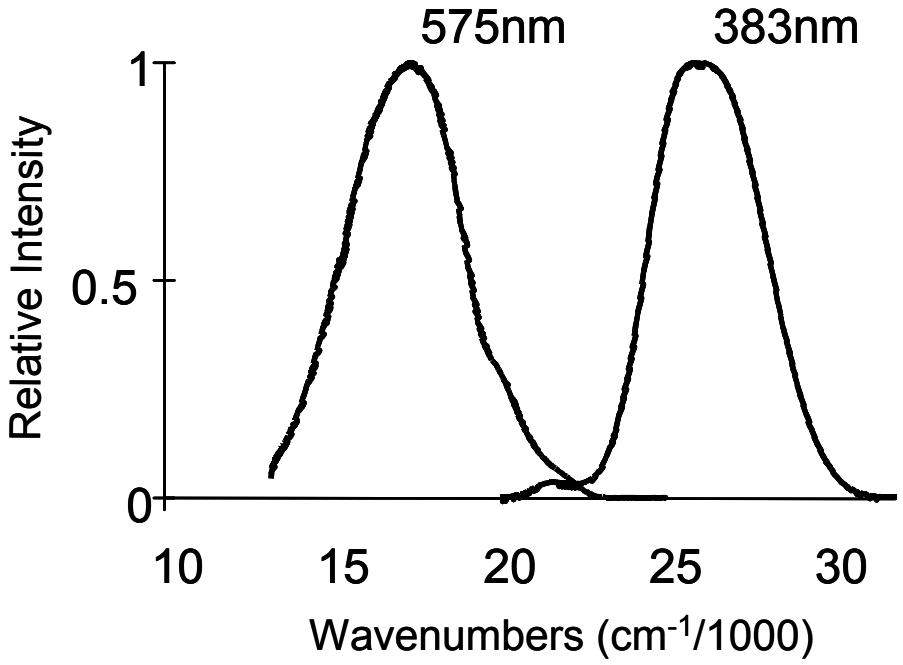

Figure 5.3. Excitation and emission spectra for $((bz)Cu)_2Zr_2Cl_{10}$ (**2**).

nm) under daylight conditions, and was found to be approximately 25% the intensity of anthracene.[21] Desorption of the benzene from **2** to form **3** results in a loss of the observed luminescence.

Gas Sorption by $((bz)Cu)_2Zr_2Cl_{10}$ (2)

Volumetric Gas Sorption Studies. In order to ascertain if the benzene coordinated to $((bz)Cu)_2Zr_2Cl_{10}$ (**2**) could be displaced by another neutral, two electron donor, like ethylene, and/or exhibit clay-type sorption, volumetric gas sorption/desorption studies were undertaken and are summarized in Figure 5.4. Because the loss of coordinated benzene results in the loss of the observed luminescence of **2**, all samples were checked for yellow luminescence using a hand held mercury lamp (350 nm) before beginning any experiments, and after the sample holder was evacuated. Luminescence was observed throughout the evacuation process, which indicated that a significant fraction of the benzene was still coordinated to the sample before the addition of ethylene. Furthermore, the vapor pressure of benzene is low at room temperature with respect to the ethylene. Thus, as the benzene is displaced by ethylene, it does not significantly contribute to the measured gas pressure in the line. Ethylene was then added to $((bz)Cu)_2Zr_2Cl_{10}$ (**2**) in 100 torr increments up to 1500 torr and allowed to equilibrate for at least one hour between initial and final pressure readings. A plateau during the initial sorption is observed at ca. 400 torr with 0.5 eqs. of C_2H_4 sorbed per copper site (**4**). After the initial plateau the sample steadily sorbs increasing amounts of ethylene up to 1.4 eqs. per copper site at 1500 torr. Upon desorption the one equivalent/copper adduct is observed to persist down to quite low pressures of ethylene, such that this 1:1 C_2H_4:Cu^+ adduct (**5**) is reasonably isolable. The final equivalent of

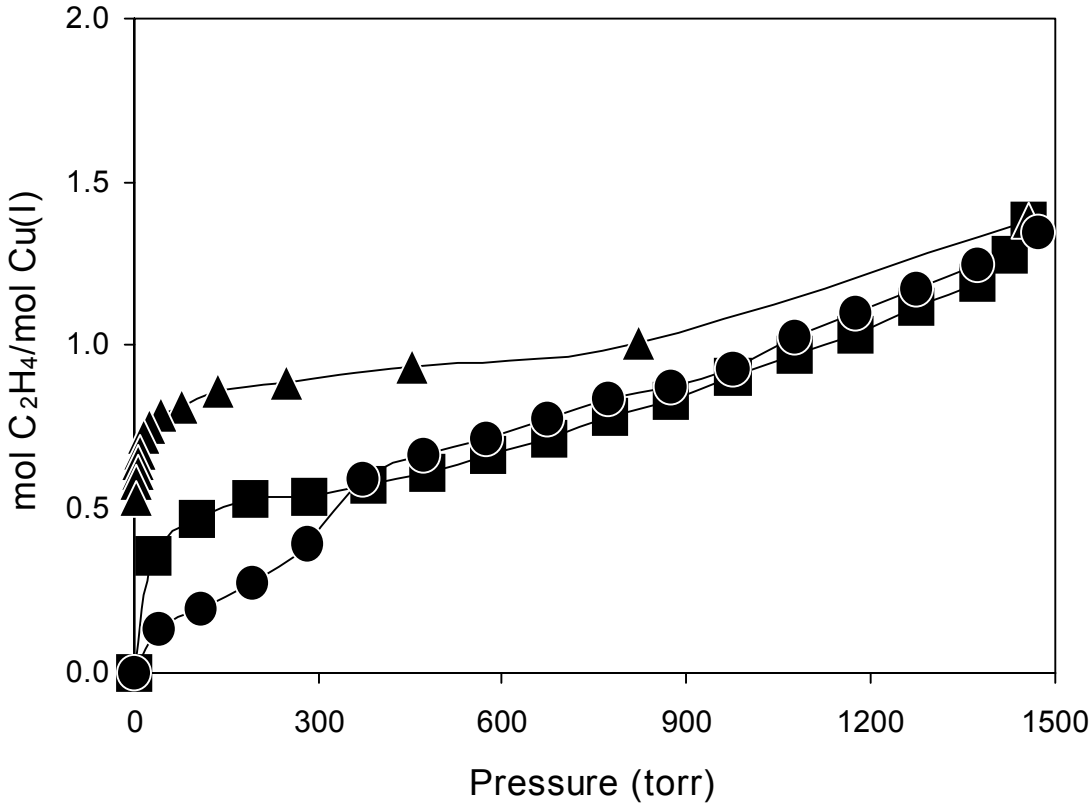

Figure 5.4. Volumetric gas measurements for the ethylene sorption/desorption by $((bz)Cu)_2Zr_2Cl_{10}$ (**2**). Sorption 1 (■), Desorption 1 (▲), and Sorption 2 (●).

ethylene is not removed until the pressure is reduced to below 100 torr. Upon resorption by the nearly desolvated material, **3**, a different sorption isotherm curve is observed from that of the initial benzene-replacement isotherm. From this cycle shown in Figure 5.4, the latter is suggestive of a cooperative binding process by which an interlayer "gallery" in the framework must be opened to initiate further sorption. The sorption and desorption of ethylene is reversible without any appreciable loss of activity, having been repeated for five cycles in our laboratory. Nevertheless, slight contamination from a small leak on the gas manifold results in the deactivation of this material.

Diffuse Reflectance Spectroscopy (DRS). DRS data collected during the sorption of C_2H_4 by $((bz)Cu)_2Zr_2Cl_{10}$ (**2**) are shown in Figure 5.5. The initial DRS of **2** (pink in Figure 5.5) exhibits a broad band edge at ca. 24,900 cm^{-1} (416 nm, 3.09 eV). This band edge is red shifted from that of CuCl (3.2 eV) and that of $ZrCl_4$, which is in the vacuum ultraviolet. Exposure with up to 200 torr of C_2H_4 appeared to have little effect on the position of the band edge, although an increase in absorption intensity is observed at higher energy. At 300 torr of C_2H_4, the band edge shifts dramatically to ca. 30,000 cm^{-1} (333 nm, 3.72 eV) indicative of a structural phase transition (royal blue in Figure 5.5). This phase transition is also observed in the volumetric experiments at which point 0.5 equivalents of ethylene are sorbed per copper site. As the ethylene pressure is increased from 300 to 1500 torr a peak in the absorption spectrum with a maximum at 24,038 cm^{-1} (416 nm, 2.98 eV) is observed to grow in with a corresponding blue shift of the band edge at 30,000 cm^{-1}. The presence of an isosbestic point at 26,200 cm^{-1} indicates that gas sorption above 300 torr occurs without proceeding through another intermediate phase. By comparison to the volumetric data, these spectra are likely

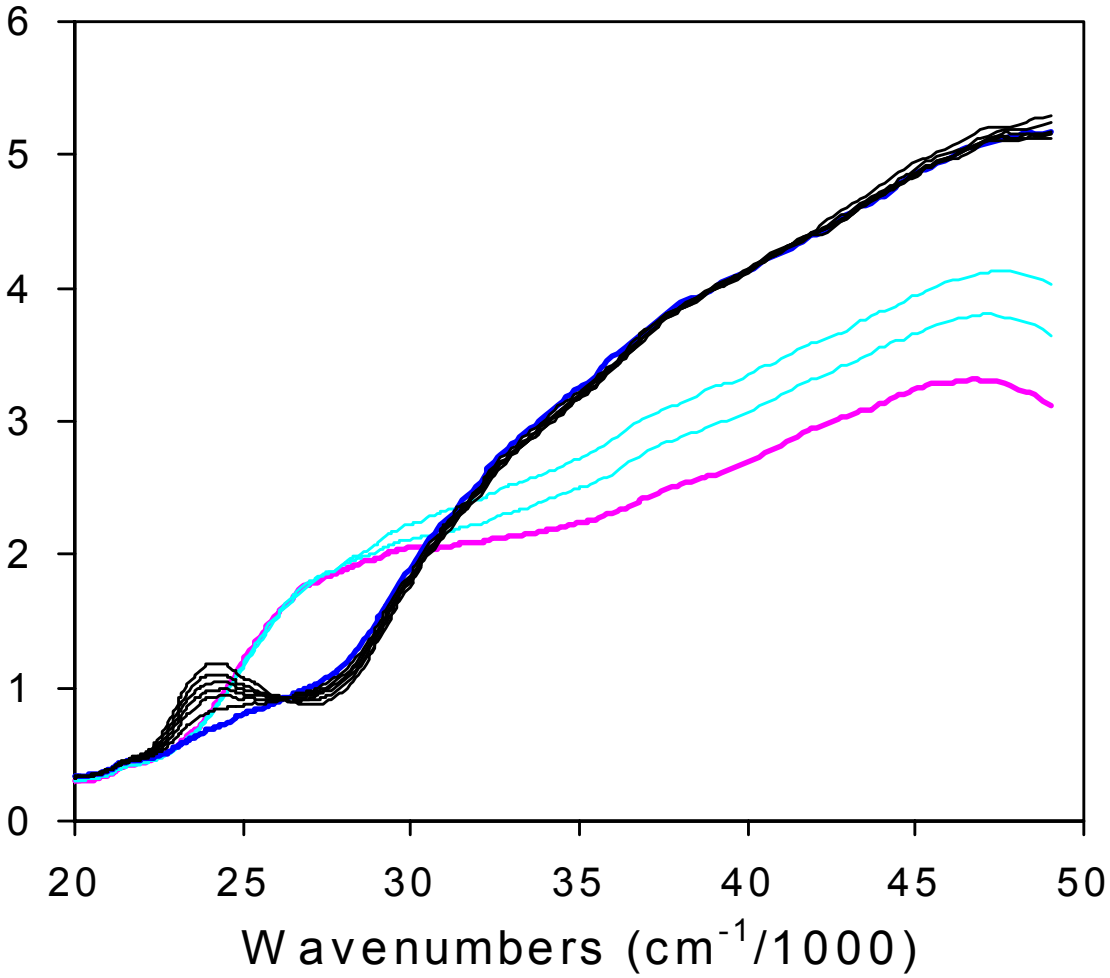

Figure 5.5. Diffuse reflectance spectroscopy for the sorption of ethylene by $((bz)Cu)_2Zr_2Cl_{10}$ (**2**) (—). Exposure to 100 and 200 torr (—), 300 torr (—), 400 to 1500 torr (—).

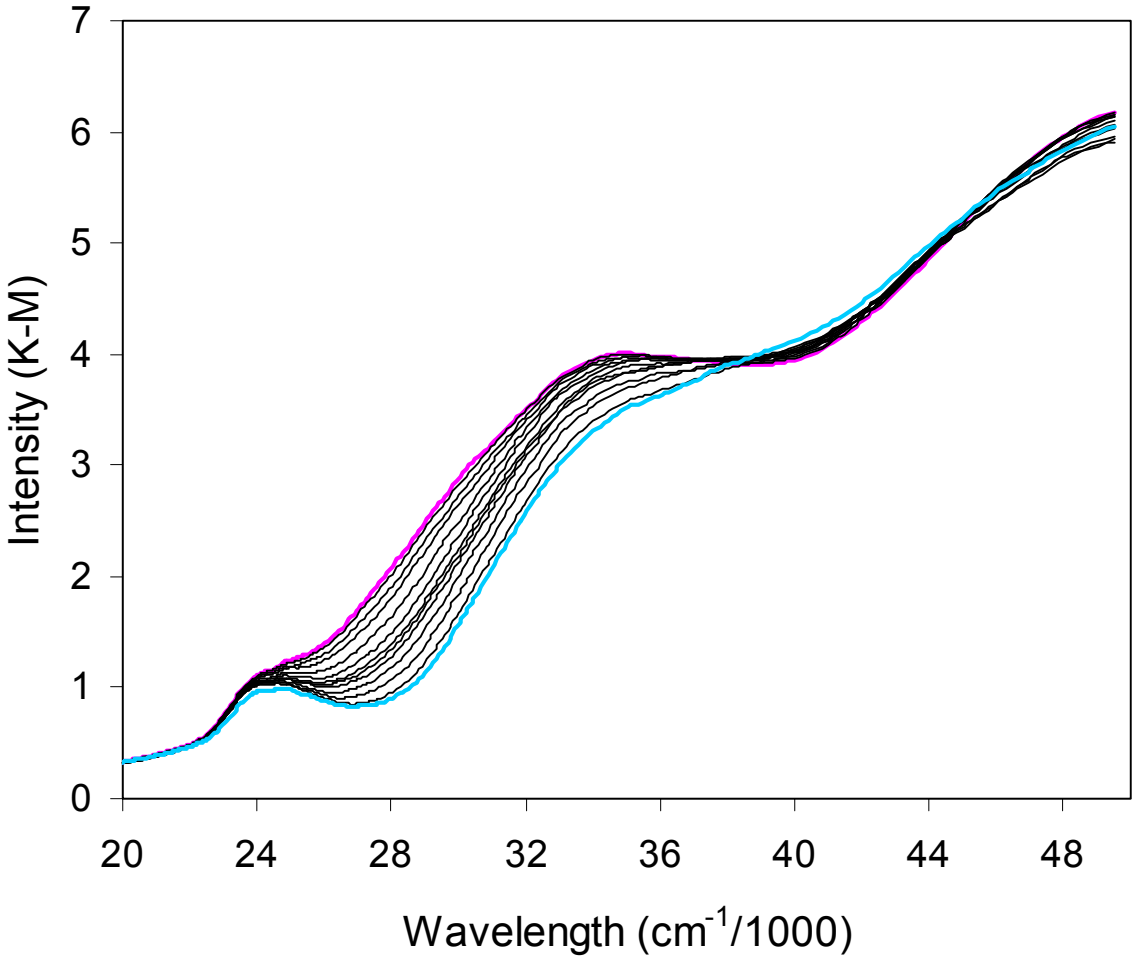

Figure 5.6. Diffuse reflectance spectroscopy for the desorption of ethylene from $((et)Cu)_2Zr_2Cl_{10}$ (**5**) (—).

associated with a 0.5 eqs of C_2H_4 per Cu^+ site intermediate, **4**, and a 1:1 C_2H_4:Cu^+ adduct, **5**. Upon desorption of ethylene from **5**, the minima at approximately 27,000 cm^{-1} slowly disappears proceeding towards the completely desolvated material, $Cu_2Zr_2Cl_{10}$ (**3**), as seen in Figure 5.6. An isosbestic point at 38,600 cm^{-1} during the desorption also indicates that no intermediates are present between the totally sorbed, **5**, and desorbed, **3**, materials (black and pink in Figure 5.6) .

Sorption of ethylene by $Cu_2Zr_2Cl_{10}$ (**3**) to form intermediate **4** is shown in Figure 5.7. The band edge associated with **3** is red shifted compared to **2** by about 500 cm^{-1} to 24,400 cm^{-1}. In this sorption experiment the sample was exposed to 1500 torr of ethylene, which lead to the gradual shift in the band edge towards 30,000 cm^{-1}, the band edge associated with intermediate **4**. This is in marked contrast to the abrupt transition from **2** → **4** by ligand displacement. The presence of an isosbestic point at 36,000 cm^{-1} indicates that the gradual sorption of ethylene by **3** to **4** does not proceed through an intermediate phase. The absorbance at 24,038 cm^{-1} was not observed upon prolonged exposure to ethylene, likely due to diffusion problems sometimes associated with these experiments. The ethylene was then removed under dynamic vacuum, whereupon the band edge for **4** is seen to slowly shift to lower energy, and eventually returns to the desorbed material, **3**, as seen in Figure 5.8. The isosbestic point is again observed at, 36,000 cm^{-1}, as seen for the sorption data in Figure 7. This sorption/desorption cycle between **3** and **4** was repeated three additional times to show the reversibility between these two phases. In each cycle the same gradual sorption and desorption was observed.

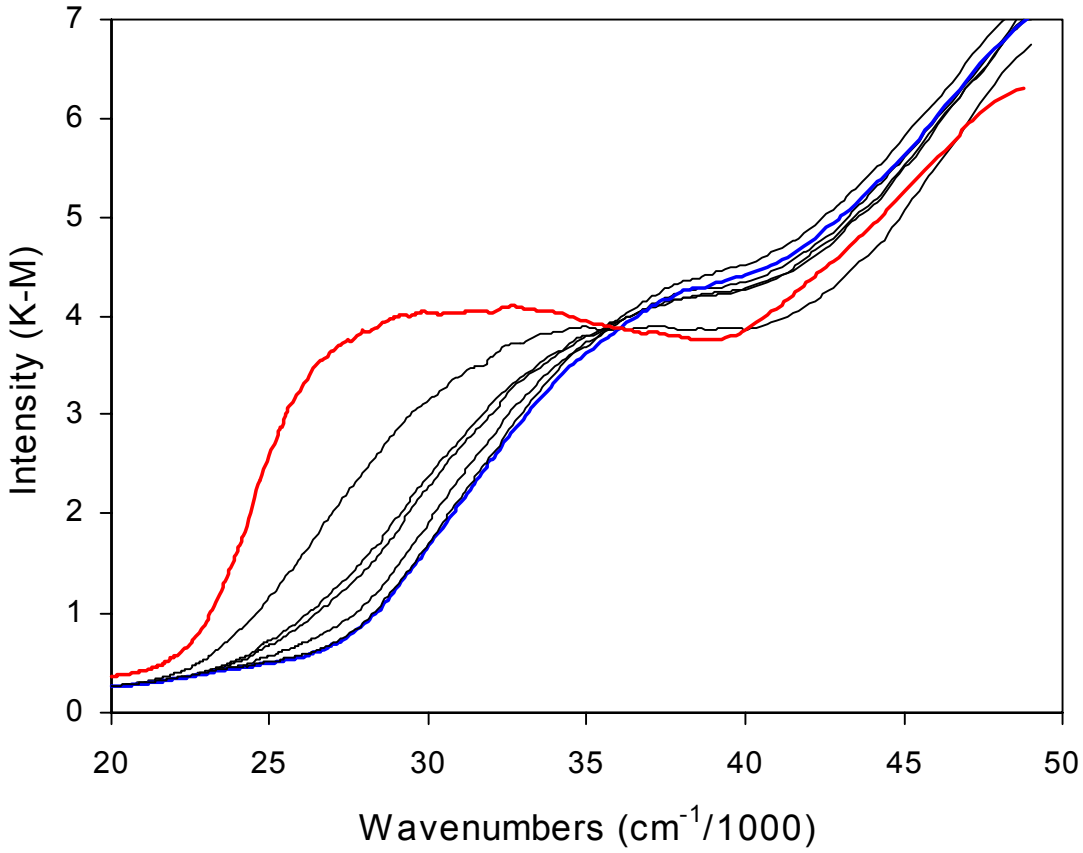

Figure 5.7. Diffuse reflectance spectroscopy for the sorption of ethylene by $Cu_2Zr_2Cl_{10}$ (**3**) (—). Spectra in black show **3** sorbing ethylene over one hour at 1500 torr C_2H_4. (et)$Cu_2Zr_2Cl_{10}$ (**4**) (—).

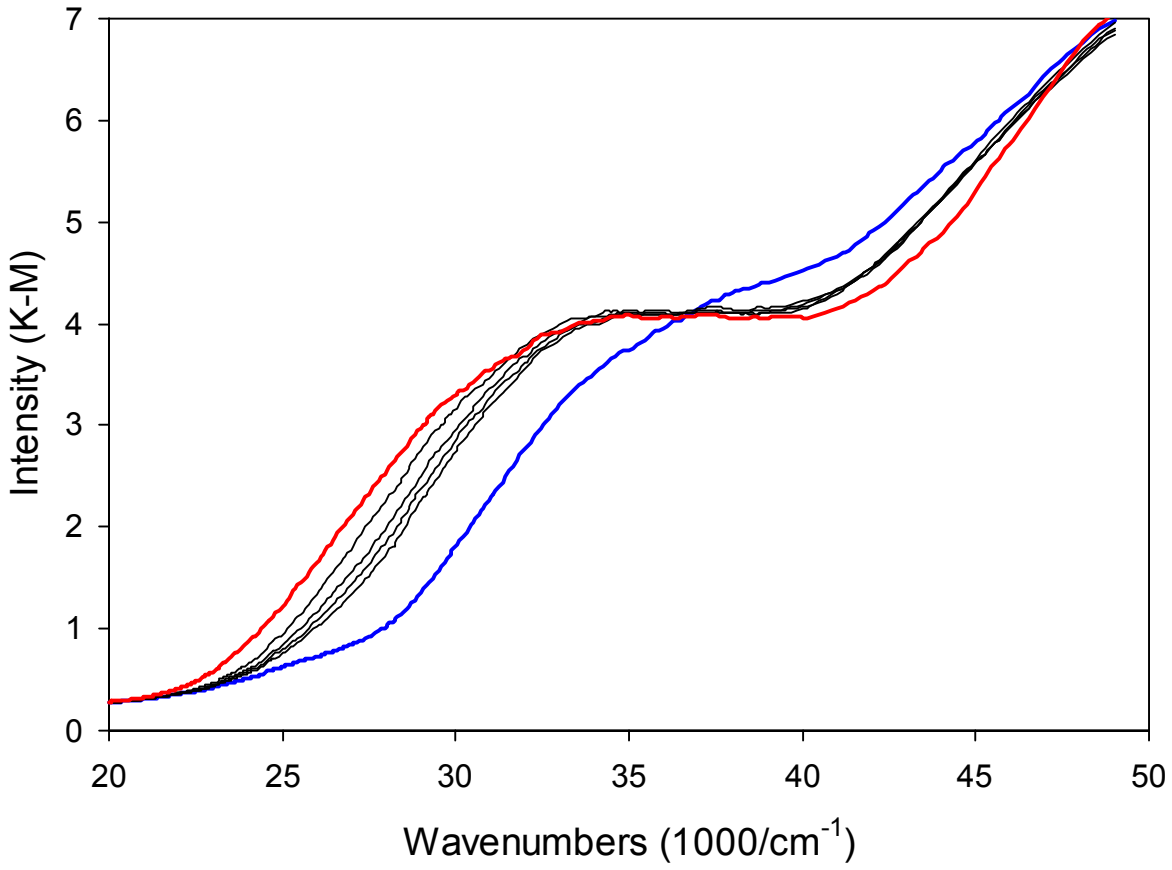

Figure 5.8. Diffuse reflectance spectroscopy for the desorption of ethylene from (et)$Cu_2Zr_2Cl_{10}$ (**4**) (—). Spectra in black indicate the slow, incomplete, desorption of ethylene over a period of 3 hours. The final spectrum (—) is not the completely desorbed material.

Time Resolved X-ray Diffraction (TRXRD). Time resolved X-ray diffraction (TRXRD) experiments were preformed at the National Synchrotron Light Source, Brookhaven National Laboratory, to monitor the structural changes taking place during the sorption of ethylene by $((bz)Cu)_2Zr_2Cl_{10}$ (**2**) that correspond with the volumetric and spectroscopic experiments described above. Ethylene was added to **2** in 100 torr increments to carefully monitor the formation of the C_2H_4 adduct as seen in the TRXRD shown in Figure 5.9. The sample was initially placed under vacuum (ca. 50 mtorr); however, no appreciable loss of benzene occurs during this initial evacuation of the sample as no changes in the diffraction pattern (black diffraction patterns) were observed. This is consistent with the sample retaining its luminescence during the initial evacuation step of the volumetric and spectroscopic experiments described above. With the incremental addition of ethylene to **2**, the sample slowly converts to a final ethylene adduct phase, **5**, without proceeding through an intermediate, in contrast to volumetric and spectroscopic experimental results. The conversion from **2** to **5** occurs over a relatively small pressure range between 400 and 800 torr of ethylene (blue diffractograms) after which the sample does not appear to undergo any further structural changes (green diffractograms) at higher pressures of ethylene. In Figure 5.10, the powder patterns for **2** and **4** have been plotted in d-spacing to directly compare the two phases which are listed for the individual peaks in Table 5.5. Desorption of ethylene from **4** was not observed because the seal of the sample capillary to the goniometer gas line is insufficient to obtain adequate vacuum to remove the ethylene without decomposing the sample due to exposure to atmospheric pressure and/or moisture.

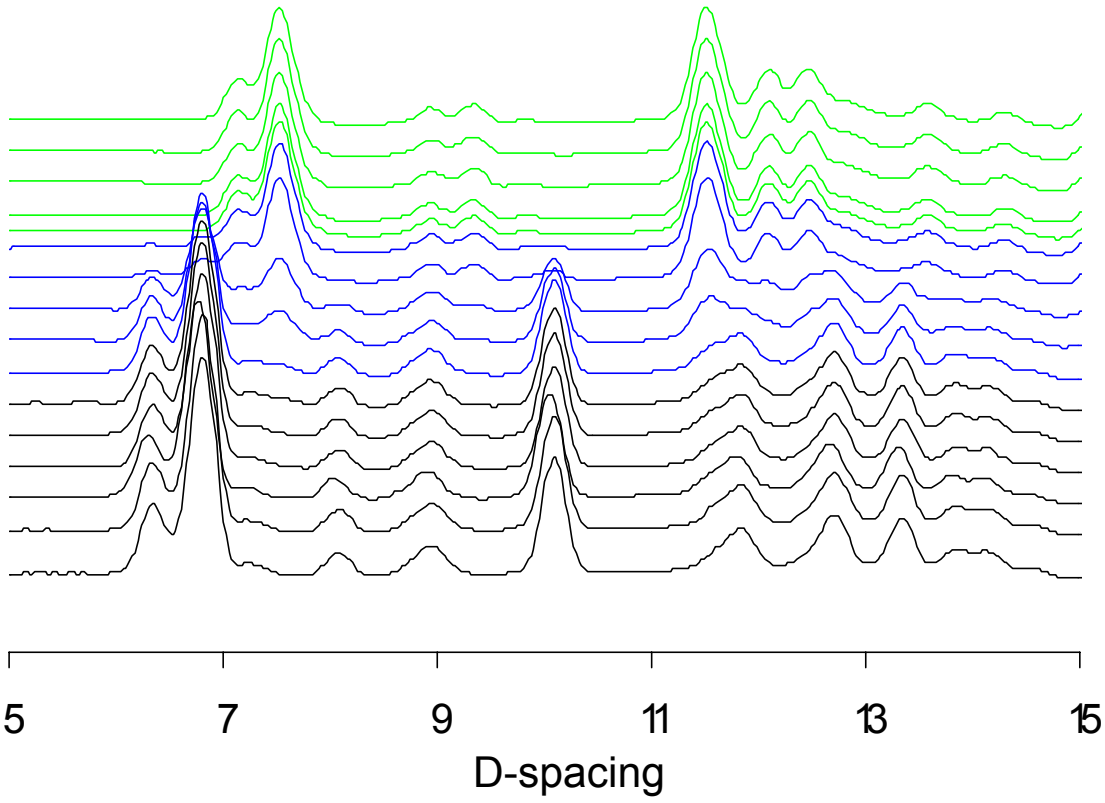

Figure 5.9. Time resolved X-ray diffraction of the ethylene sorption by $((bz)Cu)_2Zr_2Cl_{10}$ (**2**) upon exposure to ethylene in 100 torr increments.

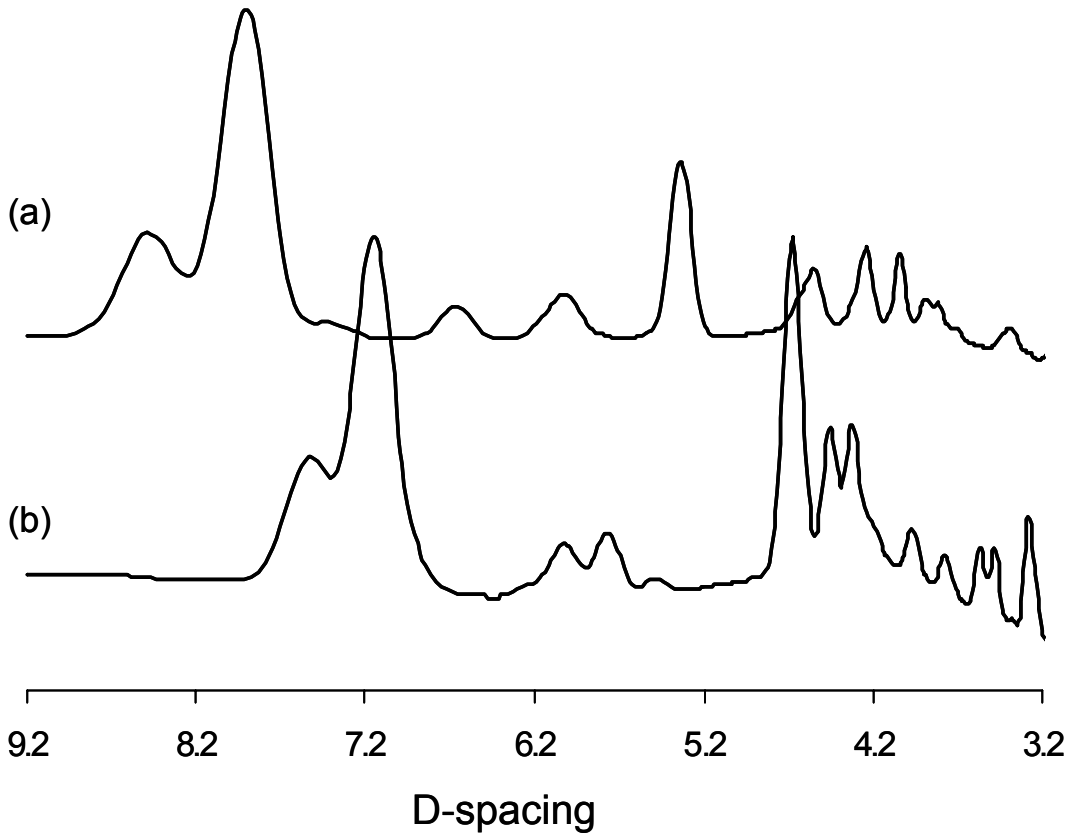

Figure 5.10. Diffractograms of (a) $((bz)Cu)_2Zr_2Cl_{10}$ (**2**) and (b) $((et)Cu)_2Zr_2Cl_{10}$ (**5**).

Table 5.5. D-spacing for $((C_6H_6)Cu)_2Zr_2Cl_{10}$(**2**) and $((C_2H_4)Cu)_2Zr_2Cl_{10}$(**5**) from TRXRD.

$((C_6H_6)Cu)_2Zr_2Cl_{10}$(**2**)	$((C_2H_4)Cu)_2Zr_2Cl_{10}$(**5**)
8.49	7.50
7.87	7.12
7.34	6.30
6.65	5.74
5.98	5.98
	5.45
5.33	4.68
4.51	4.42
	4.30
	4.17
4.22	3.95
4.03	3.75
3.84	3.55
3.78	3.46
3.67	3.33
3.95	3.27

A sample of the undissolved by-product and the unreacted starting material, CuCl, from the synthesis of **1** was also exposed to ethylene and monitored by TRXRD as shown in Figure 5.11. The sample was placed under vacuum for ten minutes where no appreciable change in the pattern was observed (blue peaks). The sample was then exposed to 1500 torr of ethylene at which point a new ethylene adduct phase (red peaks) is rapidly formed at the expense of the starting material. After ten minutes under ethylene pressure, the ethylene was removed under reduced pressure. Upon desorption, the diffraction intensity for the ethylene adduct phase begins to decrease and the diffraction pattern for a new phase (green), which is similar the starting sample, is observed.

5.4. Discussion

The $((bz)_2Cu)_2Zr_2Cl_{10}$ molecules in **1** are constructed from an edged-shared zirconium bioctahedron, such that the zirconium atoms share two chlorides, Cl(1) and Cl(2), and have two terminal chlorides, Cl(5) and Cl(6) in the equatorial plane of the bioctahedron as seen in Figure 5.1. The axial chlorides, Cl(3) and Cl(4), on each side of the bioctahedron, form a bridge to Cu, such that a boat-like geometry is observed for the $Cu_2Zr_2Cl_4$ tetrameric ring. The two copper atoms are coordinated in a *cis*-conformation with respect to the axial plane of the bioctahedron. And, the Cl(3)-Cu-Cl(4) plane is bent ca. 31° out of the Cl(3)-Zr'-Cl(4)'-Cl(3)'-Zr-Cl(4) molecular plane resulting in a Cu-Cu separation of 7.55 Å. Each copper is also bound to two benzene molecules, one in an η^2-fashion, Cu-C(7) = 2.237(7) Å and Cu-C(8) = 2.235(8) Å, while the second is weakly

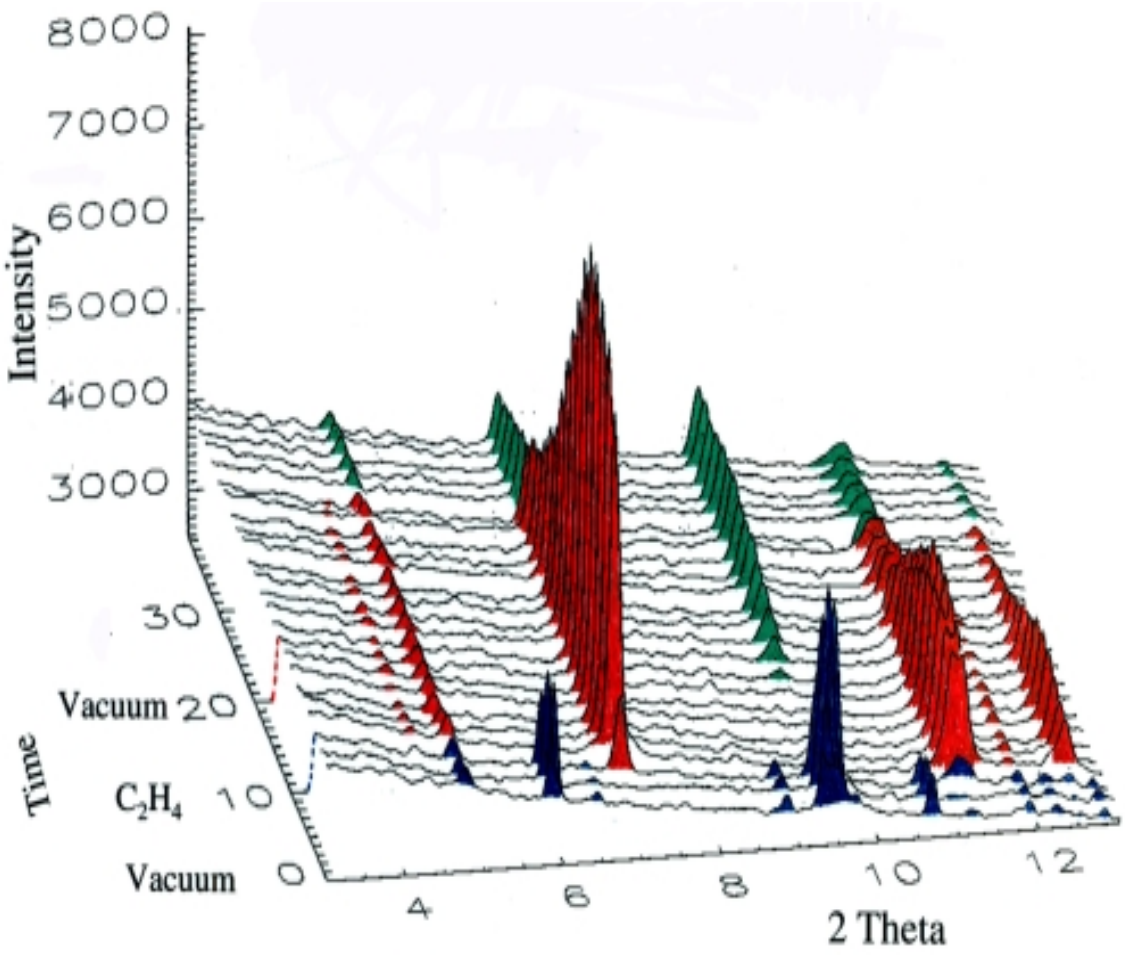

Figure 5.11. Time resolved X-ray diffraction (TRXRD) of the ethylene sorption at 1500 torr C_2H_4 by a mixture of an unknown copper-zirconium halide and CuCl.

coordinated in an η^1-fashion with a Cu-C(1) = 2.385(8) Å. The next nearest Cu-C distances are Cu-C(2) = 2.85(1) Å and Cu-C(6) = 2.90(1) Å.

Both edge-to-face π-interactions of the benzne ligands and hydrogen bonding to the halides contribute to the boat-like geometry of the $Cu_2Zr_2Cl_4$ tetramer core. They also stabilize the overall lattice. In particular, intramolecular hydrogen bonding contacts between chlorides and carbons of η^2-coordinated benzene ligands, Cl(2)-C(9) = 3.43 Å, appear to pull this coordinated benzene ligand toward the equatorial plane of the zirconium bioctahedron. The η^2-coordinated benzene is also observed to interact with the solvated benzene molecule, which helps to stabilize the boat-like orientation and connects the molecules into chains along the **c**-direction as described by the dashed lines in Figure 5.2. The closest contact from the midpoint of the face of the solvated benzene, B_s, to the edge of the η^2-bound benzene is 3.55 Å to C(8), which is similar to the edge-to-face π-interactions observed in the crystal structure of benzene, 3.6 Å.[22,23] Both of the coordinated benzene molecules are also involved in inter- and intramolecular edge-to-face π-type interactions along the **a** and **b**-directions yielding a three-dimensionally "π-stacked" lattice (Table 5.4). Significant intramolecular edge-to-face π-interactions are observed from the midpoint of the η^1-bound benzene, B_1, to the edge of the η^2-bound benzene, 3.36 Å to C(7), 4.21 Å to C(8), and 4.03 Å to C(12). And, intermolecular interactions are found to the η^1-bound benzene of adjacent molecules, 3.61 Å to C(4). Only a few, relatively long, intermolecular interactions are found from the midpoint of the η^2-bound benzene, B_2, to neighboring benzene molecules; the strongest being C(1), 3.67 Å.

Desolvation of $((bz)_2Cu)_2Zr_2Cl_{10}$•(bz) (1). $((bz)_2Cu)_2Zr_2Cl_{10}$•(bz) (**1**) rapidly loses solvent under a nitrogen atmosphere to form a pale yellow material, **2**, that is also a brilliant yellow phosphor under UV excitation (Figure 5.3). Although the exact structure of this desolvated material is not known, elemental analysis is consistent with the loss of three moles of benzene per formula unit yielding a material with the formula $((bz)Cu)_2Zr_2Cl_{10}$ (**2**). It is reasonable to assume that the solvated and η^1-coordinated benzene molecules, both of which are only weakly held in the lattice, are those that initially desorb. As solvent is lost from the coordination sphere of copper, either a three coordinate copper forms or **1** undergoes a structural rearrangement such that terminal chloride ligands of a neighboring tetramer fill the copper coordination sphere. In general, Cu^+ adopts a tetrahedral coordination geometry, rather than a trigonal planar coordination environment of halides; although distortions toward trigonal pyramidal geometries are common. Thus, a trigonal geometry can not be conclusively excluded. However, the solvated and η^1-coordinated benzene also played a significant role in the lattice stabilization of **1**. Thus, upon desolvation, significant lattice recontruction is anticipated. Therefore, I propose that upon loss of solvent **1** undergoes a topotactic reconstruction to form chain $((bz)Cu)_2Zr_2Cl_{10}$ (**2**) and layered-type material $Cu_2Zr_2Cl_{10}$ (**3**), respectively, such as those schematically described in Figure 5.12.

The coordinative saturation and solvation by benzene molecules prevent condensation of the copper-zirconium molecules into extended networks. However, loss of the η^1-coordinated benzene molecules opens a coordination site on the copper atoms. To stabilize the crystal lattice, and likely, fill the coordination sphere of copper, the molecules may reasonably be expected to condense into one-dimensional chains along

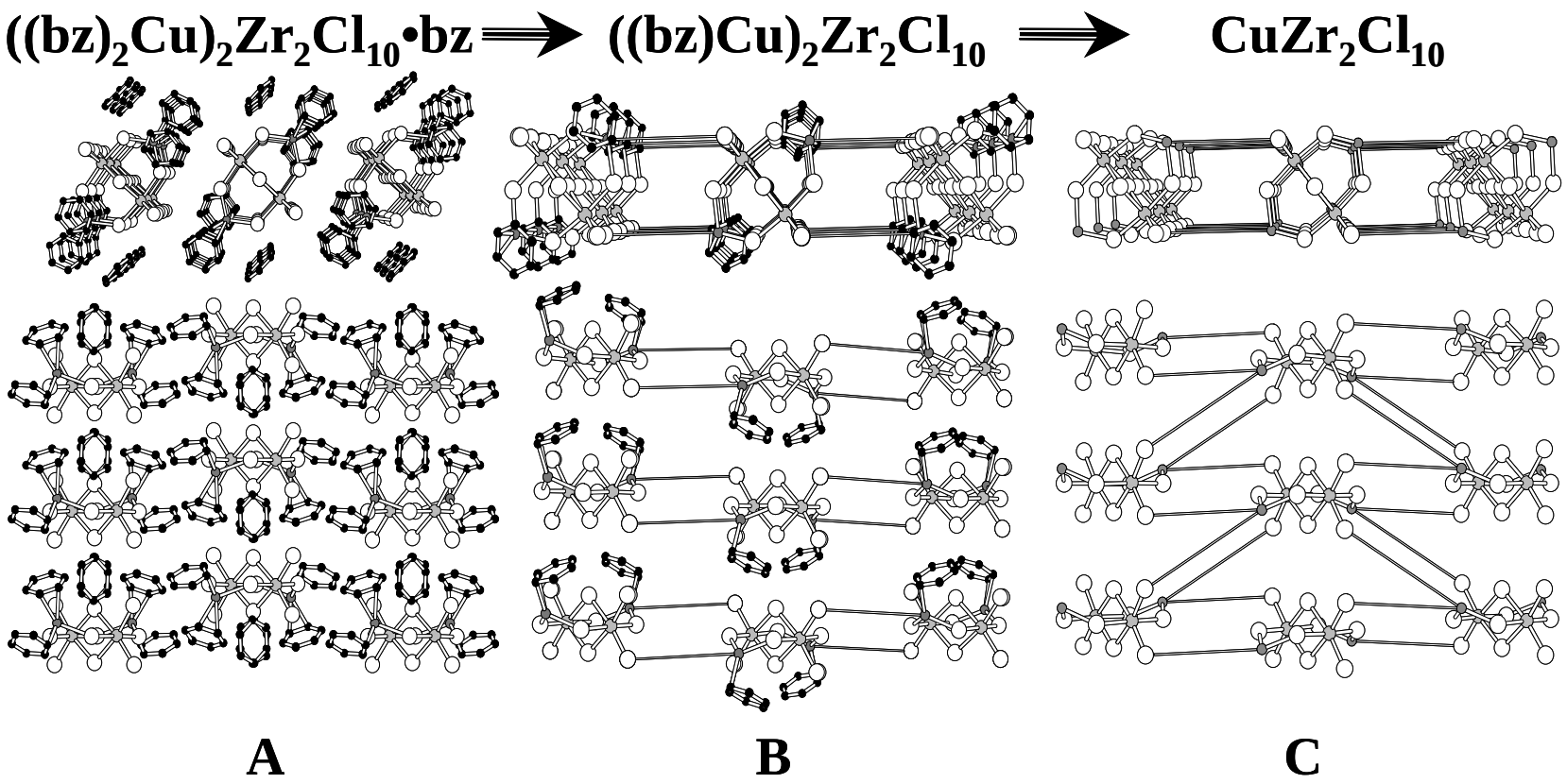

Figure 5.12. A schematic drawing of the desolvation process for $((bz)_2Cu)_2Zr_2Cl_{10}\cdot(bz)$ (**1**). Above are views looking parallel to the **b** axis and below are views emphasizing the proposed condensation layers derived from the **bc** planes of the crystal structure of **1**.

the **c**-direction as shown in Figure 5.12**B**. This condensation is envisioned to proceed by the formation of a bridge between the nearest terminal chlorides of neighboring zirconium bioctahedra, Cl(6), to the now coordinatively unsaturated copper(I) atoms. In the parent crystal structure of **1**, the Cu and Cl(6) atoms are separated by only 5.55 Å and are in fact directed toward the η^1-benzene ligand coordination site. This condensation would possibly form a chain-like structure running along the **c**-direction. Removal of the remaining η^2-coordinated benzene molecules by exposing the material to reduced pressures for several hours results in an open coordination site on the coppper atoms. The terminal Zr-Cl(5) chloride atoms of a neighboring molecule (1/2 b + 1/2 a) are directed toward the vacated η^2-benzene coordination site at a distance of only 6.58 Å in the structure of **1**. This further condensation of the chains results in a layered material, schematically described in Figure 5.12**C**. Support for the bonding features of the model structures from such a topotactic reconstruction is found by comparing the diffuse reflectance spectra of **2** and **3** to that of $((C_6H_6)CuCl_3)_2Zr$[24] and Cu_2ZrCl_6[23] (Figure 5.13). $((C_6H_6)CuCl_3)_2Zr$ is the one-dimensional chain formed from the solvothermal reaction of the three-dimensional framework Cu_2ZrCl_6 in benzene. In the previous chapter, the low energy absorption in the ternary Cu_2ZrCl_6 was assigned to a Cu-d^{10} to Zr-d^0 charge transfer,[24] while the absorption band edge in $((C_6H_6)CuCl_3)_2Zr$ is assigned to a copper-to-benzene charge transfer.[25] The band edge of the 1-D chains in $((C_6H_6)CuCl_3)_2Zr$, where benzene is coordinated to copper, 24,700 cm^{-1}, is red shifted from that of the condensed phase, Cu_2ZrCl_6, 23,600 cm^{-1}. In a similar manner, the absorption band of **2**, 24,900 cm^{-1}, is red shifted to 24,400 cm^{-1}, presumably due to the loss of benzene and condensation of the chains upon formation of **3**. It is likely then that the absorption band

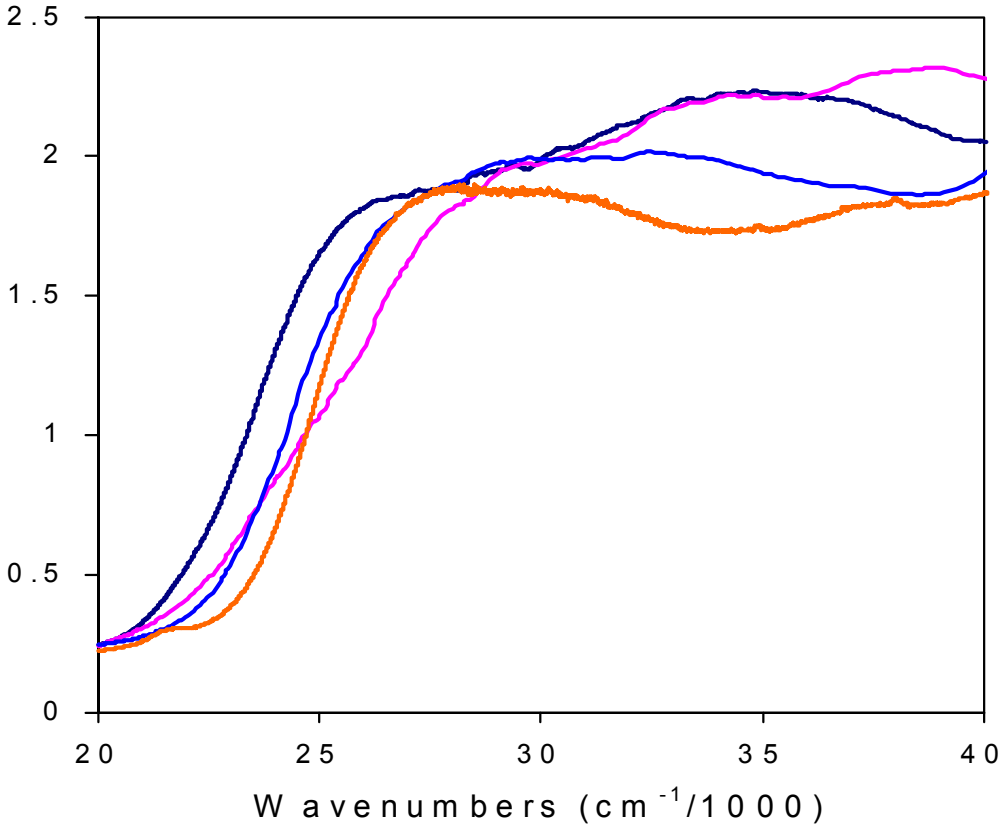

Figure 5.13. Diffuse reflectance spectra of Cu_2ZrCl_6 (—) and $((bz)CuCl_3)_2Zr$ (—) compared to $((bz)_2Cu)_2Zr_2Cl_{10}$ (2) (—) and $Cu_2Zr_2Cl_{10}$ (3) (—).

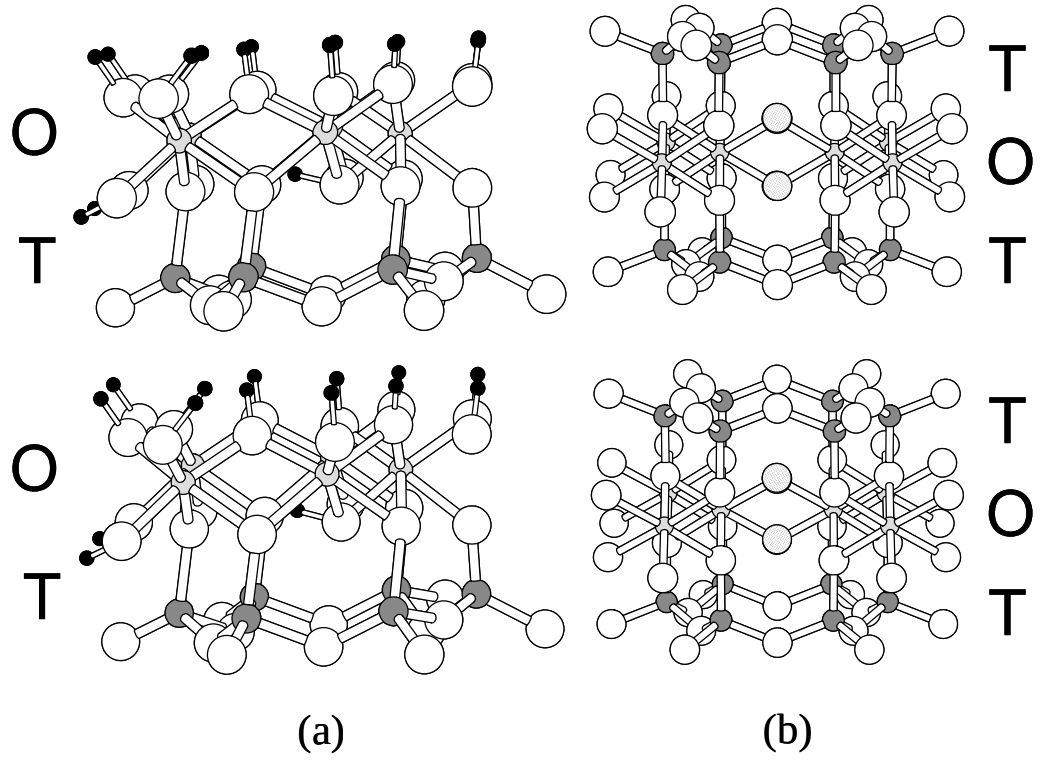

Figure 5.14. Ball and stick drawing of idealized structures of (a) kaolinite, $[Al_4Si_4O_{10}(OH)_4]$, and (b) montmorillonite, $[Al_4Si_8O_{20}(OH)_4]$. Unshaded spheres are O, smaller shaded spheres are Al, and larger, darker spheres are Si. Small, black spheres represent hydrogen atoms. In (b) largest shaded spheres represent OH groups.

in **2** is associated with a copper-to-benzne charge transfer analogous to that observed for $(bzCuCl_3)_2Zr$. By contrast, the absorption band in **3** is likely associated with a Cu-d^{10} to Zr-d^0 charge transfer. Such a comparison of the absorption spectrum of **2** and **3** implies that the empty zirconium d-orbitals are at a similar energy as the benzene LUMO.

Analogy to silicate-based clay materials. Examples of kaolinite and smectite clays are shown in Figure 5.14.[26] Kaolinite, the major constituent of china-clay, has the idealized formula, $[Al_4Si_4O_{10}(OH)_8]$ (Figure 5.14a), and is constructed from alternating layers of silicate tetrahedra and aluminate octahedra. The formula is idealized because a variety of cations and anions can be substituted into this material. Such clays are known as 1:1 or T:O clays, where T = tetrahedral layer and O = octahedral layer. Hydrogen atoms attached to oxides bridging aluminum octahedra create significant hydrogen bonding between the layers which makes them difficult to separate apart. Another common clay-type architecture that is more germane to this discussion is that of the smecite-clay, montmorillonite, with the idealized formula $[Al_4Si_8O_{20}(OH)_4]$, shown in Figure 5.14b. This clay is constructed from repeating layers with a T:O:T arrangement, such that layers of tetrahedra encompass a layer of octahedra. Four out of the six oxides around an octahedron bridge to a silicate tetrahedron and an adjacent octahedron, such that each is three-coordinate. The other two oxides (shaded in Figure 5.14b) are shared between only two octahedra, and have a terminal hydrogen (not shown) filling the third coordination site, which sits in the center of a six ring of silicate tetrahedra. The usefulness of smectite clay results from an ability to readily reversibly incorporate water or organic molecules into the interlayer region, which "swells" or increases the distance between layers, i.e. increases the **c**-lattice direction, without affecting the **a** or **b**

crystallographic axes. Incorporation of organic molecules into the interlayer region limits the reaction area and brings the molecules into close contact with the terminal hydrogen atoms, which are utilized in acid-base chemistry on the organic materials.

The T:O:T layers of the montmorillonite clay shown in Figure 5.14b are reminiscent of the proposed layered structure of the fully desorbed material, **3**, Figure 5.12**C**. Both the proposed structure for **3** and montmorillonite are similar in that each is constructed from neutral T:O:T layers. However, whereas the reactivity of the clay generally results from the accessibility to the interlayer terminal protons, the reactivity for the copper-zirconium materials results from a direct interaction with the constituent copper atoms of the two-dimensional layer. Assuming that **3** has a similar layered structure to montmorillonite shown in Figure 5.14b, one can envision breaking one of the metal-anion bonds that bridge tetrahedra to allow for ethylene binding, while the overall layered structure is maintained. Such reactivity is possible with the labile metal-halide bonds and not with much stronger M-O bonds. Metal-halide materials with clay-type architectures may be optimal for the sorption of small gas molecules, like ethylene, provided the gas can access the interlayer region in order to bind to copper. Studies to examine the gas sorption properties of the copper-zirconium-chloride materials **2** and **3** are described below.

Ethylene Sorption/Desorption by the Copper-Zirconium Materials. In support of the "clay-type" structural analogy proposed here upon desolvation of benzene from **1**, the desorbed materials, **2** and **3**, were shown to exhibit similar reactivity patterns with regard to the reversible sorption of ethylene. Time-resolved X-ray diffraction (TRXRD), volumetric gas sorption data, as well as diffuse reflectance spectroscopy were

employed to monitor and characterize the details of the reversible ethylene sorption. Using **2** as the starting material, presents the problem that the precise amount of benzene coordinated to copper in the sample is not known. However, both spectroscopic and synchrotron diffraction experiments confirm that there is little change in the benzene coordination in **2**, during the initial evacuation at room temperature prior to ethylene sorption. Furthermore, by working at room temperature, the vapor pressure of the benzene that is displaced by ethylene is significantly less than that of the ethylene such that it minimally contributes to the observed pressure.

Both volumetric and spectroscopic measurements, Figures 5.4-8, demonstrate that the sorption of ethylene by **2** occurs via a multi-step mechanism. There is a significant difference in the sorption isotherms below 400 torr between the initial sorption starting from **2**, and, the subsequent isotherms for which the sorption is apparently into the fully desorbed **3**. Whether sorption by **2** or **3**, the same intermediate adduct, (et)$Cu_2Zr_2Cl_{10}$ (**4**), is formed upon exposure to about 300 torr of ethylene. The formation of **4** from **2** likely proceeds by a benzene ligand loss and ligand exchange upon sufficient exposure to ethylene pressure. The initial exposure of **2** to low pressures of ethylene result only in a gradual increase in intensity of the high-energy portion of the absorption spectrum, however, no significant change in the band edge is observed. An abrupt phase transition is observed upon increasing the ethylene pressure to 280 torr at which point a dramatic blue shift to the band edge is observed; 24,900cm^{-1} to 30,000cm^{-1}. This is consistent with formation of the intermediate ethylene adduct **4**, which by volumetric measurements contains one ethylene ligand for every two copper sites. The blue shift in the band edge of the absorption spectrum by about 5,000 cm^{-1} is consistent with an assignment of this

feature to a metal-to-ligand charge transfer since the LUMO of the delocalized π-system of benzene should be significantly lower in energy than π*-LUMO of ethylene. Unlike **2**, the ethylene adduct **4** is not photoluminescent.

The sorption of ethylene into **3**, formed after the first sorption/desorption cycle, requires a higher ethylene pressure to form the intermediate **4** than was required for the ligand exchange upon ethylene sorption into **2** (Figure 5.4). This type-V isotherm is further consistent with a mechanism whereby a small amount of ethylene must be sorbed into **3** in order to open up the lamellar galleries that are necessary to sorb sufficient ethylene to form the intermediate **4**. Nevertheless, spectroscopic signatures, and the continued sorption of ethylene confirm that the intermediate **4** is common to both reaction pathways, starting from either **2** or **3** as seen in Figures 5.5 and 5.7, respectively. The intermediate **4** continues to sorb ethylene as the gas pressure is increased from 400 to 1500 torr. As seen in the isotherms of Figure 5.4, the sorption limit of the sample has not been achieved at the pressure limit of our gas line. Nevertheless, it is clear that by this pressure 1.25 to 1.5 equivalents of ethylene are sorbed per copper site. At the ethylene pressure of 1500 torr, 17 cc ethylene are sorbed per gram of sorbate. Such sorbtive capacity is similar to that described for mesoporous materials, when one takes into account the heavier cations and anions used here. The diffuse reflectance spectra, Figure 5.5, clearly show the clean transition from the intermediate **4** to the higher ethylene adduct **5** with an isosbestic point at 26,200 cm^{-1}. The absorption centered at 23,090 cm^{-1} has a band edge at approximately the same energy as that found for the condensed phase, **3**, as well as the ternary Cu_2ZrCl_6, which has been assigned to a Cu-d^{10} to Zr-d^0 charge

transfer. Because this band edge does not shift during the desorption of ethylene from **5**, Figure 5.6, it is most reasonable to assign it to a Cu-d^{10} to Zr-d^0 charge transfer as well.

The results of the volumetric and spectroscopic investigations are summarized schematically in Figure 5.15. The luminescent material **2** readily sorbs ethylene in a step-wise fashion to form an intermediate that has sorbed 0.5 equivalents of ethylene per copper site, **4**, then continues to sorb ethylene to form a 1:1 adduct, **5**. The ethylene can then be removed under reduced pressures. The fully desorbed material **3** was then shown to initially convert to **4** consistent with the sorption pathway beginning with the benzene coordinated material, **2**.

Time Resolved X-ray Diffraction. TRXRD experiments were performed in order to monitor the structural changes alluded to by the volumetric gas sorption experiments. Similar to the volumetric and spectroscopic experiments described above, ethylene was incrementally added to **2**, and monitored by TRXRD as seen in Figure 5.9. This data indicated that **2** slowly proceeds to the final ethylene adduct between 400 and 800 torr without proceeding through an intermediate in contrast to the volumetric and spectroscopic experiments described above. However, diffusion of the gas through the sample has been a problem in the TRXRD experiment, which may prohibit an observable intermediate phase. The final phase from this experiment is presumably the 1:1 C_2H_4:Cu^+ adduct, **5**, because the sample did not appear to sorb ethylene above 800 torr. Furthermore, both the initial benzene coordinated material, **2**, and the final ethylene adduct phase, **5**, were observed to have similar diffraction patterns. The diffraction

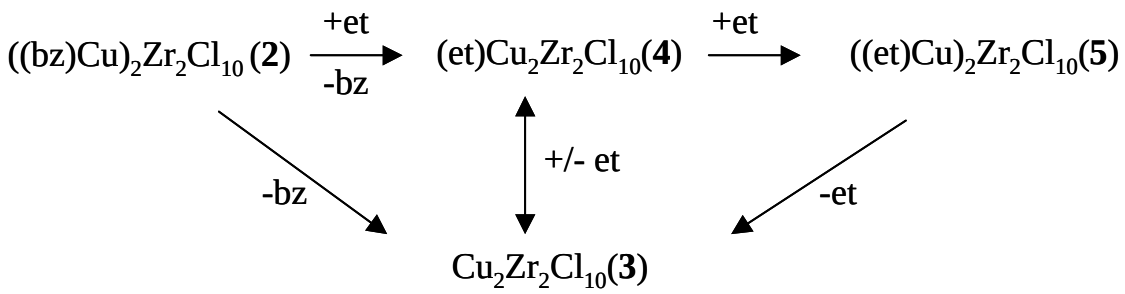

Figure 5.15. Schematic drawing summarizing the structural relationships derived from the volumetric and spectroscopic measurements.

patterns of **2** and **5** are shown plotted as a function d-spacing in Figure 5.10. Qualitatively one can see from Figure 5.10 that the majority of the reflections for the two phases have shifted to smaller d-spacing values without a dramatic change in the peak intensities. And, most of the reflections in **2** can be associated with a corresponding reflection in **5** as indicated in Table 5. Based on the first major reflections, which are generally related to the distance between repeat layers, a 1.0 Å decrease in the d-spacing is observed upon displacement of benzene by ethylene. This is consistent with a displacement of the benzene by a smaller ethylene molecule without a major structural change to the inorganic material. Such behavior is typically observed for clay-type materials.

Interestingly, the unknown by-product from the reaction, that yields **1**, was also found to sorb/desorb ethylene as seen in Figure 5.11 in a similar manner to **1**. Upon exposing this unknown material to 1500 torr of ethylene, an immediate structural change was observed by the disappearance of the initial powder pattern in blue, and the appearance of an ethylene adduct phase shown in red. The peaks associated with the ethylene adduct are at lower 2θ values, which would again be consistent with a decrease in lattice constants due to the displacement of the larger benzene molecules by smaller ethylene molecules. The ethylene was removed under reduced pressure to form a new phase, shown in green in Figure 5.11, that is similar, but not identical to the starting material. The diffraction pattern of the final, organic-free phase indicates a further decrease in lattice constants, as the diffraction peaks are shifted again to higer 2θ values (or smaller d-spacing), consistent with a structure that continues to condense. The final phase should not be expected to be identical to the initial phase because all bound

benzene is displaced by ethylene, and subsequently removed by vacuum. The fact that the ethylene could be removed from this unknown copper-zirconium phase with the TXRD experimental set-up may indicate that the ethylene is not as strongly bound to this material as to **2**. Alternatively, because the sample was diluted in CuCl, which is inert with respect to ethylene sorption under these reaction conditions, diffusion problems may have been fortuitously eliminated. These results indicate that a variety of structures in the copper-zirconium system may exhibit gas sorbing capabilities, which can be studied in the future.

Luminescence by $((bz)Cu)_2Zr_2Cl_{10}$ (2). The Cu^+ centers can frequently serve as the luminescent activator resulting in materials that exhibit emission across the visible spectrum. The high-lying filled d-orbitals and low-lying empty s-orbitals, or their combination with ligand orbitals of similar energy, are responsible for the observed excitation and emission phenomenon. The d←s metal-metal transition is generally observed for isolated Cu^+ centers and results in a green to blue emission, such as was previously characterized for $CuAlCl_4$.[4] The excitation at 26,000 cm^{-1} and yellow emission at 16,000 cm^{-1} observed for 2 are more characteristic of a metal-to-ligand charge transfer, which is chemically consistent with a copper to benzene transition. The lower energy of excitation and emission observed for 2 as compared to $CuAlCl_4$ is consistent with the benzene LUMO being intermediate in energy to the Cu-d and –s orbitals. Nevertheless, the approximately 10,000 cm^{-1} separation between the excitation and emission is indicative that a singlet to triplet intersystem crossing, similar to that described for $CuAlCl_4$, is responsible for this emission.

When benzene is replaced by ethylene, the absorption edge is moved to significantly higher energy, and the brilliant yellow emission is also lost. Changes in the crystal lattice undoubtedly influence this loss of the photoluminescence. However, the higher excitation energy may populate higher levels in the singlet manifold, which have greater overlap with the excited-state hyper-surface, such that after a rapid relaxation to the vibrational ground state of a high-lying singlet excited state, the process of internal conversion allows for a nonradiative relaxation through the singlet manifold to the singlet ground state. Under these conditions the intersystem crossing to the triplet excited state is not competitive, and hence the luminescence is not observed.

Ethylene sorption by a transfer of Lewis acidity. The reversible binding of ethylene at room temperature by Cu^+ in the presence of $ZrCl_4$ contrasts with the ability of CuCl by itself in the solid state to bind ethylene only at low temperature (0°C) and high pressures (>60 atm C_2H_4).[27] Furthermore, previous research to prepare and design Cu^+ complexes that bind ethylene have largely been directed towards the preparation of Cu^+-amine complexes. Such Cu^+-amine complexes have been designed to model the copper receptor site in the enzyme ETR-1,[28,29] which binds ethylene. Most complexes of this type that have been crystallographically characterized generally have a CuL_2 (where L_2 = two mono- or one bidentate amine containing ligand) fragment. Upon ethylene coordination the copper becomes three coordinate in a trigonal planar geometry.[30-33] Four-coordinate copper(I)-amine complexes have been prepared, but only when there is a constraint on the ligand environment, for example, with hydrotris(pyrazoyl)borate ligands.[34,35] The preferred trigonal coordination environment about copper is optimal for binding ethylene to a copper complex containing strong σ-donor ligands such as amines.

For these complexes, ethylene binding is enhanced by an electron donation from the copper d-orbitals into the π^* orbital of ethylene. And, the overlap between these orbitals is maximized when copper adopts a trigonal planar coordination. Increasing the Lewis basicity of the amine donor ligand has been shown to increase the donor ability of Cu^+ leading to a stronger copper-ethylene interaction as determined spectroscopically.[30-35]

By contrast, the affinity for CuCl to sorb ethylene can also be enhanced by the coordination of strong Lewis acids to the copper center. For example, the metal-halide complexes, $CuAlCl_4$ and $CuGaCl_4$, in addition to the copper-zirconium materials described in this work, readily bind ethylene. The comparative sorption isotherms are shown in Figure 5.16. $CuAlCl_4$ sorbs more ethylene at lower pressures than $CuGaCl_4$, and can sorb up to two equivalents of ethylene per Cu^+ site, while $CuGaCl_4$ does not sorb more than 0.75 equivalents of ethylene per Cu^+ site under an ethylene pressure of two atmospheres. The $CuMCl_4$ materials are condensed, three-dimensional materials constructed from Cu^+ and Al^{3+} tetrachloride tetrahedra. Thus, a significant framework reconstruction is required to sorb ethylene; however, upon desorption the original three-dimensional structure of the $CuMCl_4$ material returns as observed by TRXRD.[36] Because both of the $CuMCl_4$ materials have the same structure,[37] the differences in sorption behavior must be due to the differing Lewis acid strength of Al^{3+} vs Ga^{3+}. The stronger Lewis acid studied here, Al^{3+}, may polarize the chloride ligands away from Cu^+ to a greater extent, than does Ga^{3+} or Zr^{4+}, which yields relatively weak and labile Cu-Cl bonds. The increased lability of the Cu-Cl bond is what allows $CuAlCl_4$ to sorb ethylene much more readily. In the copper-zirconium system, greater pressures are required to observe a comparable amount of ethylene sorption to that measured for $CuAlCl_4$ at lower

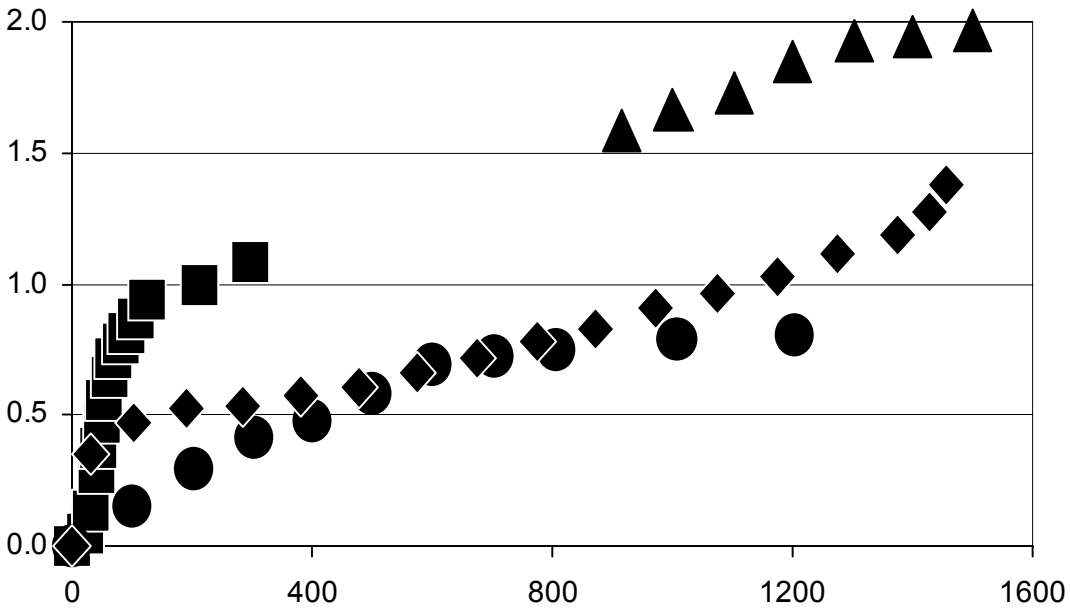

Figure 5.16. Volumetric ethylene sorption data for $((bz)Cu)_2Zr_2Cl_{10}$ (◆), $CuAlCl_4$ at exposing at low pressure (■), $CuAlCl_4$ exposing at high pressures (▲), and $CuAlCl_4$(●).

pressures. The copper-zirconium chloride, $((bz)Cu)_2Zr_2Cl_{10}$ (**2**), likely has a more accessible trigonal or tetrahedrally coordinated copper site, made available by the dissociation of the benzene ligands. Displacement of benzene by ethylene, as opposed to the reconstruction of a condensed framework, should lead to an enhanced sorptive property for **2** versus $CuAlCl_4$ based on structural arguments alone, however, this is not the case. Thus, the different strength of the Lewis acid between Al^{3+} and Zr^{4+} is likely the deciding factor in the sorption of ethylene or other ligands in these metal-halide material. Preliminary ^{31}P NMR studies currently underway on the triphenyl phosphine adducts to molecular copper-zirconium, -aluminum, and -galium complexes are consistent with such an argument.[38] For example, the chemical shift of the 1:1 PPh_3:$CuAlCl_4$ material, 2.911 ppm, is downfield from the corresponding chemical shift for the 1:1 $CuGaCl_4$-PPh_3 adduct, 2.531 ppm. And, both of these values are shifted downfield of free PPh_3, -4.98 ppm, and the 1:1 PPh_3:CuCl adduct, -3.68 ppm. The chemical shift for $(PPh_3Cu)_2ZrCl_6$ is even further downfield, 5.38 ppm, however as descibed in Chapter 3, Zr has low-lying unfilled d orbitals that can participate in charge transfer from the Cu^I. Thus, direct comparison with Al^{3+} and Ga^{3+} is not possible. Nevertheless, the large downfield shift is further indicative of a Lewis acidity transfer from the coordinated Lewis acid to the Cu^+ center.

The mechanism for ethylene binding in the Cu^+-amine complexes appears to differ from the metal-halide materials. In the metal-halide materials, the ability to bind ethylene has been demonstrated to increase with increasing strength of the Lewis acid bound to Cu^+. For the Cu^+-amine complexes, enhanced binding is attributed to an increase in the Lewis basicity of the amine ligands. These contrasting bonding features

can be reconciled by understanding the ability of copper(I) to readily donate *or* accept electron density. Copper (I) effectively maximizes ligand binding as an electron acceptor by making use of its low lying and empty s and p orbitals. Copper(I) can also donate its high-lying d-electrons in a π-type fashion to acceptor ligands like ethylene and carbon monoxide.[39] The π-backbonding from copper to olefins is a relatively weak interaction due to the energy difference between the copper d-orbitals and the π^* orbitals. And, as demonstrated in a number of systems both spectroscopically[34,35] and theoretically,[40] the dominant interaction between copper and ethylene is the σ-donation of electrons from ethylene to copper. Thus, π-backbonding can serve as a stabilizing force, as in the copper(I)-amine complexes, but it is not dominant. In the Cu^+-halides, the Lewis acid bound to copper inductively removes electron density from copper increasing the strength of the σ-donation from ethylene, thus stabilizes the copper(I)-ethylene interaction. In this way, the Lewis acid, Al^{3+}, Ga^{3+}, Zr^{4+}, etc., has transferred its Lewis acidity to copper, which increases the affinity for copper to bind small, gas molecules.

5.5. Conclusion

In conclusion, $((bz)_2Cu)_2Zr_2Cl_{10}\bullet C_6H_6$ (**1**), was synthesize, characterized, shown to lose solvent in a step-wise fashion to yield a chain, $((bz)Cu)_2Zr_2Cl_{10}$ (**2**), and a layered structure, $Cu_2Zr_2Cl_{10}$ (**3**). The layered material **3** likely exhibits a layed-network structure similar to a clay-type architecture. And, reminiscent of clay-type sorption behavior, both **2** and **3** were shown to reversibly bind ethylene through a combination of volumetric, spectroscopic and time resolved X-ray diffraction gas sorption measurements. The affinity for Cu^+ to sorb ethylene is shown to be enhanced by constructing a framework

from CuCl and another Lewis acidic metal-halide. Such ethylene binding to metal-halide complexes is dependent upon the Lewis acid strength of the metal bound to Cu(I), where the strongest Lewis acid yields the greatest ethylene binding.

5.6. References

(1) Martin, J. D.; Dattelbaum,A. M.; Sullivan, R. M.; Thornton, T. A.; Wang, J.; Peachey, M. T. *Chem. Mater.* **1998**, *10*, 2699.

(2) Martin, J. D.; Greenwood, K. B. *Angew. Chem., Int. Ed. Eng.* **1997**, *36*, 2072.

(3) Gilliland, E. R.; Seebold, J. E.; Fitzhugh, J. R.; Morgan, P. S. *J. Am. Chem. Soc.* **1939**, *61*, 1960.

(4) Sullivan, R. M.; Martin, J. D. *J. Am. Chem. Soc.* **1999**, *121*, 10092.

(5) Sullivan, R. M.; Martin, J. D. in *Luminescent Materials*, McKittrick, J.; Di Bartolo, B.; Mishra, K., eds., *Proc. Mat. Res. Soc.*, **1999**, 560, 39.

(6) Kim, Y. H.; Ryu, J. H.; Kang, Y. S.; Kim, H. S. *Chem Comm.* **2000**, 195.

(7) Rege, S. U.; Padiu, J.; Yang, R. T. *AIChE J*. **1998**, *44*, 799.

(8) Kauffman, G. B.; Fang, L. Y. *Inorg. Syn*. **1983**, *22*, 101.

(9) Thesis of Andrew M. Dattelbaum, NCSU, 2000, Chapter 3.

(10) Gabe, E. J.; Le Page, Y.; Charland, J.-P.; Lee, F. L.; White, P. S. *J. Appl. Crystallogr*. **1989**, *22*, 384.

(11) Altomare, A.; Burla, M. C.; Camulli, G.; Cascarano, G.; Giacovazzo, C.; Guagliardi, A.; Polidori, G. *J. Appl. Cryst.* **1994**, *27*, 435.

(12) Wendlandt, W. W.; Hecht, H. G. *Reflectance Spectroscopy*; Interscience: New York, 1966; Chapter 3.

(13) Blasse, G.; Grabmaier, B. C.; *Luminescent Materials*; Spriner-Verlag: Berlin, 1994; p A4.

(14) Hammersley, A. P., *FIT2D: An Introduction and Overview*, ESRF Internal Report, ESRF97HA02T, European Synchrotron Radiation Facility: Grenoble Cedex, France, **1997**.

(15) Hammersley, A. P., *FIT2D V9.129 Reference Manual V3.1*, ESRF Internal Report, ESRF98HA01T, European Synchrotron Radiation Facility: Grenoble Cedex, France, **1998**.

(16) Norby, P. "In-situ Time Resolved Synchrotron Powder Diffraction Studies of Syntheses and Chemical Reactions" *Materials Science Forum* **1996**, Vol.s 228-231, pp. 147-152.

(17) Norby, P. *J. Appl. Crystallogr.* **1997**, 30, 21.

(18) Amemiga, Y. *Synchrotron Radiation News* **1990**, 3, 21.

(19) Cox, E. G.; Cruickshank, W. J.; Smith, J. A. *Proc. R. Soc. London, Ser. A* **1958**, *247*, 1.

(20) Bacon, G. E.; Curry, N. A.; Wilson, S. A. *Proc. R.. Soc. London, Ser. A* **1964**, *279*, 98.

(21) Wright, G. T. *Proc. Phys. Soc., London* **1955**, *B68*, 701.

(22) Cox, E. G.; Cruickshank, W. J.; Smith, J. A. *Proc. R. Soc. London, Ser. A* **1958**, *247*, 1.

(23) Bacon, G. E.; Curry, N. A.; Wilson, S. A. *Proc. R.. Soc. London, Ser. A* **1964**, *279*, 98.

(24) Dattelbaum, A. M. Ph.D. dissertation, Chapter 3.

(25) Dattelbaum, A. M.; Martin, J. D. *Inorg. Chem.* **1999**, *37*, 6200.

(26) Bruce, D. W.; O`Hare, D., eds, *Inorganic Materials*, John Wiley & Sons, Chichester, England, 1992.

(27) Gilliland, E. R.; Seebold, J. E.; Fitzhugh, J. R.; Morgan, P. S. *J. Am. Chem. Soc.* **1939**, *61*, 1960.

(28) Schaller, G. E.; Bleecker,, A. B. *Science* **1995**, *270*, 1809.

(29) Rodriguez, F. I.; Esch, J. J.; Hall, A. E.; Binder, B. M.; Schaller, G. E.; Bleecker, A. B. *Science*, **1999**, *283*, 996.

(30) Straub, B. F.; Eisenträger, F.; Hofmann, P. *Chem. Comm.* **1999**, 2507.

(31) Munakata, M.; Kitagawa, S.; Kosome, S.; Asahara, A. *Inorg. Chem.* **1986**, *25*, 2622.

(32) Susenaga, Y.; Liang, P. W.; Takayoshi, K.-S.; Munadata, m.; Maekawa, M. *Polyhedron* **1997**, *16*, 67.

(33) Masuda, H.; Yamamoto, N.; Taga, T.; Machida, K.; Ditagawa, S.; Munakata, M. *J. Organometallic Chem.* **1987**, *322*, 121.

(34) Thompson, J. S.; Harlow, R. L.; Whitney, J. F. *J. Am. Chem. Soc.* **1983**, *105*, 3522.

(35) Thompson, J. S.; Whitney, J. F. *Inorg. Chem.* **1984**, *23*, 2813.

(36) Martin group, unpublished results.

(37) Martin, J. D.; Leafblad, B. R.; Sullivan, R. M.; Boyle, P. D. *Inorg. Chem.* **1998**, *37*, 1341.

(38) Work in progress.

(39) Strauss, S. H. *J. Chem. Soc. Dalton,* **2000**, *1*, 1.

(40) Ziegler, T.; Rauk, A. *Inorg. Chem.* **1979**, *18*, 1558.

(41) X-ray Research GmbH **1999**. Image Plate Detector System (345 mm diameter). X-ray Research GmbH, Segeberger Chassee 34. 22850 Norderstedt, Germany.

Chapter 6:

Conclusion

The work described in this dissertation has extended the types of metal-halide analogs of metal-oxides that have been synthesized utilizing a halide for chalcogenide substitution methodology. Metal-halide analogs of phosphates, phosphonates, and clay-type materials have been designed from copper(I) chloride tetrahedra and zirconium(IV) chloride octahedra by incorporating a building block approach for new materials design. Following such a methodology, the structural relationship between the isoelectronic and isostructural tetrahedral building blocks $(CuCl_4)^{3-}$ and $[PO_4]^{3-}$ was established by the synthesis of the octahedral and tetrahedral chains in $[CuZrCl_6]^-$, which are analogous to the thiophosphate chains in the $[NiPS_4]^-$. Furthermore, the $[(bz)CuCl_3]^{2-}$ building blocks found in $((bz)CuCl_3)_2Zr$ were described as the metal-halide equivalent to the phosphonate building blocks, $[RPO_4]^{2-}$. And, the Cu_3ZrCl_9 adamantine-type building blocks found in the condensed three-dimensional material Cu_2ZrCl_6 are similar to adamantine-type building blocks commonly observed for metal sulfide materials.

A common feature of Cu^+ that is continuously encountered in this work, is the propensity of copper(I) chloride tetrahedra to distort as a result of second-order mixing. Such second-order mixing was found to be a major influence on the structure, as well as the electronic and magnetic properties, of the copper(I)-zirconium(IV) materials described here. In general, this second order mixing resulted in a distortion of the copper(I) coordination environment from a tetrahedral geometry towards a trigonal pyramidal coordination of halides, as seen in $[NMe_2H_2]CuZrCl_6$. The second-order mixing of the high-lying filled and low-lying unfilled orbitals on Cu^+ was found to be dependent on the thermal energy of the system in all of the materials described here. And, in the case of $[NMe_2H_2]CuZrCl_6$, hydrogen bond formation from the chloride

anions to dimethylammonium cations appears to facilitate significant the second-order mixing resulting in distortions to the metal chloride building blocks.

It was also shown that the addition of Lewis acids into the CuCl framework can control the band gap of CuCl. By stoichiometrically doping the empty Zr^{4+} 4d-orbitals into the CuCl band gap, the nature of the lowest energy transition was changed from a copper centered transition to a copper-to-zirconium transition, which can lead to an absorption in the visible region of the electromagnetic spectrum as demonstrated in Cu_2ZrCl_6. And, as a result of the second-order mixing at the copper(I) sites in Cu_2ZrCl_6, the band gap was observed to decrease leading to thermochromic phase transition, which accompanied the structural distortion at copper. Based on these results, addition of other empty, low-lying d-orbtials, such as those of V^{5+}, into the CuCl band gap is anticipated to allow further control over the absorption and electronic properties of CuCl. It may also be possible to extend these ideas of stoichiometric doping described here, which is, of course, commonly done in the field of materials science, to include other semiconductors into new materials design.

One of the most intriguing results of this work is the field dependent Van Vleck paramagnetism observed for Cu_2ZrCl_6. At room temperature, the paramagnetism was observed to maximize at a small applied field before becoming increasingly diamagnetic. To my knowledge, such behavior has yet to appear in the literature. Nevertheless, the paramagnetic behavior can be understood by an indirect Van Vleck paramagnetism, which occurs through the chloride bridges. Although a cohesive explanation of the magnetic behavior has not yet been determined, the maximum magnetization appears to be coupled to the band gap of the semiconducting materials studied here, i.e. as the band

gap increases greater applied fields are needed to maximize this term.. The field dependence on the Van Vleck paramagnetism may be a common phenomenon for wide band gap semiconductors; however, more data is necessary to substantiate this generalization.

Materials construction from Lewis acids and cuprous chloride building blocks are also shown to dramatically affect the binding capability of copper(I). For example, the reactivity of Cu^{+} in the presence of the Lewis acidic Zr^{4+} was demonstrated by the solvothermal reaction of Cu_2ZrCl_6 in benzene, which breaks up the three-dimensional framework into a one-dimensional $[((bz)CuCl_3)_2Zr]_\infty$ chain. Chains of $((bz)CuCl_3)_2Zr$ are linked along the crystallographic **c** direction *via* an edge-to-face π-stacking of the coordinated benzene molecules. The crystal packing forces are shown to influence dramatic second-order Jahn-Teller distortions making each of the two $((bz)CuCl_3)^{2-}$ units distinct. The distortions of the distinct $((bz)CuCl_3)^{2-}$ units emphasize the unique donor and acceptor properties of the Cu(I) ion. Binding of benzene molecules was also observed at different stoichiometries of copper to zirconium. The addition of $ZrCl_4$ to the solvothermal reaction of Cu_2ZrCl_6 in benzene yields the molecular species $(bz)_2Cu_2Zr_2Cl_{10}$•bz, which loses to yield a luminescent material, with one mole of benzene per copper site. Upon complete loss of benzene from the inorganic material, the luminescence is lost and a new phase forms. These desolvated materials exhibit reversible binding of ethylene reminiscent of the behavior typically observed for silicate-based clays. The sorption/resorption behavior was studied by X-ray diffraction, as well as volumetric and spectroscopic measurements. Based on this data, a topotactic condensation mechanism for the desolvation of benzene was proposed.

Sorption/resorption of ethylene occurred *via* a similar destructive/constructive pathway. Having demonstrated the reversible binding of organic molecules to the copper-zirconium chlorides, the catalytic activity of these materials can now be investigated. Thus, these results may eventually lead to new catalytic materials, which could combine the size and shape selectivity of a framework material with the lability of the cuprous chloride building blocks.

RESUME

Andrew Dattelbaum

Department of Chemistry
North Carolina State University
Raleigh, NC 27695-8204
phone: (919) 515-8924
fax: (919) 515-8909

108 Rubin Ct
Apt A4
Cary, NC 27511
(919) 481-1208
e-mail: amdattel@pams.ncsu.edu

EDUCATION

Ph.D.; Inorganic Chemistry
Minor: Solid State Sciences
North Carolina State University, Raleigh, NC
Thesis Advisor: James D. Martin

Bachelor of Science, Magna Cum Laude with Distinction in Chemistry (ACS Certified)May 1995
James Madison University, Harrisonburg, VA

RESEARCH EXPERIENCE

Doctoral Candidate, NCSU, James D. Martin 1996 to present

- Designed and synthesized transition metal-halide analogs of metal oxides
- Determined single crystal X-ray structure of the synthesized materials
- Performed i*n situ* reactivity studies on powder samples in inert or vacuum environments using the Synchrotron Light Source at Brookhaven National Laboratory
- Performed *in situ* diffuse reflectance studies monitoring ethylene sorption by metal-halide complexes
- Performed Variable Temperature ^{31}P NMR experiments on Metal-Halide-Phosphine complexes
- Performed extended Hückel calculations on metallo-organic materials

Research Assistant, JMU, John Mosbo and Donna Amenta 1992 to 1995

- Prepared 4'-chloromethyl-benzo-15-crown-5 through a multi-step organic synthesis
- Prepared $(\eta^5\text{-}C_5H_5)M(CO)_xCH_2R$ (M = Mo, Fe;R = $CH_2C_6H_3$-benzo-15-crown-5, $CH_2(C_6H_3)(OCH_3)_2$) and it's acyl complex *via* a migratory insertion reaction upon introduction of a phosphine ligand
- Performed kinetic studies monitoring the formation of the acyl complex both in the presence and absence of sodium cations using ^1H NMR

TECHNICAL EXPERTISE

X-ray diffraction (single crystal and powder), Schlenk/Vacuum line syntheses, NMR, Solid-State UV-Vis, IR, DSC

PROFESSIONAL EXPERIENCE

Coordinator for *Chemistry: A Quantitative Science* solutions manual	1999
Mentor for ACS-Project SEED at NCSU	1999
Mentor for NSF-Research Experience for Undergraduates (REU) program at NCSU	1998
Mentor for a High School Army Research Scholar at NCSU	1997
Teaching Assistant in General Chemistry, NCSU and JMU	1993 to 1997
Tutor for General and Organic Chemistry students	1993 to present

AWARDS AND HONORS

PLU Travel Award	2000
Preparing the Professoriate Fellowship	1998
American Institute of Chemists Award	1998
Science Applications International Corp. (SAIC) Thesis Award	1995
ACS/Merck Award (Given to outstanding Senior chemistry major)	1995
R. D. Cool Award (Given to outstanding Junior chemistry major)	1994
Presidential Premedical Scholar	1991 to 1995
Research Experience for Undergraduates (REU) at JMU	1993 and 1994
Elected President Phi Lambda Upsilon	2000
Elected Senior Advisor Phi Lambda Upsilon	1999
Elected Vice President Phi Lambda Upsilon	1998 to 1999
Elected Graduate Student Association Co-Representative	1997 to 1998
Elected President Alpha Chi Sigma, A Professional Chemistry Fraternity	1994 to 1995

PRESENTATIONS

(Lecture) "Design and Reactivity of Copper(I)-Zirconium(IV) Transition Metal Halide Materials," 219th National ACS Meeting, San Francisco, CA, March 26-30, 2000.

(Lecture) "Transition Metal Halide Analogs of Phosphonate Materials," Southeastern Regional ACS Meeting, Research Triangle Park, NC, Nov. 6-7, 1998.

(Poster) "Metal Halide Analogs of Phosphates and Phosphonates," Solid State Gordon Conference, Colby-Sawyer College, New London, NH, July 26-Aug. 3, 1998.

(Lecture) "Rational Design of Octahedral and Tetrahedral Metal Halide Framework Solids," 111th ACS North Carolina Sectional Meeting, Duke University, Durham, NC, April 5, 1997.

(Lecture) "The Synthesis and Studies of (η^5-C_5H_5)M(CO)$_x$$CH_2$R (M= Mo, Fe; R = $CH_2C_6H_3$-benzo-15-crown-5 or $CH_2(C_6H_3)(OCH_3)_2$)," National Conference on Undergraduate Research, Union College, Schenectady, NY, April 20-22, 1995.

(Lecture) "The Synthesis and Studies of (η^5-C_5H_5)$Fe(CO)_2CH_2$R (R = $CH_2C_6H_3$-benzo-15-crown-5 or $CH_2(C_6H_3)(OCH_3)_2$)," Virginia ACS Sectional Meeting, The College of William and Mary, Williamsburg, VA, April 20-22, 1994.

PUBLICATIONS

1. Templated Synthesis of Cuprous Chloride Networks: The Synthesis and Characterization of [Hpy]Cu_3Cl_6 and {[$H_3NMe]_6Cl$}[$H_3NMe]_2Cu_9Cl_{16}$. J. D. Martin, J. Yang, and A. M. Dattelbaum, *Chem. Mater.* Submitted.

2. Benzene-Copper(I) Coordination in a Bimetallic Chain Complex. A. M. Dattelbaum and J. D. Martin, *Inorg. Chem.* **1999**, *38*, 6200.

3. ($N(CH_3)_2H_2$)$CuZrCl_6$: Hydrogen Bond Induced Distortions in a Copper Zirconium Chloride Analog of a Thiophosphate. A. M. Dattelbaum and J. D. Martin, *Inorg. Chem.* **1999**, *38*, 2369.

4. Metal Halide Analogs of Oxides: A Building Block Approach to the Rational Synthesis of Solid State Materials. J. D. Martin, A. M. Dattelbaum, T. A. Thornton, R. M. Sullivan, J. Wang, M. T. Peachey, *Chem. Mater.* **1998**, *10*, 2699.